UNIVERSITY OF ROCHESTER
LABORATORY FOR LASER ENERGETICS

Volume 74
January–March 1998
DOE/SF/19460-241

LLE Review

Quarterly Report

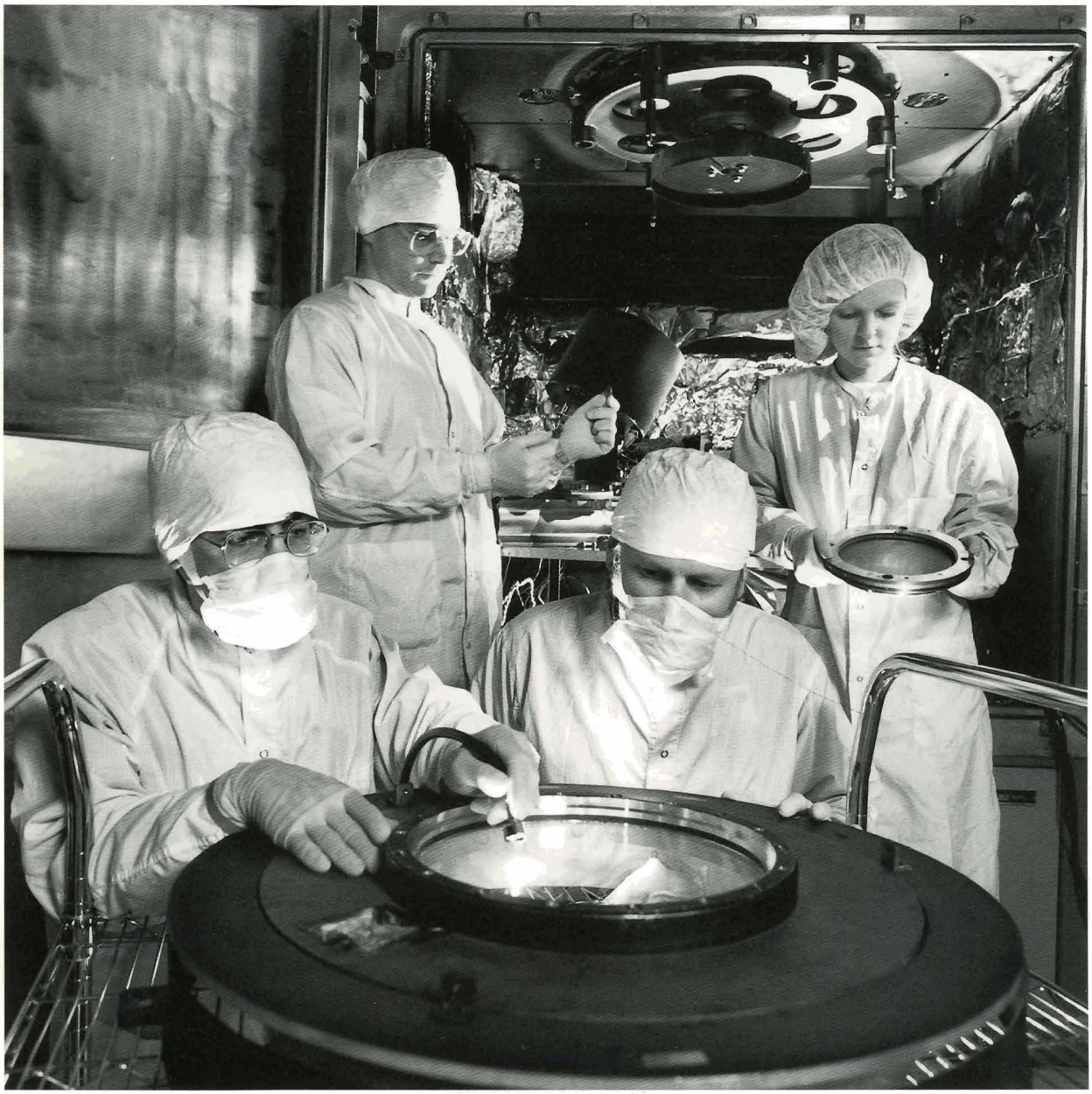

About the Cover:

The Optical Manufacturing Group's 54-in. vacuum chamber (seen in the background) has been converted from a deposition system to one with an ion-etch capability to produce distributed phase plates. Nelson LeBarron, technical associate (standing left), inspects a thin neutralizer filament while Joy Warner, laboratory engineer, checks the grids for the 16-cm ion source. In the foreground, Salvatore LaDelia (left), electronics technician, and Douglas Smith, research engineer, inspect a distributed phase plate substrate prior to etching. The chamber produced 60 continuous phase plates with high laser-damage thresholds etched directly into silica for the OMEGA laser. The substrate rotation hardware and the cryo baffle that keep the photoresist from overheating are seen in the upper background.

The work described in this volume includes current research at the Laboratory for Laser Energetics, which is supported by New York State Energy Research and Development Authority, the University of Rochester, the U.S. Department of Energy Office of Inertial Confinement Fusion under Cooperative Agreement No. DE-FC03-92SF19460, and other agencies.

For questions or comments, contact Stephen D. Jacobs, *Editor*, Laboratory for Laser Energetics, 250 East River Road, Rochester, NY 14623-1299, (716) 275-4837.

Worldwide-Web Home Page: http://www.lle.rochester.edu/

Printed in the United States of America
Available from
National Technical Information Services
U.S. Department of Commerce
5285 Port Royal Road
Springfield, VA 22161

Price codes: Printed Copy A05
Microfiche A01

UNIVERSITY OF ROCHESTER
LABORATORY FOR LASER ENERGETICS

Volume 74
January–March 1998
DOE/SF/19460-241

LLE Review

Quarterly Report

Contents

In Brief iii

The Development of Ion-Etched Phase Plates 71

A High-Resolution X-Ray Microscope for Laser-Driven Planar-Foil Experiments 92

Measurements of Core and Pusher Conditions in Surrogate Capsule Implosions on the OMEGA Laser System 100

Accurate Formulas for the Landau Damping Rates of Electrostatic Waves 113

Efficient, End-Pumped, 1053-nm Nd:YLF Laser 120

Self- and Cross-Phase-Modulation Coefficients in KDP Crystals Measured by a *Z*-Scan Technique 125

Micromechanics of Material-Removal Mechanisms from Brittle Surfaces: Subsurface Damage and Surface Microroughness 131

Cholesteric Liquid Crystal Flakes—A New Form of Domain ... 139

Publications and Conference Presentations

In Brief

This volume of the LLE Review covers the period January–March 1998. The first of eight articles documents the in-house development, scale-up, and manufacture of 60 continuous distributed phase plates with high laser-damage resistance. D. J. Smith *et al*. describe how inert ion beams were used to etch a continuously varying pattern into the surface of fused silica to form these devices.

Other highlights of research presented in this issue are

- A soft x-ray microscope ($E < 3$ keV) with high spatial resolution (~3 μm) has been characterized and used for initial experiments on the OMEGA laser system. F. J. Marshall *et al*. give details of the testing, calibration, and initial use of this microscope for studying the hydrodynamic stability of directly driven planar foils.

- D. K. Bradley *et al*. report on a series of experiments designed to investigate hydrodynamic instability growth in direct-drive capsule implosions. Measurements of the effects of imprint and unstable growth at the ablation surface have been carried out using the burnthrough technique, and target behavior during the deceleration phase has been investigated using Ti-doped shells surrounding an Ar-doped D_2 fill gas.

- C. J. McKinstrie *et al*. report on the use of systematic perturbation methods to derive formulas for the Landau damping rates of electron-plasma and ion-acoustic waves. Their formulas are more accurate than the standard formulas found in textbooks.

- High efficiency and good beam quality are potential advantages of the end-pumped solid-state lasers over the side-pumped ones. A. Babushkin *et al*. describe their successful use of a transport fiber to end-pump a Nd:YLF laser, overcoming issues related to the astigmatic nature of the high-power, quasi-cw diode laser pumping source.

- Using a single-beam *Z*-scan technique, L. Zheng and D. D. Meyerhofer report values for the self-phase modulation coefficients in a KDP crystal at wavelengths of 1.053 μm, 0.527 μm, and 0.351 μm. The cross-phase modulation coefficients between 1.053 and 0.527 μm, measured by a two-color *Z*-scan, are also given.

- J. Lambropoulos *et al*. propose a model that relates brittle material mechanical properties and grinding abrasive properties to the value of surface roughness that results from the cold working process. Surface roughness as measured by white-light interferometry can be used to establish an upper bound to the level of subsurface damage induced by grinding.

- The optical and physical properties of polymer liquid crystal flakes, alone and embedded in carriers, are explored by E. Korenic *et al*. These materials have applications as color coatings, polarizing paints, and inks.

Stephen D. Jacobs
Editor

The Development of Ion-Etched Phase Plates

Laser-driven implosion experiments on the OMEGA laser depend on optical phase conversion to provide uniform irradiation onto a target. Phase errors that accumulate as a wavefront propagates through the laser produce a nonuniform irradiance when focused into the target far field. The distributed phase plate (DPP) introduces a quasi-random phase front that produces a high-spatial-frequency, uniform pattern with a controlled energy envelope.[1] DPP's are used in conjunction with smoothing by spectral dispersion (SSD) and distributed polarization rotation to provide very smooth intensity distribution on the target when integrated over the full pulse duration of the laser.[2]

The continuous DPP is an improvement over earlier binary designs.[3] The binary phase plates used on the 24-beam OMEGA produced a uniform irradiation with limited control over the intensity envelope and a maximum of 78% efficiency with much of the lost energy coupled into higher diffractive orders. In OMEGA's target chamber geometry this diffracted light would cause catastrophic damage in the opposing beam optics, especially the frequency-conversion cell. The more recent continuous phase design offers better control of the speckle distribution and the envelope function while increasing the total energy impinging on the target to 96%. In addition to a continuous profile, the newer DPP design requires a deeper surface relief of approximately 5 μm. The binary DPP required only a surface relief of 0.3 μm between diffractive cells.

The principle of the continuous DPP's has been demonstrated and tested using a replication process.[3,4] The required pattern is generated as an amplitude modulation in photographic film and used to expose a photoresist-coated substrate. When developed, the relief pattern in the resist is coated with a release layer and then molded in epoxy supported by another silica substrate. After curing, the epoxy is separated from the master, the remnants of the release layer are removed, and the final epoxy negative relief is coated with a water-based sol-gel antireflection coating. Unfortunately, after exposure to many high-energy laser pulses, the epoxy material developed a high absorption peak near 351 nm and after 100 laser shots began to show a high level of damage. The ion-etched DPP was developed as a remedy to the failed, replicated epoxy phase plates. Much of the technology developed for the epoxy phase plates was successfully transferred to the newer etching method. This article emphasizes the technology developed exclusively for the ion-etched phase plate and will not delve into the details of phase-plate design, methods for making a master, testing methods, or target performance results with DPP.

Key Technical Issues for Ion Etching

The problems posed in etching DPP's are unique. While ion-etching methods are commonly used in the semiconductor industry, they are typically used for binary patterns with etch depths rarely exceeding 1 μm. Diffractive optics, which do have continuous profiles, are made typically on substrates much smaller than the required 30-cm aperture of the OMEGA laser, and once again usually have smaller etch depths. Experience with large optics, familiarity with broad-beam ion sources, and a short development period led to an intensive internal development program.

The ion-etch scheme used by LLE is shown schematically in Fig. 74.1. A positive image of the photoresist master will result after etching, unlike the negative image produced with replication. This does not affect the performance of the DPP; positive and negative profiles have the same far-field performance. The positive image does have an effect on the type and number of near-field defects (discussed in detail later).

An inert ion process was used for etching the DPP's. Inert ion etching (or ion milling) depends on molecular impacts (sputtering) for materials and is a purely physical process. Reactive processes were developed for high material-removal rates in a high-production environment, production of steep edges for semiconductor interconnects, and material selectivity to preserve masks. The intensity exposure mask for continuous DPP design in Fig. 74.2 has low gradient (no steep edges), and material selectivity is not as important as faithful reproduction of the photoresist surface. This last requirement demands that the etch depth be linear with time for both materials, which

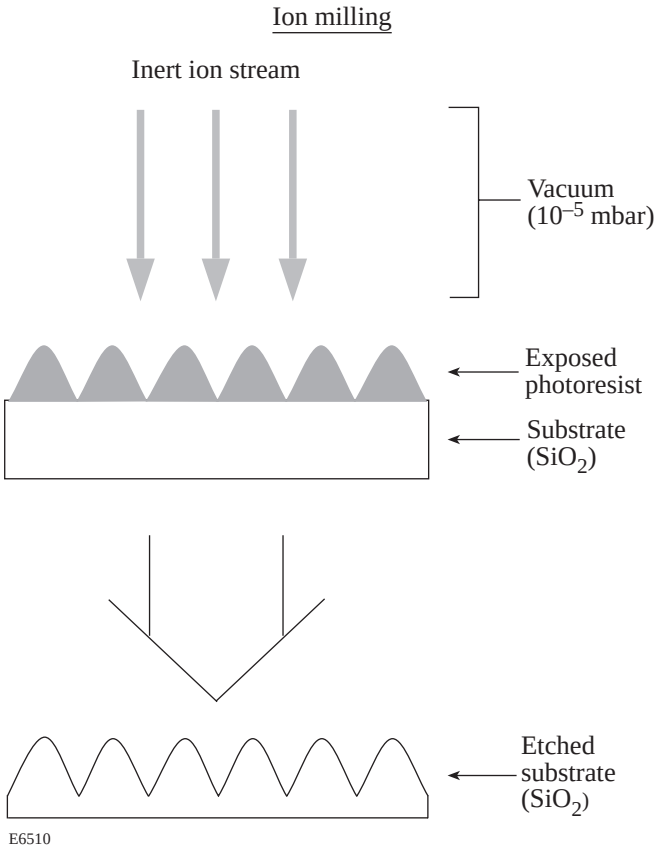

Figure 74.1
A surface-relief phase plate can be directly etched from a photoresist pattern into a silica substrate. The photoresist is completely removed after etching is complete. The etching molecule in this work is an inert gas, argon, so removing the photoresist and silica is purely a physical process.

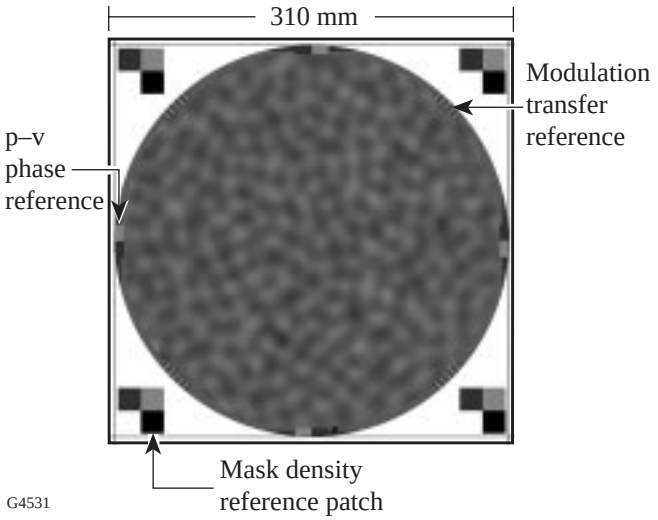

Figure 74.2
The continuous DPP for the third-order super-Gaussian profile used on OMEGA was designed using simulated annealing. The amplitude variation of the mask is transferred into phase variation by exposing the photoresist to the mask. The central portion of the mask was modified after design to provide a high point in the resist for in-process optical monitoring.

is more likely in a purely physical process. Complete erosion of the mask is necessary since any remnant photoresist could be the potential site for laser damage in the 351-nm radiation. Since LLE has had little previous experience with reactive processes, inert ion etching was the method of choice.

A number of key technical issues had to be resolved before DPP's could be produced:

1. Uniformity

The uniformity of etch across the 280-nm beam aperture had to vary less than 6% after 5 μm of material was removed. This was accomplished by first using two 8-cm ion sources with the substrate in single rotation and, later in the project, a single 16-cm ion source, also with single rotation. After establishing the correct operating parameters for the guns, all were profiled at different beam voltages and total ion currents using a biased ion probe. The profiles were used to calibrate a model of etch uniformity that was developed to determine the best source location and pointing for high uniformity and reasonable etch rate. It is well known that the sputtering yield varies considerably with the ion incidence angle in inert ion etching.[5] The relationship between etch rate and incidence angle had to be determined for the two etch materials: silica and photoresist.

2. Surface Texturing

Surfaces are often textured after a high level of ion bombardment.[6,7] Silica surfaces have been observed to become rougher or smoother depending on the type of ion, ion energy, incidence angle, and ion density.[8,9] Texturing occurs predominantly in crystalline materials and is most often caused by the varying sputter rate of different crystal planes. Resputtering and defects in the surface preparation of a substrate have also caused texturing.[10] During development of etched DPP's, severe roughing of the surface was often observed but it was primarily caused by the overlying photoresist. Although surface texturing by ions was often suspected, the true cause appears to be excessive heating of the resist in almost all cases.

3. Linearity

An accurate representation of the photoresist master in silica can only be realized if the process remains linear throughout the etch. Proper processing of the resist and careful control of the substrate thermal cycle produced adequate linearity.

4. Near-Field Defects

Near-field defects are caused by small and steep surface variations in the photoresist layer, which cause diffraction and high intensities downstream of the DPP. These defects have a strong potential to damage the final focus lens and blastshields on the target chamber. Near-field defects were first observed in the fabrication of the first set of continuous epoxy DPP's for OMEGA. Methods for detecting and removing the defects were established for the epoxy DPP's and then modified for the ion-etched devices.

5. Production Tooling

Resputtering of tooling materials will cause higher absorption and scatter on the ion-etched surface. In addition the tooling must allow a clear view of the rear surface to radiate heat to the cooled cryopanels. The tooling design offered a unique solution to these requirements.

6. Laser-Damage Threshold

When measured at 351 nm, some ion-etched samples have shown a decrease in damage threshold. This could be caused by resputtering of ion sources, tooling, or chamber materials onto the optics. The damage threshold of the DPP's had to meet a 2.6 J/cm^2 @ 1-ns peak fluence requirement for the 351-nm OMEGA beam. The damage threshold of the DPP surfaces increased after etching, probably due to careful control of redeposition of tooling and removal of subsurface damage in the silica.

Each of the technical issues listed above is discussed in detail below.

Uniformity of Ion Etching with a Kaufman Source

The Kaufman[11] ion source, originally developed as a propulsion source for NASA, has since seen wide use in materials processing.[12] The source, shown schematically in Fig. 74.3, consists of a discharge chamber with a multipole magnetic field and a hot filament, two dished molybdenum extraction grids, and a neutralizer filament. Two 8-cm ion sources were used for prototype demonstration, and a 16-cm ion source was used for the production phase of this work.

Ion-source parameters are set depending upon the application, type of working gas, and performance of the source in a given pumping system. Argon was used as a working gas because the sputter yields for SiO_2 and photoresist are similar for this gas. The maximum gas flow rate, maximum beam current, and accelerator voltage range for the sources were determined using standard methods.[13] The beam voltage (ion energy) was kept below 500 V to avoid ion implantation, surface damage to the photoresist, and overheating.

The etch profiles of each source were tested using a unique profiling method: A large sheet of inexpensive float glass was coated with an optical multilayer that had a highly visible, 13-layer oxide coating (see Fig. 74.4). The coated plate was placed normal to the ion beam at a distance of 60 cm. The source was run long enough to etch to the last layers of the coating; the coating was then removed and inspected. The erosion pattern could then be discerned as contours in the multilayer surface (see Fig. 74.5). This method gave a very quick appraisal of the gun operation and indicated whether the profile would be suitable for highly uniform etching. For

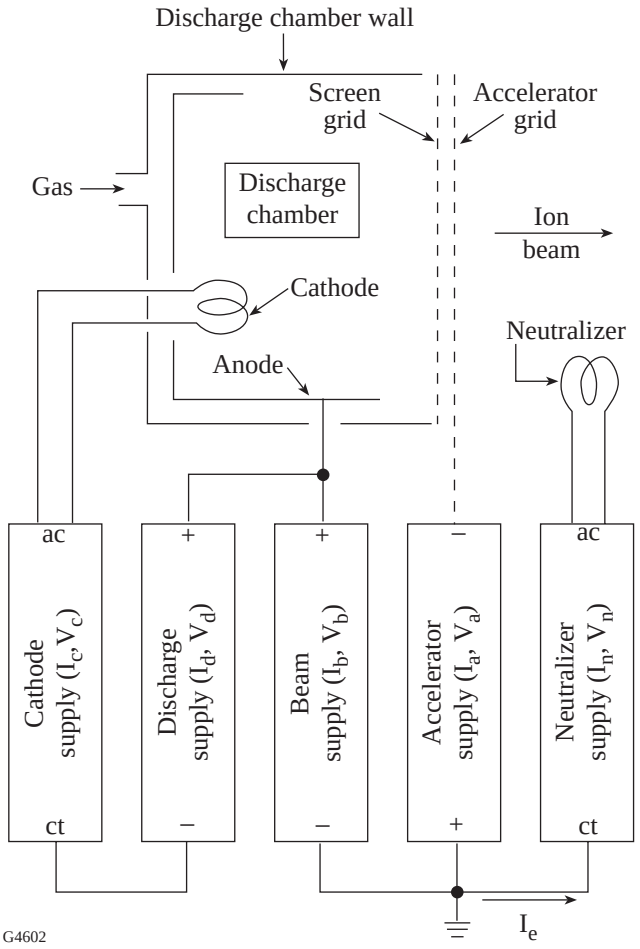

Figure 74.3
A typical broad-beam Kaufman ion source with power supplies is represented schematically. This type of source provides excellent control of ion energy and density. The source's condition during etching can be monitored by logging the voltage and current of each supply.

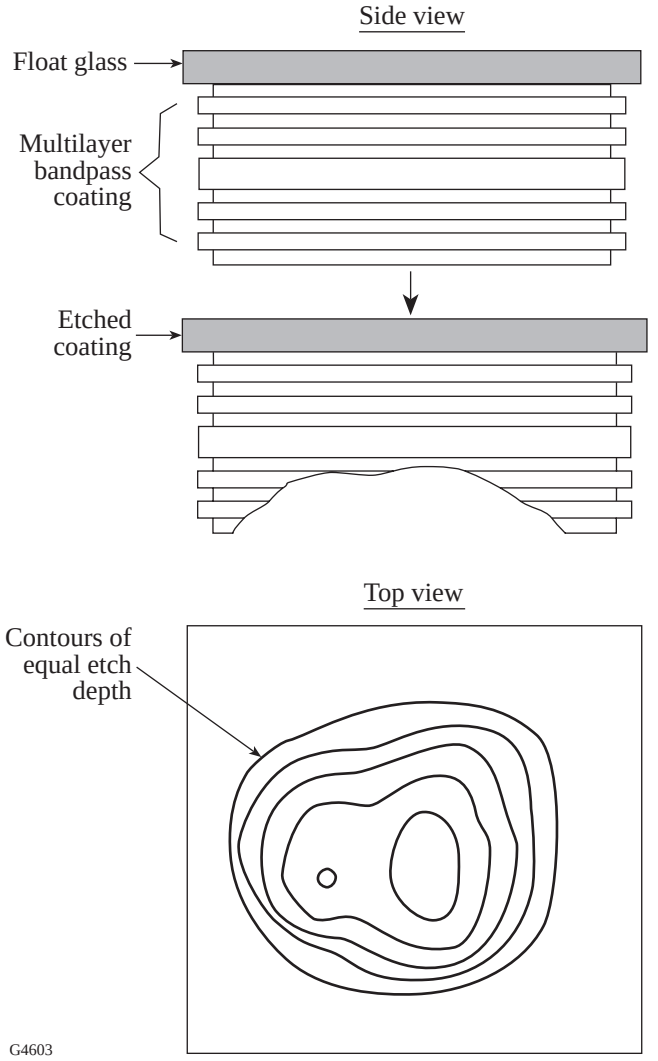

Figure 74.4
Ion-beam profiles can be monitored with a small probe or by etching into a visible interference filter deposited on inexpensive float glass as shown. The beam contours are formed by the eroded layer of the coating. After etching, the layers in an appropriately designed multilayer provide visible isothickness contours, indicating the beam profile of the ion source.

example, the etched profile of the 8-cm source operating at a beam current of 100 mA is shown in Fig. 74.5(a). Even though the source was within the normal electrical limits (low ion impingement of the grids), the profile has significant structure. The same source produced a low-structure symmetrical profile when operated at 50 mA [Fig. 74.5(b)] and was subsequently used with beam currents (I_b) no larger than 75 mA. The condition of the source anode also had a significant effect on the beam profile. The anode can be run in excess of 60 h before a discharge becomes difficult to maintain, as seen in Fig. 74.5(c); however, the beam profile again shows structure with the older anode. If the anode is abrasively cleaned, the structure in the beam profile disappears. The 16-cm source was later characterized in the same manner. Figure 74.5(d) shows the symmetrical beam profile of the source when operated with I_b = 300 mA and a beam voltage of 150 V.

The gun profiles were quantitatively measured with an open stainless steel probe after the initial gun characterization to determine the operational limits of the sources. For these measurements the ion probe was negatively biased with 18 V to repel the low-energy electrons in the beam. Both the 8-cm and the 16-cm sources were characterized at heights from the source grids ranging from 20 cm to 85 cm. The 8-cm source profiles were observed under varying conditions to determine which parameters affected the beam profile. Certain parameters, such as low neutralization current and high chamber pressure, had little effect on the profile. The most significant effect was a buildup of an insulating film on the anode, as noted above with the multilayer etch profiles. Significant differences seen in profiles between the two 8-cm sources were attributed to differences in the magnetic field surrounding the discharge chamber.

The 16-cm source beam profile is exceptionally immune to changes in the operating parameters. Profiles taken under a range of operating conditions and normalized at the on-axis center (r = 0) are compared in Fig. 74.6 for a fixed height above the source. In practice, the similarity in profiles allows use of the source over a wide range of ion energies and densities without making large changes in the geometry established to produce uniform etching. A single model, independent of source parameters, was used in the uniformity code discussed below.

Etching Model

Processes that use energetic ions for large substrates require that the time-averaged erosion effects from the ion flux be uniform across the surface. A numerical model has been developed to determine this flux and its effects on surface etching of a silica/photoresist combination. The geometries of the source and substrate are very similar to typical deposition geometries with single or planetary substrate rotation. The model was used to tune an inert ion-etching process that used single or multiple Kaufman sources[14] to less than ±3% uniformity over a 30-cm aperture after etching 5 μm of material. The same model can be used to predict uniformity for ion-assisted deposition (IAD).

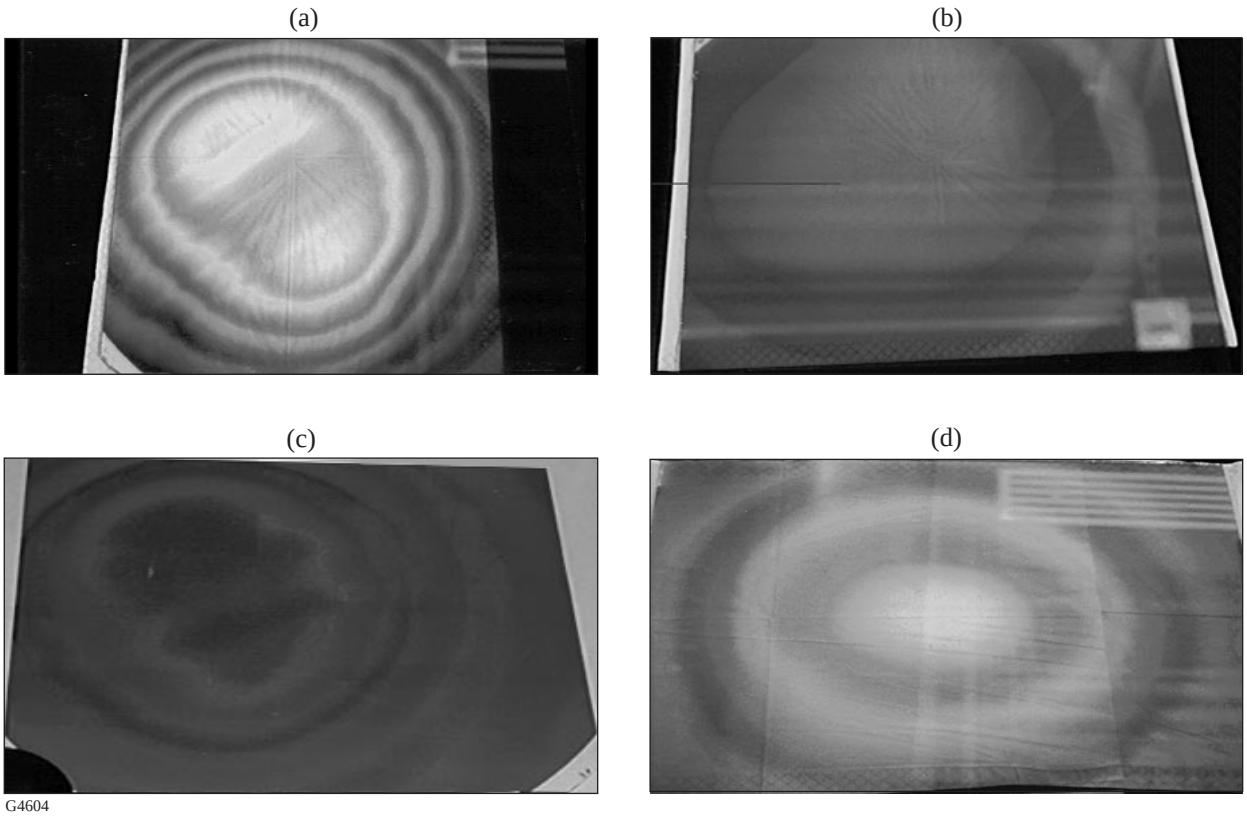

Figure 74.5
The beam profiles formed in the etched multilayers provide rapid feedback to determine correct operating limits and procedure with the ion sources. (a) Profile of a nonuniform etch obtained with the 8-cm source at an excessive beam current (I_b = 100 mA). The structure is a partial image of the spiral filament for the discharge chamber. (b) A profile from the same source as in (a) at lower beam current (I_b = 50 mA). (c) The 8-cm source operated at low current but with a contaminated anode, which had been used previously for 30 h without cleaning. The thin dielectric film that forms on the anode has an obvious effect on the discharge and beam uniformity. (d) The 16-cm source etched uniformly even when used at beam currents as high as 300 mA.

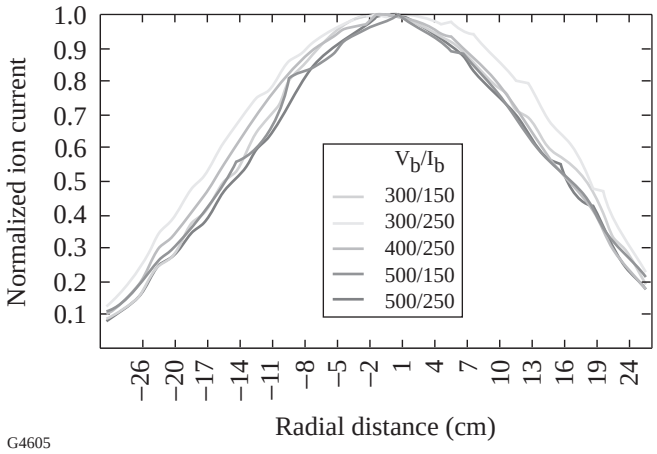

Figure 74.6
The 16-cm source had a stable profile over a wide operating range. The first number in the key is the beam voltage, and the second number is the beam current (in mA). All curves are normalized at $r = 0$.

In Fig. 74.7 an ion source is placed in some arbitrary location and orientation with a substrate rotating in a horizontal plane above the source. The total ion beam flux seen by a point P on a substrate at some radius r from the center can be approximated by

$$E(r) = \sum_{\phi=0}^{\phi_{\max}} I(\phi, r)\, R(\phi, r)\, \Delta\phi, \qquad (1)$$

where $I(\phi, r)$ is the ion flux intensity determined at point ϕ, r and $R(\phi, r)$ is the sputter yield at the same point. R is actually a function of a single variable, the incidence angle of the ion,[15] but both ϕ and r are required to determine this angle. In reality, point P will see a range of incidence angles due to the broad nature of the source. Here, a point source is assumed using the top center of the ion-source grid as the origin of ions, and a single incidence angle is used for the approximation. The example in the diagram shows a simple single rotation of the substrate. For this case, $\phi_{\max} = 2\pi$ represents one full rotation of the substrate and is adequate to model the uniformity. A more complex double rotation (planetary) can also be modeled. In that case the point P traces out an epicycloid instead of a circle.

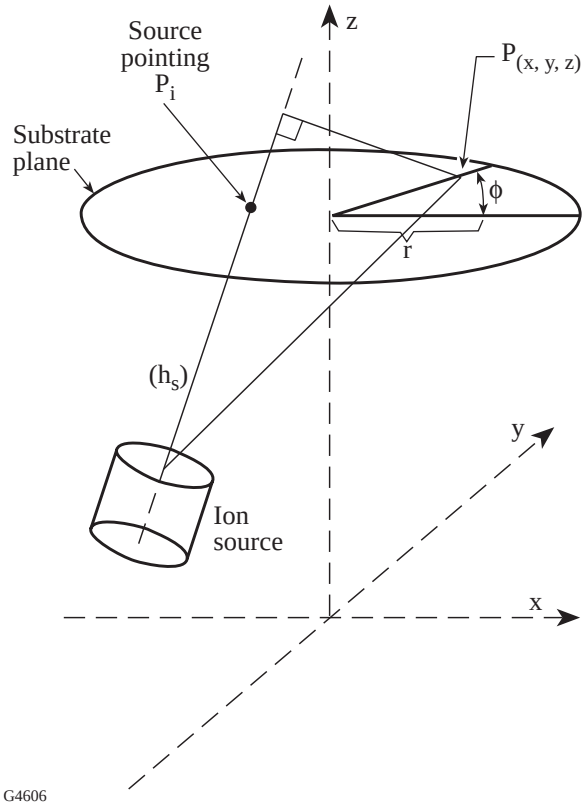

Figure 74.7
Geometry for ion etching with substrate rotation in the horizontal plane. To adjust the uniformity the source pointing was fixed, and then the source was moved on a rail along the x axis.

The model described by Eq. (1) can be broken down into three major parts:

1. summation and location routine: simulates the position of a point on a substrate, finds all position and angular parameters, and integrates the calculated flux through some amount of substrate rotation;

2. expression for $I(\phi, r)$: a model for the expected ion flux that is determined from measured values of the ion source; and

3. expression for $R(\phi, r)$: a relationship between the incident ion angle and energy and the sputtering yield (or etch rate) of the substrate. This also must be determined experimentally.

The model for $I(\phi, r)$ assumes a rotational symmetry of ion density about the axis normal to the ion-source grids.[16] This is a reasonable assumption if the discharge chamber in a hot-cathode source is maintained and cleaned regularly as discussed previously. At a given height h_s above the source, the data can then be fitted to a 1-D super-Gaussian equation

$$I = a + be^{\left(-\left|\frac{r-c}{d}\right|\right)^e}, \qquad (2)$$

where I = ion flux/area for a given r, a = dc offset (usually set to zero), b = amplitude factor at $r = 0$, c = offset for r (set to zero for well-centered beams), d = width factor, and e = shape factor.

The factors b, d, and e all vary with the height above the source. In practice, the beam profile is measured at various heights, and each profile is fitted to Eq. (2). The values found for b, d, and e at various heights are then fitted to curves using a commercial curve-fitting program. The resulting equations and associated coefficients can then be written into a concise code for modeling. Some results of the measured values and the model are given in Figs. 74.8(a) and 74.8(b). The model provides a smoother profile than the actual measured data. This is reasonably accurate since smoothing would also occur in the actual source data if the profile was an average of measurements at some fixed radial distance around the source.

The expression for $R(\phi, r)$, the etch rate as a function of ion incidence angle, was also determined experimentally. Small silica plates with binary photoresist patterns were mounted on miniature rotation drives with the axes set at 20°, 30°, 40°, 50°, 60°, and 0° to the beam axis (see Fig. 74.9). The center of each substrate was placed on a circle, and the entire assembly was rotated in the horizontal plane during the etch; thus, with the ion source on axis, the ion-etch rate for silica and photoresist could be determined simultaneously for six incidence angles by measuring step heights and photoresist thickness. Data were obtained for different operating source parameters and

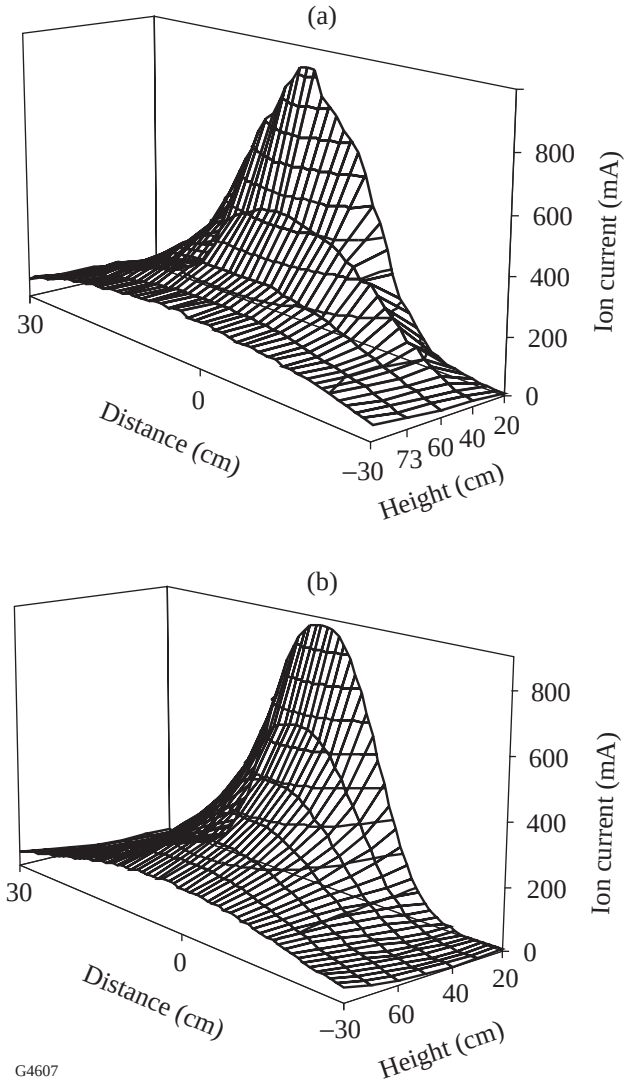

Figure 74.8
(a) Measured profile of the 16-cm ion source operating at 300-V beam voltage and 250-mA beam current at different heights above the grids. (b) Model of measured profile in (a). This model was used in the uniformity program to determine placement of the ion sources.

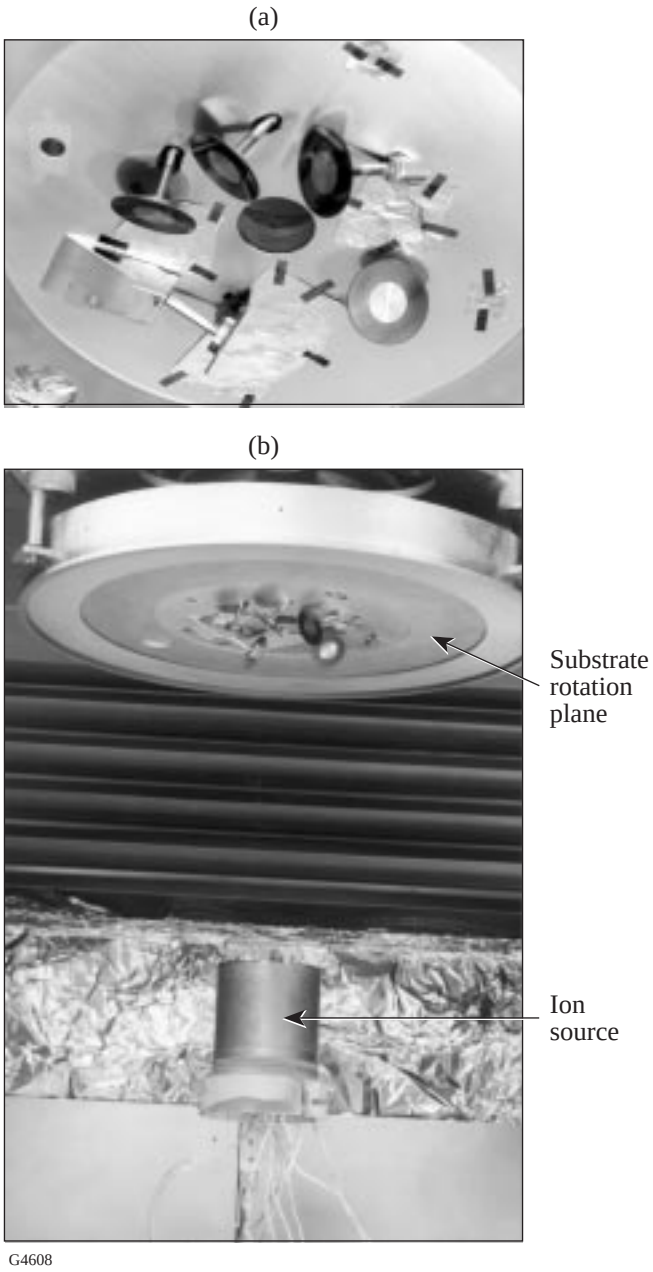

Figure 74.9
(a) The apparatus to measure the etch rate for silica and photoresist simultaneously for several ion incidence angles. Each substrate has a binary pattern of photoresist and is attached to the shaft of a motor. (b) The ion source was placed directly below the apparatus while the entire substrate apparatus above was rotated to obtain a uniform average ion flux density on all test pieces. Substrate heating affected the consistency of results in this experiment.

photoresist preparation processes. The data were often obscured by measurement errors and problems with surface roughening. The original intent was to generate curves for different photoresist annealing conditions (see Fig. 74.10) and to pick the curve that most closely matched the silica curve. In practice, the measurement was flawed by the inability to cool the samples during etching, which increased the apparent etch rate on photoresist. Thus, from these results, the etch rate of photoresist appeared higher than that of silica, but later, on cooled substrates, the etch rate of resist proved to be lower than that of silica.

Since the two materials did etch at different rates but appeared to follow the same curve, the curve for the photoresist annealed at 110°C was selected for the model. The normalized data from this measurement experiment were fitted to a polynomial of the form $y = l + m\theta^2 + n\theta^{2.5} + o\theta^3$. The data and the fitted curve are shown in Fig. 74.11. The accuracy of this data (due to thermal effects) is the largest source of error for the model.

The results for the full uniformity model using the 16-cm source demonstrated that the source should be able to etch a 30-cm aperture uniformly without requiring a supplemental 8-cm source for fine adjustments. Typical results from the full model are shown in Fig. 74.12. The array of curves demonstrates what effect moving the source on a path parallel to the

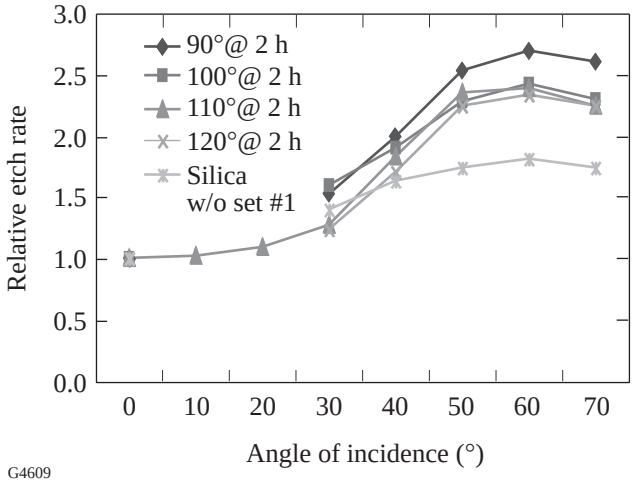

Figure 74.10
The measured etch rate versus ion incidence angle for photoresist anneal after development at different temperatures. Substrate heating affected the consistency of results for photoresist in this experiment. The silica measurements, which are more consistent, are included for comparison. All etch rates have been normalized at 0° for comparison.

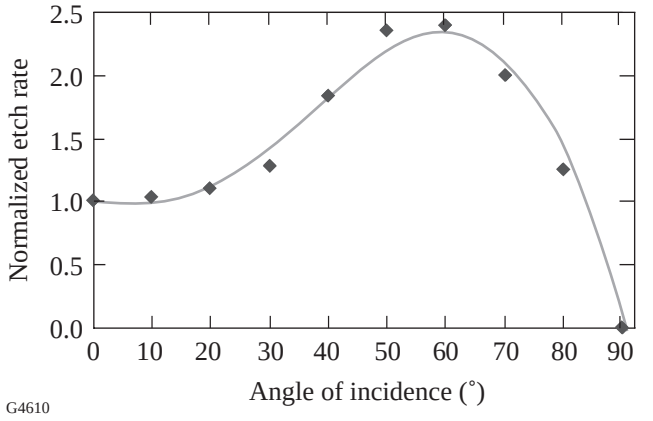

Figure 74.11
The photoresist data for resist baked at 110°C were fitted to the equation $r = \ell + m\theta^2 + n\theta^{2.5} + o\theta^3$ for the uniformity model. Some data were assumed based on other results investigating angular dependence of sputtering.[15] A zero rate was assumed for 90° and values were estimated for 10° and 20°, which satisfies the condition for an increasing positive first derivative.

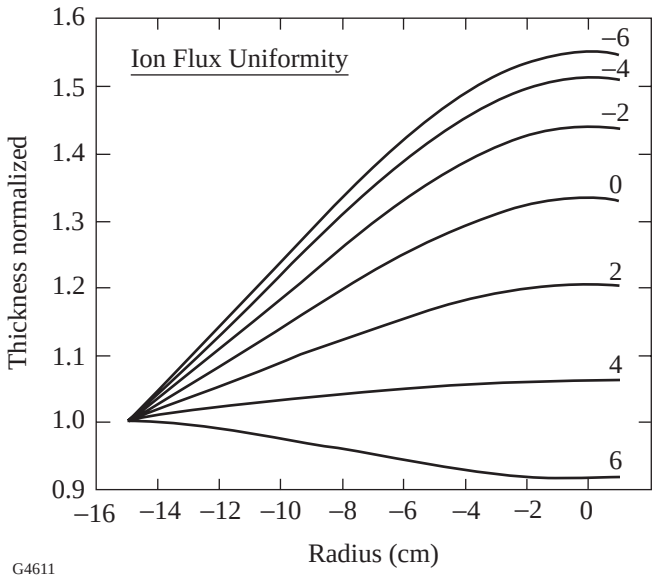

Figure 74.12
The uniformity model is used to evaluate gun positions for one or several ion sources. The graph shows the thickness of material removed, normalized to the first value at –15 cm, as a function of the radius along a DPP-sized substrate. The axis of the source struck the substrate plane at a 30° angle, and the ion-source grid center was placed 34 cm below the substrate. The source was pointed –11.5 cm from the x axis, and the curves represent the change in uniformity as the source is moved along the x axis (*x*-pointing value in centimeters is shown with the curve). This model was reflected in the hardware arrangement with the source on a rail that could easily duplicate the movement along the x axis. The model revealed that a uniform solution could be achieved with the single 16-cm ion source and indicated the sensitivity of positioning. The final position of the source was finally adjusted empirically for best uniformity.

x axis and away from the substrate has on uniformity. The ion-source axis is at 30° with respect to the substrate's normal axis, and the source is pointed away from the center. The model also tracks total integrated current for the starting point, which is used to determine the efficiency of a given geometry. Figure 74.12 shows that a uniformity of better than 7% could be achieved with careful pointing of the source. In practice, etch uniformity of less than 2.5% was measured and, during production of 60 optics, was kept below 6% across the 30-cm clear aperture.

The model was also used early in development to optimize the uniformity of two 8-cm sources etching simultaneously. The model did not always fit the exact results from the chamber; however, it did offer guidance in selecting which direction to move a source while final tuning was completed empirically. The best uniformity results were obtained with the source pointing outside the clear aperture. In this case, most of the ions did not strike the substrate, and the process made inefficient use of the generated ions. A double-source arrangement with a 16-cm and an 8-cm source could have greatly decreased the total etch time but only at the expense of decreased reliability and possible overheating of the photoresist. The 14-h etch time required for the approximately 5-μm etch into fused silica meshed well with the production rate for exposed photoresist-coated plates.

Uniformity Testing

The most reliable test of etch uniformity is to etch directly in silica or photoresist and measure the change in surface profile using interferometry. This method requires a surface that is flat enough to accurately test both before and after the etch. A uniform photoresist coating was applied to a flat-polished substrate, then was partially etched and measured. The substrate could then be stripped of the photoresist and reused without repolishing. The surface measurement prior to etching was stored and subtracted from the post-etch measurement to provide the true etch profile. One sample, if coated with 7 μm of photoresist, could be used several times for uniformity tests during development and as a quality check during production. A sample result of interferometry after etching a photoresist surface is seen in Fig. 74.13. The flat is measured in transmission by placing it in a Fizeau cavity and observing the change in wavefront. The height variation in the resist surface layer is then found from

$$d = \frac{\mathrm{OPD}}{(n-1)} \bullet \frac{\lambda}{2}, \tag{3}$$

where OPD is the optical path difference in waves and n is the refractive index of the photoresist at the test wavelength λ. The factor of 2 compensates for the round-trip path the wavefront travels when transmitting through the optic in the cavity.

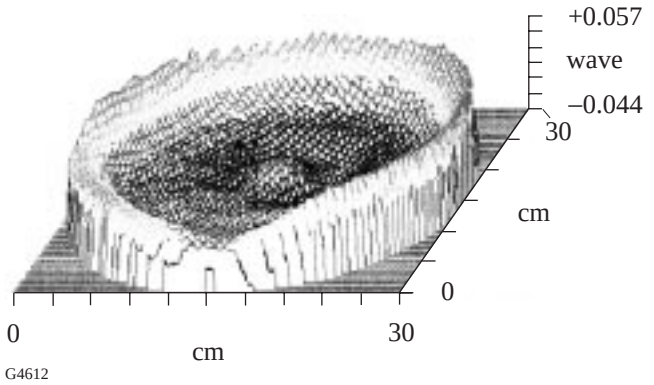

Figure 74.13
The surface figure of an etched photoresist coating measured in a phase-shifting interferometer. The surface figure prior to etching is subtracted from this measurement. The peak-to-valley and rms height values are 0.107 and 0.011 waves, respectively, measured at 633 nm. The overall power is removed from the data. Data from these measurements are combined with the total etch depth measured in the center to determine the etch uniformity in the following figures.

The plate is also tested at the center of the etched surface with a spectrometer to determine the total thickness of the photoresist coating before and after the etch. The total etch depth is found for the center and is combined with the interferometric data to generate a profile of the material removed by etching. This profile is divided by the average thickness of the etched material to provide a normalized etch uniformity for run-to-run comparison. Several profiles from the development and production phases are seen in Fig. 74.14. Figure 74.14(a) shows the convergence toward a good uniformity during the development phase. At the end of tuning the uniformity had a variation of less than 4%. Figure 74.14(b) shows the short-term stability (run-to-run) of uniformity attained during the final calibration sequence prior to etching the phase plates. The plots in Fig. 74.14(c) demonstrate the long-term stability of the etch uniformity over the 6-month production sequence of the phase plates. Stability was maintained by accurate positioning and pointing of the ion source and careful monitoring of the discharge electrical characteristics during source operation. Plots from the model in Fig. 74.12 suggest that maintaining pointing and position of the source to within a few millimeters should be adequate to limit variation in the uniformity to ±1%.

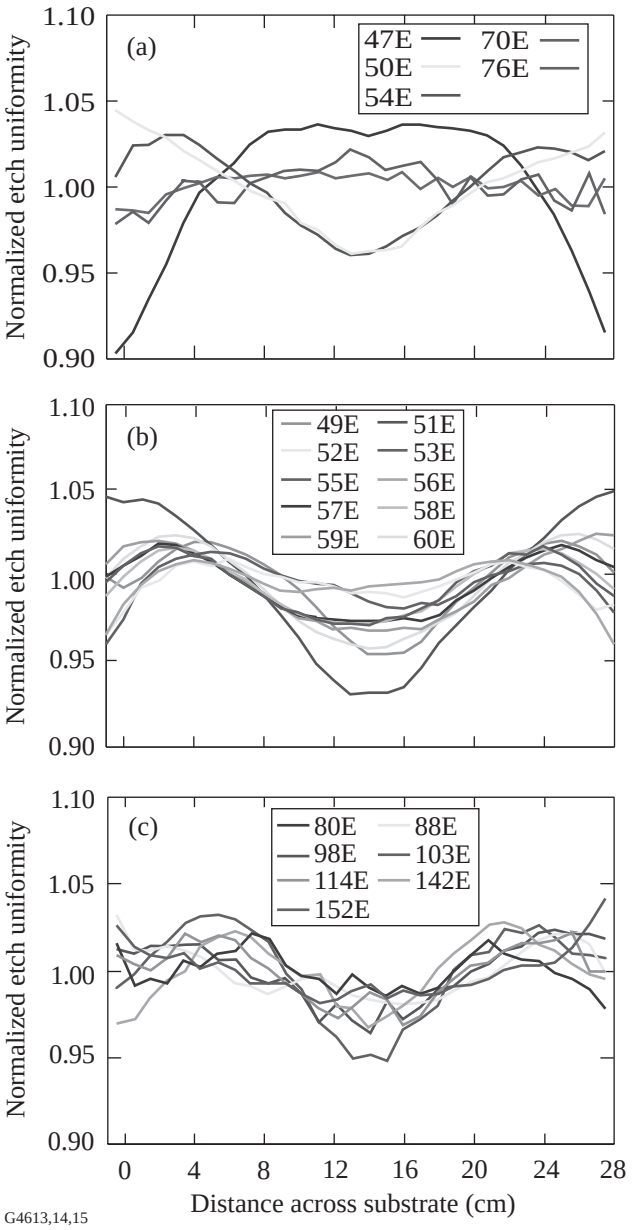

Figure 74.14
Plots of the normalized etch uniformity over the optic clear aperture during different phases of the project. (a) Good uniformity was achieved fairly quickly during the development stage as the ion source was adjusted to its final geometry. (b) The uniformity of sequential etch runs prior to production (calibration sequence) demonstrated the high repeatability of the process. The one run that deviated from ±2% was etched with a slightly different geometry. (c) The etch uniformity was very stable over the 8-month production period. The uniformity was periodically checked by etching flat, unexposed plates of photoresist. Gun position was checked frequently during production to maintain this uniformity. The numbers labeling the curves correspond to the sequential etch run for a given year.

Texturing Problems

Increasing surface roughness and scatter potentially limit the usefulness of ion-etch methods in optical applications. Surface texturing is well documented in ion-beam applications and has been attributed to several erosion-induced morphological changes including

a. development of cones and pyramids due to the angular dependence of the sputter yield;

b. faceting of different crystal planes in a polycrystalline material; and

c. redeposition of contaminating materials onto the mask and substrate. This causes local regions of different sputter yield that evolve into a structure surface.

The incidence angle tests were designed in part to test the effects of texturing from cause (a) listed above for silica and photoresist. Faceting (b) should not occur in either material since both are amorphous. Redeposition of metals, especially from tooling, was a concern and is addressed later. Other texturing effects in silica have been studied[9] but are generally found to occur at high incidence angles and at ion energies an order of magnitude higher than those used in this study.

The first experiments to probe the angle dependence on sputter yield tended to develop scatter on samples held normal to the ion beam and less so on the samples oriented at 60°, 50°, 40°, and 30° with respect to the incoming ion beam. The broad range of morphologies of the scatter in photoresist are seen in Fig. 74.15. The scanning electron micrographs (SEM) showed blistering in one view [Fig. 74.15(a)], while the other view [Fig. 74.15(b)] gave the impression of melting and flowing resist. Atomic force microscopy (AFM)[17] revealed high spatial frequencies in some areas of the photoresist scatter in Fig. 74.16(a). Areas where the photoresist had been fully eroded showed a different morphology [Fig. 74.16(b)]. The high spatial frequency component was absent here, and the surface was dominated by smooth, shallow depressions. The change of morphology of the silica surface is probably due to some planarization associated with the angular dependence of ions. This morphology occurred only in silica that was underneath the textured photoresist. Areas covered by only a very thin layer of resist showed no scatter related to etching. This evidence led to the conclusion that the photoresist was heating up, nearing its softening point, and beginning to flow during the etch.

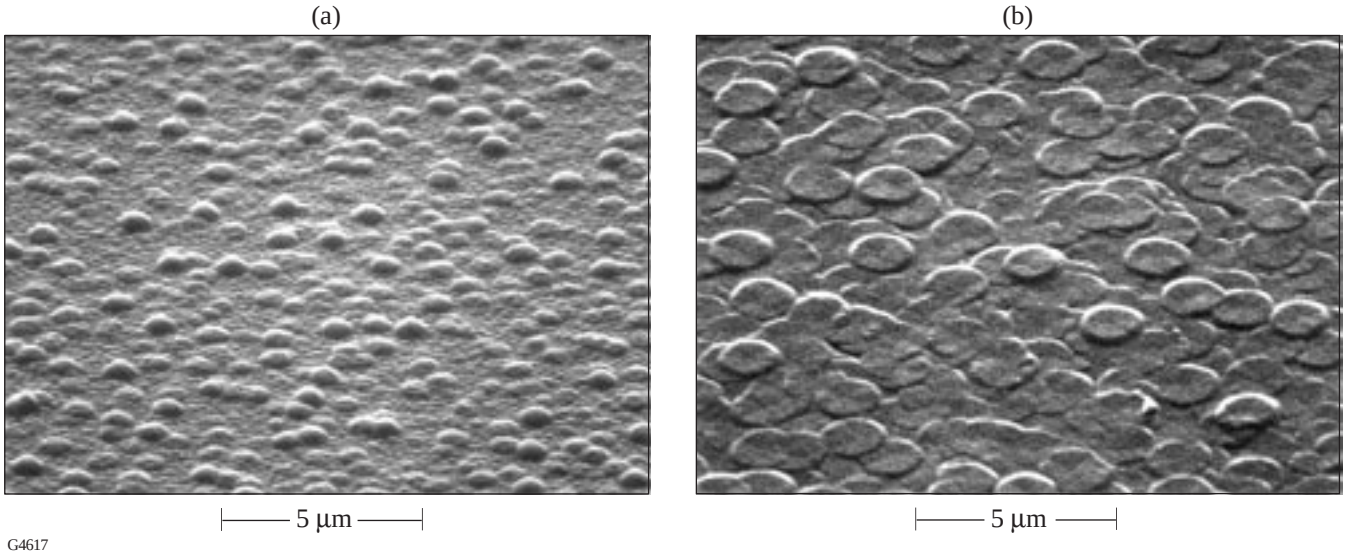

Figure 74.15
Scanning electron micrographs showing the different morphologies of high-scatter photoresist areas after etching. (a) and (b) are samples from ion-etch experiments to determine angular dependence of sputter (Fig. 74.9). The surface in (b) shows distinct signs of flow as the photoresist temperature rose during etching.

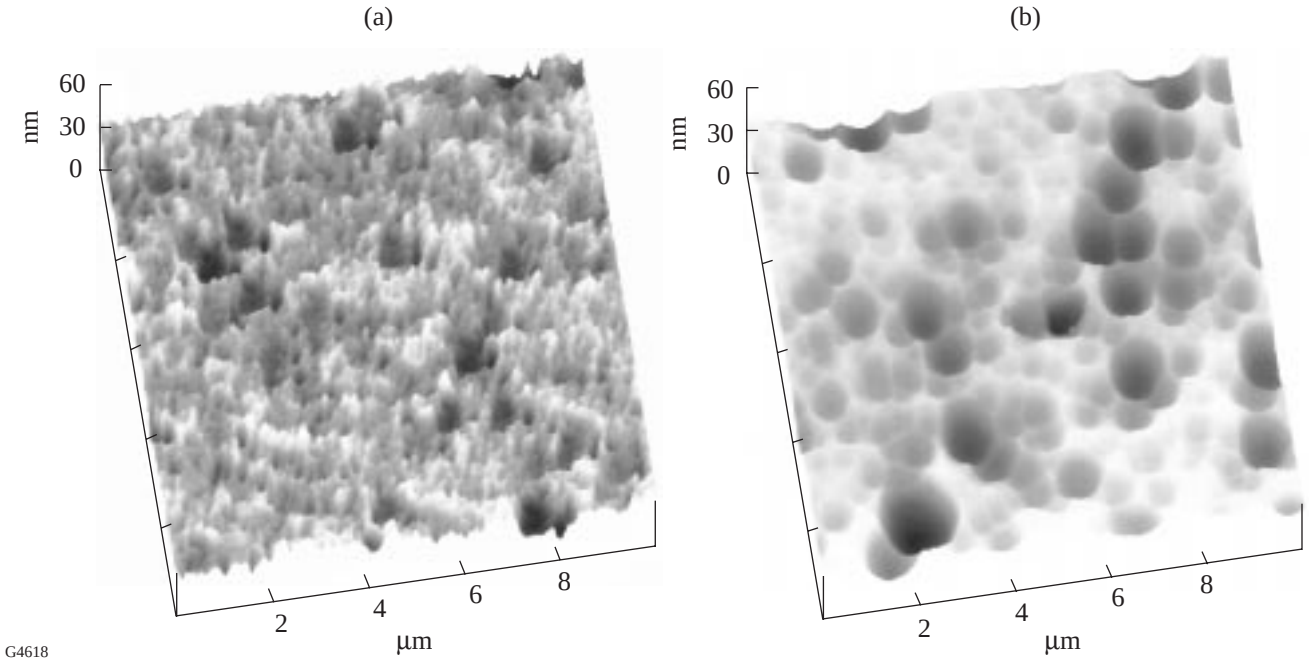

Figure 74.16
AFM scans of the surface of a 30-cm, partially etched substrate. High-scatter areas where photoresist remained (a) were measured as well as areas where photoresist was completely eroded away and only silica remained (b). The roughness in the resist area (a) seeded the topology of the SiO_2 surface (b). The morphology in the silica was then modified further by classical sputtering effects of angular dependence of sputtering, ion reflection, and redeposition.

The primary radiative thermal load during ion etching is the hot ion source and associated filaments. A secondary thermal load comes from the ion impingement, which provides an average energy of 0.1 W/cm^2 directly onto the surface of the resist; however, much of that energy is transferred by momentum to the etched molecule. In the angular dependence experiment the heat load would be largest for the substrate that had the largest amount of surface area exposed to the heat source, e.g., the normal incidence sample that typically had the highest scatter. To test this hypothesis a thermal sensor was placed directly above a rotating DPP master (a substrate with a full-thickness photoresist coating) to sense the temperature of the back of the substrate during etching. The temperature was monitored while the ion source was operated intermittently to allow the substrate to cool after a period of etching [Fig. 74.17(a)]. When the substrate was prevented from going above 50°C, the photoresist did not develop a textured surface. The surface of the photoresist layer must be significantly hotter

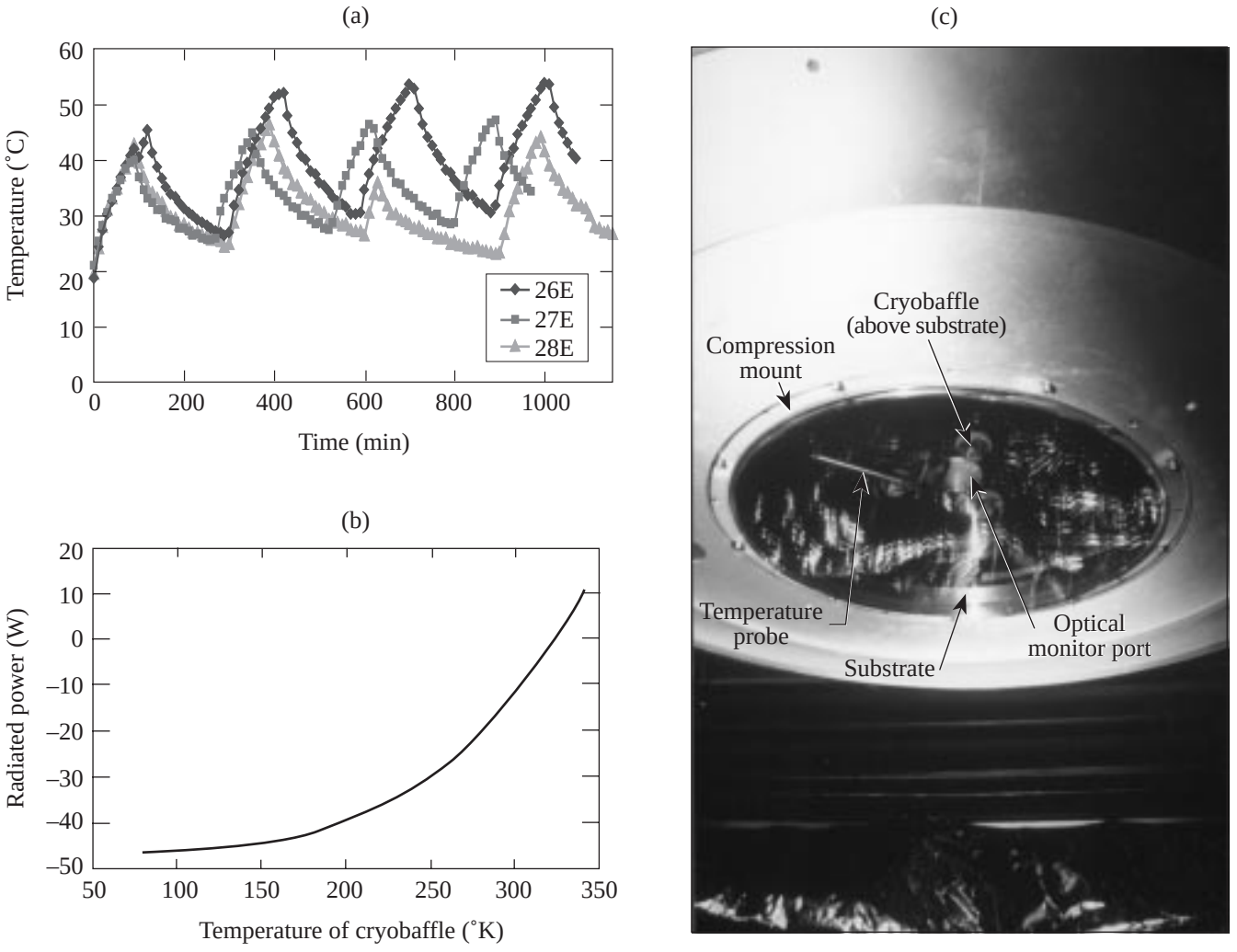

Figure 74.17
(a) The ion sources were operated intermittently in this test to allow the substrate to cool between etch cycles. The temperature of a probe close to the substrate is plotted versus time for several intermittent etch runs. Surface scatter in the resist became prominent when the measured probe temperature exceeded 50°C. A thermal load of 15 W (from the ion source) was calculated from the rate of temperature rise of the substrate. (b) The radiative heat transfer power of the cryobaffle on the back of the substrate has the capacity to cool the substrate if the baffle is cooled at liquid nitrogen temperatures. The calculation assumes the DPP is at 323°K and the emissivity of both the cryobaffle and the substrate are unity. (c) The DPP substrate is seen in the compression chuck. The cryobaffle is above the substrate with a temperature probe near the optical monitor port. The optic is held so it is the closest object to the ion source to prevent resputtering and redeposition from any metal hardware onto the optic surface.

than this measured temperature since softening temperatures for most resists exceed 120°C. This could not be confirmed because the front surface temperature of the rotating substrate could not be measured easily without disturbing other concurrent experiments. This test confirmed the suspicion that the texturing effect was due entirely to overheating of the resist during etching.

The immediate solution to the heating problem was to cryogenically cool the substrate from the back (top) surface. A 15-W heat load on the substrate was determined from the rate of temperature rise in the intermittent etch tests. The heat load could be reduced only by moving the ion source away from the substrate, which would result in excessively long etch runs. The thermal radiative power for two flat surfaces was found from the relationship

$$Q(T) = \sigma * \frac{T^4 - S^4}{\left[\left(\frac{1}{\varepsilon_1} + \frac{1}{\varepsilon_2}\right) - 1\right]} * A, \qquad (4)$$

where $\sigma = 5.6697 \times 10^{-8}$ W°K/m^2, T is the temperature of the cryobaffle, S is the maximum allowable temperature of the substrate (323°K), A is the substrate area, and ε_1 and ε_2 are the emissivity of the substrate and the cryobaffle. Both emissivity values were assumed to be unity since the peak wavelength of radiation will be in the 5- to 10-μm range. The cooling power of the cryobaffle as a function of the baffle temperature is given in Fig. 74.17(b). A cryobaffle was designed and fabricated[18] that had temperature regulation provided by a proportioning valve for liquid nitrogen and internal heaters [see Fig 74.17(c)]. The cryobaffle could be rapidly heated after the etch completion to prevent condensation on the substrate and excessive cooling of photoresist in partially etched plates. Temperatures of probes near the front surface and between the back surface and the cryobaffle were recorded for all etch runs.

The design of the substrate mount was driven by the need to thermally cool the optic from above, to hold the optic through a wide temperature range in case of ion-source failure, and to prevent redeposition onto the back of the substrate from scattered ions. In addition, resputtering of hardware onto the front surface of the substrate was to be avoided since it would both increase localized scatter and lower the damage threshold of the optic. The mount functioned as a compression chuck and used a polyetherimide[19] material to hold the optic [see Fig. 74.18(a)]. The optic surface was located well below all other hardware, which prevented resputtering of hardware material onto the surface. A conductive metal apron dropped down around the mount from the cryobaffle above to improve cooling of the mount.

The compression mount was tightened enough to prevent the optic from releasing during a worst-case condition where, if the cryobaffle failed, the optic and mount would heat to 80°C. The stresses of the mount on the optic were modeled using finite element analysis [Fig 74.18(b)] to ensure that the optic would not fracture when placed in the cold extreme of –80°C. The compressive stresses did not exceed 400 kg/cm^2, and the tensile stresses were less than 80 kg/cm^2 [SiO_2 strength is 11,000 kg/cm^2 (compressive) and 500 kg/cm^2 (tensile)].[20] The mount with an optic can be seen in Fig.74.18(c).

The surface scatter was visibly reduced in all etch runs that were cryocooled. The only exception occurred on some DPP's that were rotated too slowly during the etch cycle and others that did not cool well enough directly under the optical monitor port in the cryobaffle. (This caused local hot spots in the optic and very light scatter.) The total scatter from any plate never exceeded a loss of more than 1% at 351 nm. AFM scans of a typical and a worst-case surface are illustrated in Fig. 74.19. The typical low-scatter silica surface after removal of 5 μm of material had an rms roughness of 3.7 nm with peaks of 24 nm, and the worst-case area had an rms roughness of 4.14 nm with peaks of 60.8 nm. The isolated peaks in the worst case are assumed to be seeded by blisters in the photoresist.

Linearity

In a continuous profile optic, a linear removal rate between the photoresist and the silica is essential. If the process were not linear, it would be necessary to modify the original mask to compensate for the nonlinearity, and to tightly control the nonlinear process from run to run. Linearity was tested by using a calibration mask designed by LLE's Optical Imaging and Sciences Group [Fig. 74.20(a)]. This mask produces a linear ramp in resist, a stepped ramp, and several steps in different locations in the aperture. It also has a flat region across the center that can be used to measure etch uniformity. The ramp region, which was the most useful, was measured on an interferometer[21] before and after etching. A typical result from the measurement is seen in Fig. 74.20(b).

The ion-etch pattern faithfully reproduced the ramp in the photoresist master. The normalized measured ramps of the photoresist ramp and the etched silica ramp from this master are compared in Fig 74.20(c). The departure from the photore-

sist curve for the thicker resist is due to some residual spatial nonuniformity that existed in the process at the time of the test. The ratio of the slopes of the silica ramp to the photoresist ramp was approximately 1.3 during a calibration sequence just before production. This value represents the etch ratio of the two materials and depends on the photoresist type, resist bake parameters, ion incidence angle, and ion energy. The higher etch rate in the silica allowed for the use of lower thickness photoresist coatings and reduced exposure times to the mask for a given desired spot size of the DPP. The final resist thickness for this design was 3.5 μm, which produced a 5-μm peak-to-valley pattern in the silica. The ramp of the silica is plotted against the straight line target in Fig 74.20(d). The linearity seen in this graph is a result of careful compensation for nonlinearities in all stages of mask manufacture, including film response and photoresist response.

Near-Field Defects

Near-field defects are small-scale regions of high slope in the surface of the distributed phase plate. They are caused by either defects in the photoresist spinning process or imperfections in the mask used to expose the photoresist. Near-field defects produce regions of high intensity fairly close to the DPP surface, which could damage other optics in the vicinity.

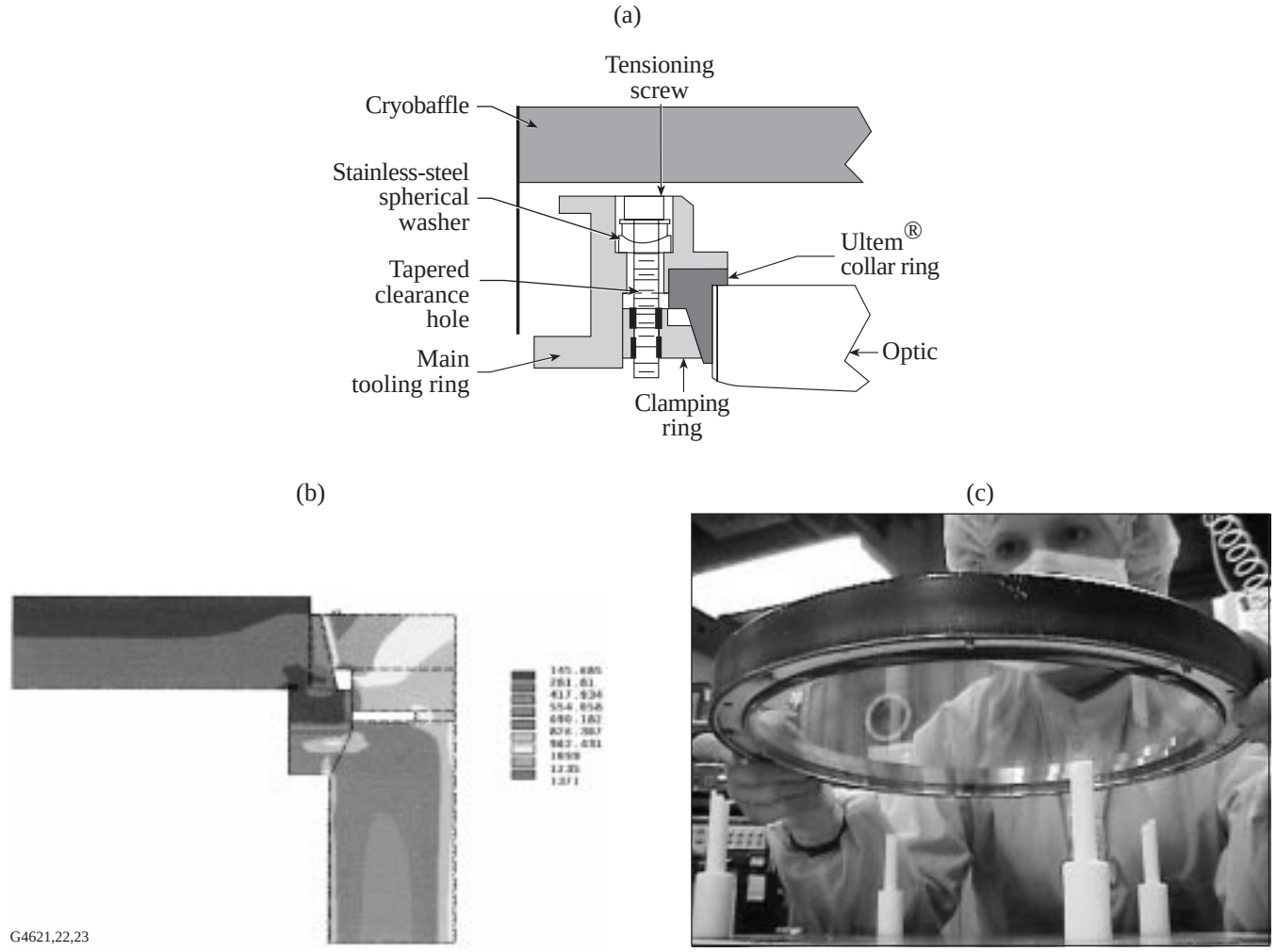

Figure 74.18
(a) The vacuum chuck holds the optic in compression with a Ultem® polyetherimide collar. The substrate mount acts as a barrier for ions traveling to the back surface; it also allows rear radiative cooling and optical monitoring through the optic. (b) Finite element analysis of the substrate in a fully tightened and cooled (–80°C) chuck determined that stresses in the optic would be well below the tensile strength of fused silica. The chuck is tightened enough to prevent the optics from falling out at the high-temperature extreme (+80°C). (c) A close-up view of the chuck on a mounting jig shows the optic, the Ultem® ring, and the tensioning screws. The mount is painted black to increase the infrared emissivity of the aluminum.

In OMEGA, near-field defects could damage the aspheric focusing lens, which is approximately 150 mm in front of the DPP. This lens is both expensive and difficult to replace.

During the production of the first set of replicated DPP's made in epoxy, the near-field defects were removed by locally altering the topography around the defect. Several methods for achieving this were attempted and tested by placing a repaired DPP and a surrogate focus lens in a full beam of OMEGA. The technique that prevailed in both the epoxy and the photoresist materials was to use a hot, blunt point to change the topography of the epoxy by melting. In these cases, the light striking the repaired area is scattered into a wide angular area. The repaired defect areas appear as small holes in the propagating beam.

For etched DPP's, near-field defects were repaired by altering either the photoresist master prior to etching or the fused-silica surface after etching. In silica the near-field defects were repaired by localized grinding with a small dental grinder. Since the etch ratio of silica to the photoresist is 1.3:1, a defect that causes a small modulation in photoresist will turn into a defect with a larger modulation in silica. For this reason, when making etched DPP's, it was preferable to inspect and repair the final etched surface.

DPP's were first inspected for near-field defects in a collimated beam at $\lambda = 442$ nm, which is fairly close in wavelength to the 351-nm wavelength of the OMEGA laser but still visible to the unaided eye. A shadow image of the collimated beam was examined against a white background at a distance of ~150 mm beyond the part. After mapping out the near field for regions of high intensity, a quantitative measure of intensity from each defect was obtained with a CCD camera in the near-field plane (see Fig. 74.21). If the near-field defect caused a peak intensity that exceeded the background by a factor of 3, the defect was marked and removed by grinding [see Fig. 74.21(c)]. During production, plates typically exhibited five to ten defects. Plates with as many as 20 defects were repaired and used on OMEGA. Near-field defect repair was one of the most time-consuming and labor-intensive operations in the manufacturing of DPP's. After being repaired, the optic was cleaned and sol-gel coated by dip coating.

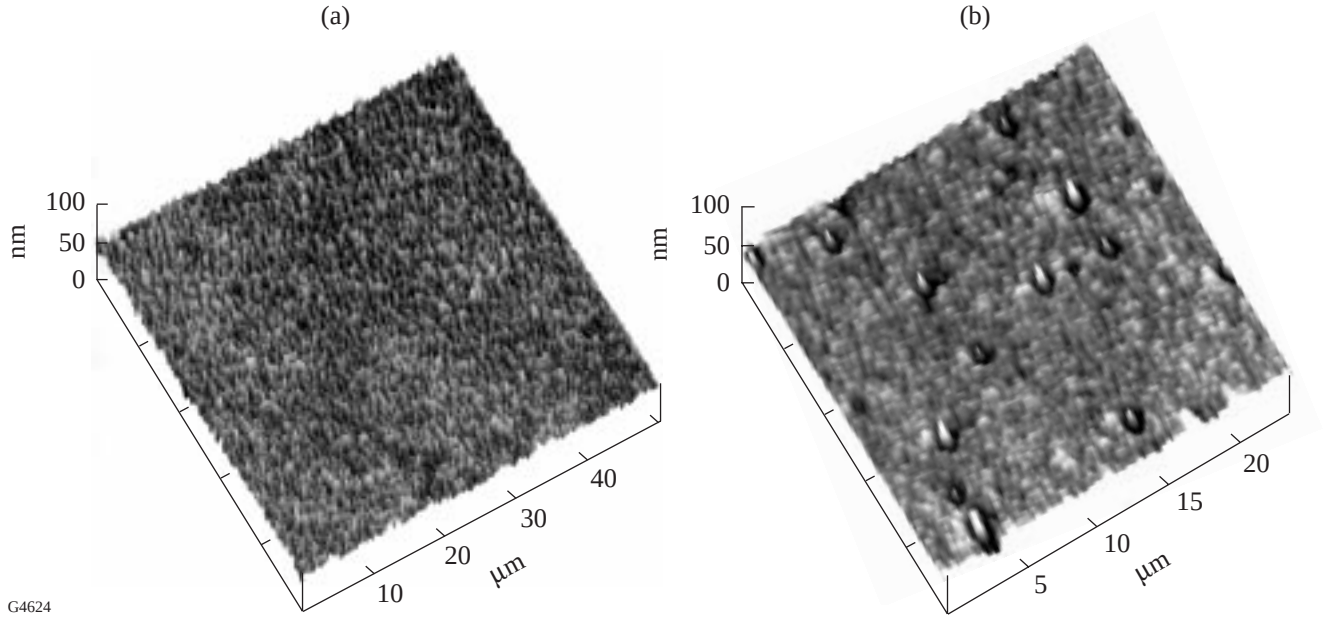

Figure 74.19
(a) The improved surfaces of a DPP cooled during etching can be seen in this AFM scan of a low-scatter area. The rms roughness = 3.4 nm; the P–V roughness = 24.5 nm. (b) AFM scan of worst-case scatter on a production DPP. Scatter was associated with a region that would not have been effectively cooled by the cryobaffle, such as the optical monitor port. The rms roughness = 4.1 nm; the P–V roughness = 60.8 nm. Isolated defects cause most of the scatter losses from this surface. Note the different scale lengths in the two AFM images.

Production Process/Results

A schematic of the full ion-etch system is shown in Fig. 74.22(a). The geometry of the ion source and the substrate can be seen in the photograph of the vacuum chamber's interior [Fig 74.22(b)]. A control program that would shut off the source after a set interval monitored the ion source. The program would terminate the etch if the ion source operated outside the prescribed parameter space for the ion-beam neutralizer emission current and the accelerator (grid) current. The chamber was loaded during the day and operated at night. A typical 14-h etch run included time to heat up the cryobaffle and the substrate to room temperature before removing the part for testing the next morning.

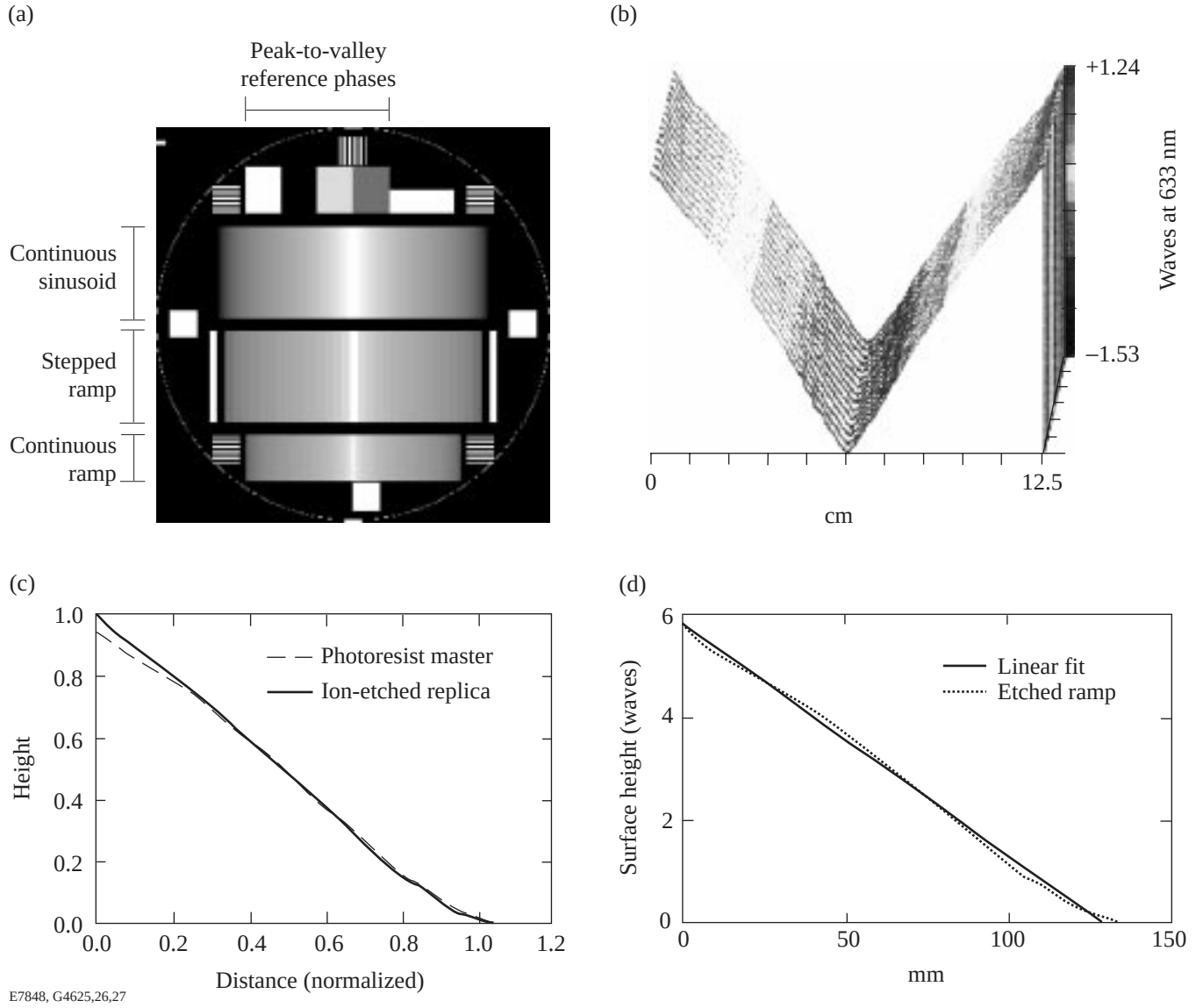

Figure 74.20

(a) The calibration mask is used to characterize both lithographic and etch nonlinearities. (b) A typical interferometric measurement of a continuous calibration ramp. (c) The measured continuous ramps for both silica and photoresist are closely matched and therefore indicative of a highly linear process. The heights are normalized for easy comparison. (d) The etched ramp is compared to a desired linear ramp. The final result includes errors of the entire DPP process, including the film errors from several stages of mask writing and enlarging, photoresist errors, and final etching.

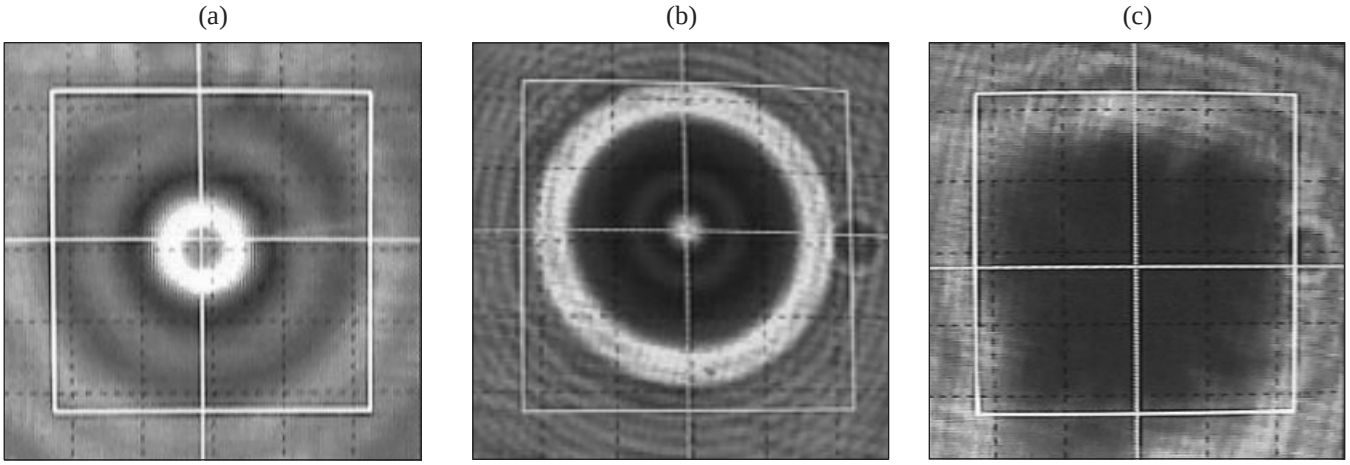

Figure 74.21
A CCD camera is used to analyze individual defects. Several type of near-field defects are found in the DPP's, including lenslets (a), comets (b), goobers, worms, and dirt (last three not illustrated). The final frame (c) shows the near-field result after repair.

An optical monitor measured the thickness of photoresist during an etching run to determine the etch rate and assist in endpoint determination. The DPP design was modified to produce the thickest area of photoresist in the center of the substrate, which was made to coincide with the center of the substrate rotation. A white-light beam was co-aligned with this point to allow for continuous monitoring by interference through the photoresist. The beam entered a monochromator/detector combination, and the signal was fed into a strip chart recorder. The etch rate derived from this measurement proved to be a good indicator of ion-source performance. Ion etching would continue for 30 min after the interference signal ceased to ensure that all the photoresist was removed.

The full production process for DPP's is summarized in the flowchart in Fig. 74.23. The process requires that a photoresist master be made for each etched phase plate. The DPP's for OMEGA were produced over a period of 19 weeks. During this time 79 successful etch runs—66 DPP's and 13 calibration or uniformity checks—were completed. Maintenance occurred on 9 days, and 5 etch runs resulted in failures. A high level of preventive maintenance was performed on the vacuum pumping system and the mechanical components just prior to the final calibration sequence.

Laser-induced-damage thresholds of ion-etched silica always increased when care was taken to prevent the occurrence of redeposition from sputtered tooling. Ion-etched samples of Corning 7940 fused silica were damage tested at 1ω and 3ω with 1-ns pulses. The results are compared to polished and cleaved surfaces in Fig. 74.24. The damage thresholds of the ion-etched surfaces increased over polished surfaces but were less than those for a freshly cleaved surface. The current explanation for the increase is that polishing processes produce both a hydrated layer and a layer of subsurface fractures that can trap absorbing contaminants during the polishing process. The ion-etch process removes the hydrated layer and the layer of fractures and associated contaminants, while the relatively low-energy ions do not penetrate and disrupt the structure near the surface.

A DPP's optical performance can be evaluated by examining the minimum spot size it produces when used in a focusing system similar in aperture and focal length to that found on OMEGA (265-mm aperture, 1800-mm focal length). The spot size is measured at the width corresponding to 5% of the maximum energy. A Gaussian function is fit to the measurement, and the order n (shape) of the function is found. The results for both the replicated epoxy and ion-etched DPP's are given in Table 74.I, and histograms for both DPP types are given in Fig. 74.25. The etched DPP's had a more consistent spot size than the replicated DPP's. Note that the target size had changed between the time the two sets were made. The Gaussian order for the ion-etched set was lower that the target value of 3, but most of those variations were probably due to errors in the mastering process and are not inherent to etching.

(a)

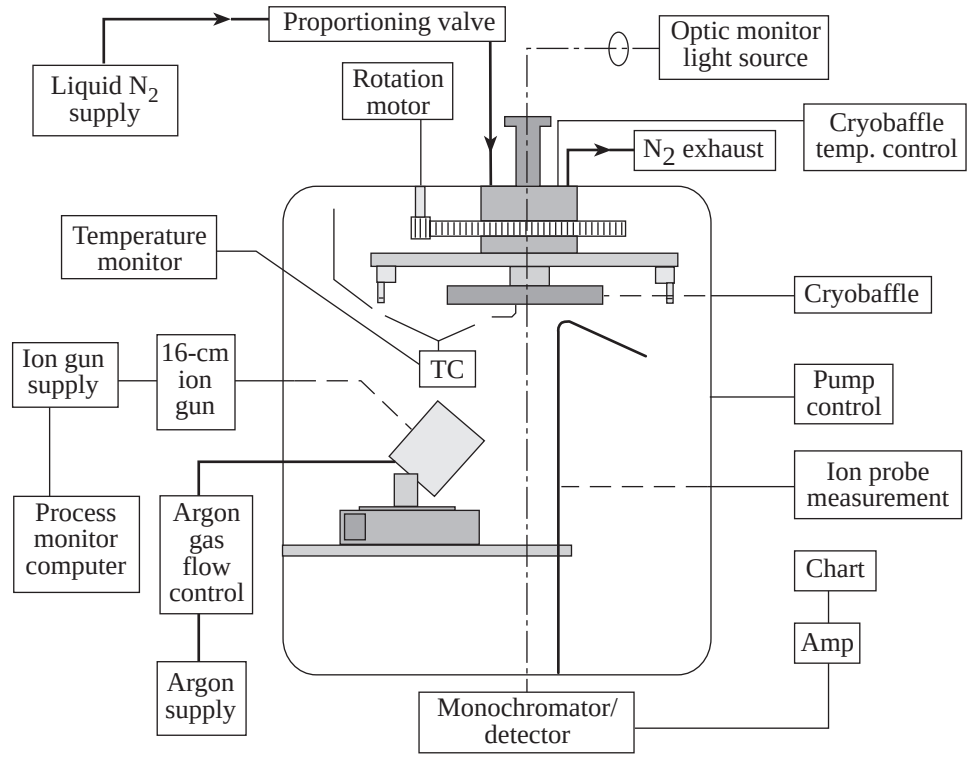

(b)

G4629,30

Figure 74.22
(a) Schematic of the LLE/OMAN 16-cm-ion-source etching system. The system was operated continuously for 14 h during each etch. (b) The 16-cm ion source (below) is shown on a rail in the 54-in. chamber with a substrate in the rotation fixture (above).

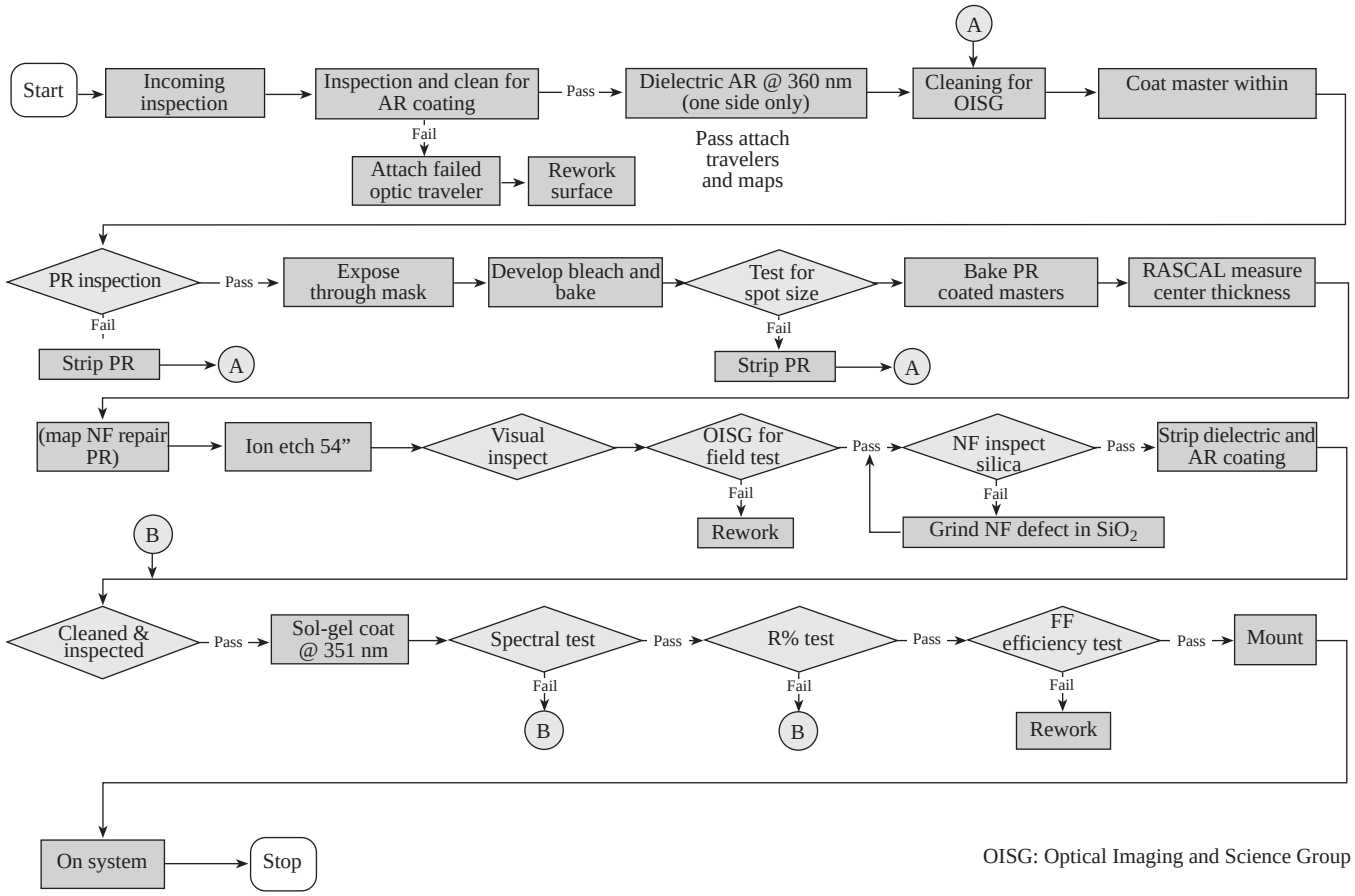

Figure 74.23
Flowchart of etched DPP production steps. The substrates were coated initially with a durable antireflection coating to reduce interference effects during exposure of the photoresist.

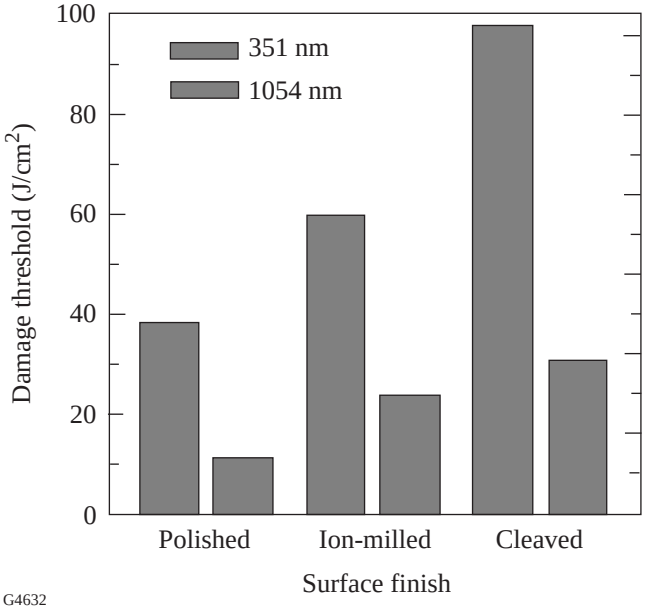

Figure 74.24
Ion etching improves the damage threshold at both 1ω and 3ω for 1-ns pulses.

The transmission through a DPP was measured by collecting all of the energy in the spot using an oversized detector and then reducing the aperture of the detector to 1 mm. The first measure indicates the performance of the sol-gel coatings and scatter characteristics of the piece. The second measure gives the energy likely to impinge on a target and is more relevant to performance on OMEGA. The distribution of the 1-mm aperture measurements for the 60 DPP's used on OMEGA is seen in Fig. 74.26. The plates are near the theoretical maximum transmission for the Gaussian order of $n = 2.44$.

Conclusion

Inert ion etching is a powerful tool for use in manufacturing DPP's for high-peak-power lasers. In concert with gray-level photoresist methods developed at LLE, it provides a method of transferring any continuous function onto an optical surface. The development and production time of 15 months was relatively short given the excellent performance of the devices.

The inert-ion-etching process may be invaluable as a tool for increasing the damage threshold of silica surfaces in both

Table 74.I. Comparison of performance results for 60 etched DPP's manufactured for OMEGA and earlier replicated epoxy DPP's.

	Etched DPP's		Epoxy DPP's	
	Mean	1 σ	Mean	1 σ
Minimum spot size, μm	936.7	14.1	635.8	37.6
Gaussian order	2.44	0.07	~	~
Full transmission	0.994	0.004	Degraded	~
T @ 1-mm aperture	0.959	0.006	~	~

~ no data available.

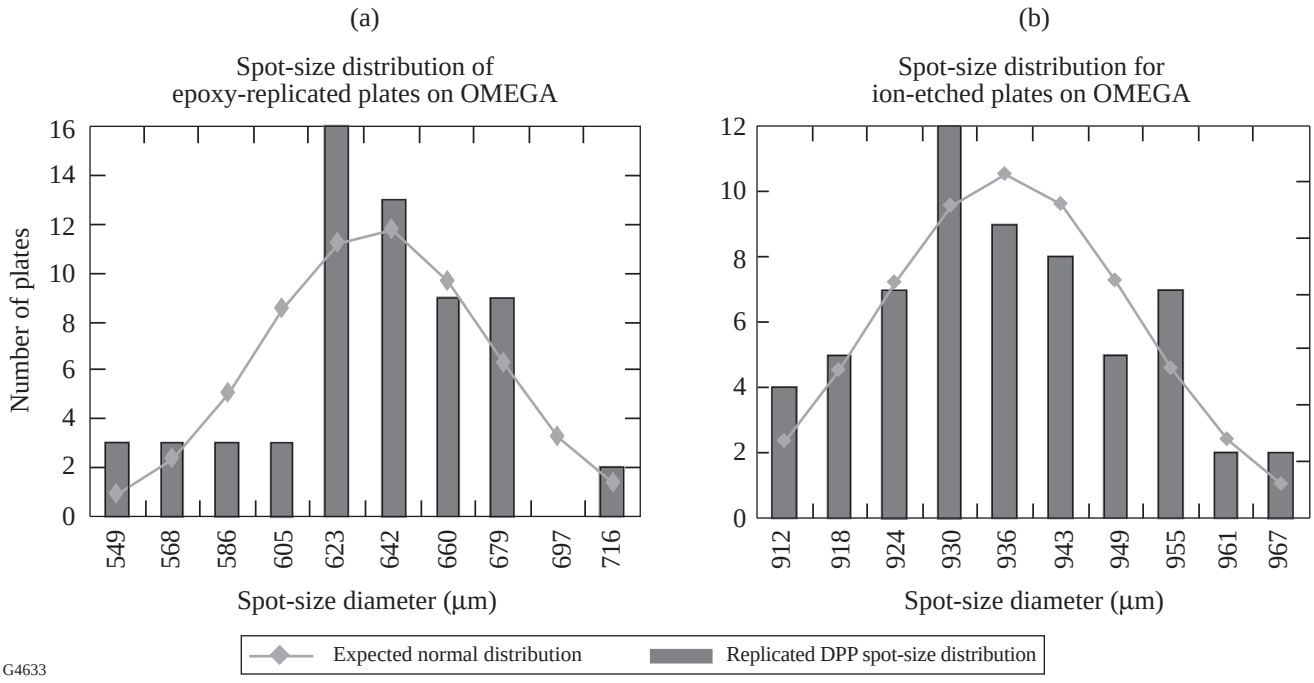

Figure 74.25
The far-field spot size (at the 5% of maximum width) was measured for each DPP. The distribution of spot sizes for the epoxy-replicated DPP's (a) was much broader than in the ion-etched DPP's (b).

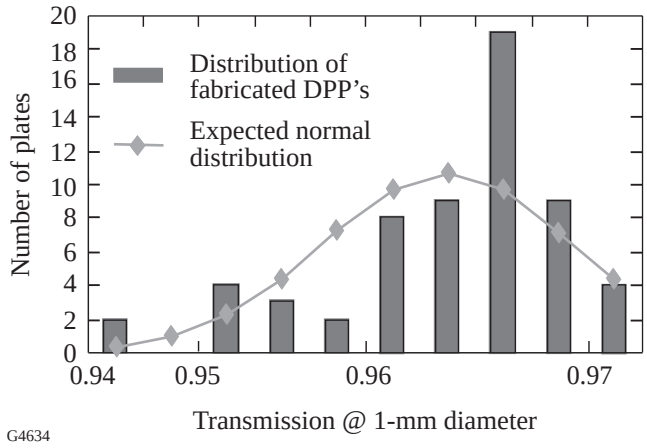

Figure 74.26
Despite some loss due to the near-field defect repairs and slight scatter, the transmission was near the maximum value possible for this Gaussian order. The DPP design requires that some of the energy be sent outside the target.

the infrared and the UV. Ion etching will be tested on other components of OMEGA to assess its capabilities for raising laser-damage thresholds.

ACKNOWLEDGMENT

This work was supported by the U.S. Department of Energy Office of Inertial Confinement Fusion under Cooperative Agreement No. DE-FC03-92SF19460, the University of Rochester, and the New York State Energy Research and Development Authority. The support of DOE does not constitute an endorsement by DOE of the views expressed in this article.

REFERENCES

1. Laboratory for Laser Energetics LLE Review **65**, 1, NTIS document No. DOE/SF/19460-117 (1995). Copies may be obtained from the National Technical Information Service, Springfield, VA 22161.

2. Laboratory for Laser Energetics LLE Review **71**, 101, NTIS document No. DOE/SF/19460-186 (1997). Copies may be obtained from the National Technical Information Service, Springfield, VA 22161.

3. Laboratory for Laser Energetics LLE Review **64**, 170, NTIS document No. DOE/SF/19460-99 (1995). Copies may be obtained from the National Technical Information Service, Springfield, VA 22161.

4. Y. Lin, T. J. Kessler, and G. N. Lawrence, Opt. Lett. **20**, 764 (1995).

5. G. K. Wehner and G. S. Anderson, in *Handbook of Thin Film Technology*, edited by L. I. Maissel and R. Glang (McGraw-Hill, New York, 1983), p. 3-17; G. C. Schwartz, in *Handbook of Semiconductor Interconnection Technology*, edited by G. C. Schwartz, K. V. Srikrishnan, and A. Bross (Marcel Dekker, New York, 1998), pp. 1–76.

6. O. Auciello and R. Kelly, eds., *Ion Bombardment Modification of Surfaces: Fundamentals and Applications*, Beam Modification of Materials, Vol. 1 (Elsevier, Amsterdam, 1984).

7. B. A. Banks, in *Handbook of Ion Beam Processing Technology: Principles, Deposition, Film Modification, and Synthesis*, edited by J. J. Cuomo, S. M. Rossnagel, and H. R. Kaufman (Noyes Publications, Park Ridge, NJ, 1989), pp. 338–361.

8. E. Chason and T. M. Mayer, Appl. Phys. Lett. **62**, 363 (1993).

9. T. Motohiro and Y. Taga, Thin Solid Films **147**, 153 (1987).

10. S. R. Wilson *et al*., in *Science of Optical Finishing*, Vol. 9, 1990 Technical Digest Series (Optical Society of America, Washington, DC, 1990), p. 73.

11. H. R. Kaufman, R. S. Robinson, and W. E. Hughes, *Characteristics, Capabilities, and Applications of Broad-Beam Sources* (Commonwealth Scientific Corporation, Alexandria, VA, 1987).

12. J. M. E. Harper, J. J. Cuomo, and H. R. Kaufman, J. Vac. Sci. Technol. **21**, 737 (1982).

13. H. R. Kaufman, *Fundamentals of Ion-Source Operation* (Commonwealth Scientific Corporation, Alexandria, VA, 1984).

14. Commonwealth Scientific Corporation, Alexandria, VA 22314-1974.

15. O. Auciello, in *Ion Bombardment Modification of Surfaces: Fundamentals and Applications*, edited by O. Auciello and R. Kelly, Beam Modification of Materials, Vol. 1 (Elsevier, Amsterdam, 1984), Chap. 1; G. Carter and M. J. Nobes, *ibid*., Chap. 5.

16. M. Jin, "Numerical Estimation for 8-cm Ion Source Distribution," Internal Memo, Laboratory for Laser Energetics, University of Rochester (8 August 1991).

17. Atomic force microscope contact mode, Model NS3, Digital Instruments, Inc., Santa Barbara, CA 93117.

18. Vacuum Process Technology, Pembroke, MA 02359.

19. Ultem®-Polyetherimide, available from Design Engineering Plastic Products, Reading, PA 19612-4233.

20. Fused silica available from Technical Products Division, Advanced Products Department, Corning Glass Works, MP-21-4, Corning, NY 14831.

21. Zygo Mark IVxp, Zygo Corporation, Middlefield, CT 06455.

A High-Resolution X-Ray Microscope for Laser-Driven Planar-Foil Experiments

A soft x-ray microscope ($E \lesssim 3$ keV) with high spatial resolution (~3 μm) has been characterized at LLE and used for initial experiments on the OMEGA laser system to study the hydrodynamic stability of directly driven planar foils. The microscope, which is an optimized Kirkpatrick-Baez (KB)–type design, is used to obtain four x-ray radiographs of laser-driven foils. Time-resolved images are obtained with either custom-built framing cameras (time resolution ~80 ps) or short-pulse backlighter beams ($\Delta t \lesssim 200$ ps). In the former case, a spatial resolution of ~7 μm was obtained (limited by the framing camera), while in the latter case a resolution of ~3 μm was obtained. This article details the testing, calibration, and initial use of this microscope in the laboratory and on OMEGA.

Recent experiments studying the hydrodynamic stability of laser-driven planar foils[1–7] have relied on the technique of time-resolved x-ray radiography as a method of diagnosis. The short time scales (~ ns) require the use of a laser-generated x-ray backlighter, while the small spatial scale lengths (~ μm) require a high-spatial-resolution imaging system. In a radiograph of a perturbed driven foil undergoing unstable growth, the modulation depth (the desired observable) is affected by the resolution (modulation transfer function) of the imaging system.[8] This is typically limited by the imaging system itself (pinhole resolution in the case of pinhole imaging) or additionally by the recording system blurring (as is typically the case when using framing camera or streak camera imaging). Systems used to record radiographs of laser-driven foils range from simple pinhole cameras coupled to x-ray framing cameras to Wolter microscopes coupled to streak cameras. A good example of the resolution obtainable with a pinhole–framing camera combination is described in Robey *et al.*,[9] where 5- to 10-μm-diam pinholes in combination with framing cameras at magnifications up to 12× yield a spatial resolution approaching 10 μm. Remington *et al.*[10] describe the measured resolution of the Nova 22× Wolter microscope, which has an ultimate resolution of ~2 to 3 μm but is not easily adaptable to multiple-frame, two-dimensional imaging. More recently, monochromatic imaging using bent crystals as the imaging device has been applied to flat-foil experiments.[7] Resolution approaching ~3 μm has been reported. Kodama *et al.*[11] report on an advanced Kirkpatrick–Baez (AKB) microscope, which consists of four mirrors producing a single image. This microscope has a quoted resolution of ~3 μm or better over an ~1-mm-diam region.

This work describes the characterization of a KB microscope configured to provide high-spatial-resolution (~3-μm), low-energy (≲3-keV), multiple framed images (Δt ~ 80 ps) of x-ray-backlit, laser-driven foils. This KB microscope optical assembly consists of glass reflecting surfaces assembled without an additional metal coating. As will be shown below, the uncoated reflecting surfaces provide a convenient high-energy cutoff at ~3 keV, which is appropriate to both the backlighter spectrum and the subjects of the radiography (plastic foils). The detailed design is further described in Marshall and Su.[12] Time resolution can be obtained by either custom framing cameras (developed at the Los Alamos National Laboratory[13]) or a novel, multibeam, short-pulse (~100-ps) backlighter irradiation scheme. This KB microscope will be used in future planar-foil stability experiments on the University of Rochester's OMEGA laser system.[14]

Characterization of the Microscope

The microscope used for these experiments was built and assembled by Sydor Optics.[15] It consists of four mirrors arranged in a stack of two perpendicular pairs (Fig. 74.27) that produce four images of laser–plasma x-ray emission. Images are formed by two perpendicular reflections at a mean grazing angle of ~0.70°. The super-polished reflecting surfaces (surface roughness < 4 Å) are concave with radii of curvature r = 26 m and a thickness along the optical axis of 4.5 mm. [Previously reported mirror assemblies (Ref. 12) had a thickness of 9 mm, resulting in a larger solid angle but also larger measured and calculated off-axis aberrations.] The surfaces perpendicular to the reflecting surfaces are also super polished and are used to optically contact the mirrors into a fixed, stable assembly. The images formed by the KB microscope obey the focus equation[16]

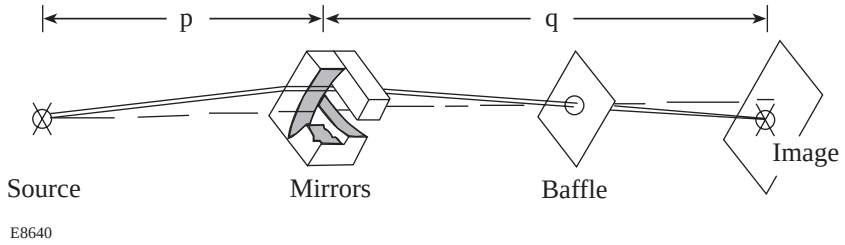

Figure 74.27
Schematic of the KB microscope optical assembly.

$$\frac{1}{p}+\frac{1}{q}=\frac{2}{R\sin i}, \tag{1}$$

where p is the distance from the object to the mirror assembly, q is the distance from the mirror assembly to the image, i is the grazing angle, and R is the radius of curvature of the mirrors. The distances p and q in Eq. (1) refer to the distance from the center of the assembly, i.e., between the pairs of perpendicular mirrors. The mirror separations have been adjusted (as described in Ref. 12) so that the focus of the first reflecting surface is coincident with the second reflecting surface. The best-focus distance at a magnification of 13.6 was found to be p = 179.3 mm. The solid angle subtended by each reflecting pair as seen from the source is $\sim 9\times 10^{-8}$ sr for this case.

After assembly the KB microscope was first characterized in the laboratory using a cw, e-beam-generated x-ray source. The e-beam impinged on a water-cooled tungsten target after passing through a bending magnet whose purpose was to prevent ion contamination of the target area. Typical e-beam voltage settings of 10 kV were used in all tests, producing a continuum x-ray source up to 10 keV. Images were recorded on Kodak DEF direct-exposure film after passing through a 1-mil (25.4-μm) Be window placed near the optic baffle. Figure 74.28(a) shows one of four such images taken of a 500-mesh Cu grid (0.001-in.-diam Cu wires spaced by 0.002 in., i.e., 500/in.) placed at the best focus of the microscope. A hole was placed in the grid [visible in Fig. 74.28(a) as a dark irregularly shaped region] as a position reference from image to image. The resolution as a function of position was determined from photomicrodensitometer (PDS)-digitized grid images. A Perkin–Elmer PDS with a 0.25 NA lens, and a scanning aperture of 10 μm, was used to digitize the images. Figure 74.28(b) shows a horizontal lineout through the image of Fig. 74.28(a) and just below the reference hole. The values are computed intensity in ergs/cm^2 versus position in μm [assuming a photon energy of 2 keV (see the energy response calibration later in this section) and using the semi-empirical formula of Henke *et al.*[17]]. The lineout has been averaged over the width of the space between the wires and median filtered to reduce point-to-point noise. The remaining pattern shows the overall resolution of the image near best focus. Figure 74.28(c) shows an enlargement of the lineout at the edge of the shadow of one wire. The width of the shadow is ~3.7 μm. This measurement was repeated across the image, yielding the resolution as a function of position [Fig. 74.28(d)]. The resolution thus measured closely follows that computed by ray tracing (solid line). Diffraction of soft x rays ($\lesssim$1.5 keV) will contribute to image blurring at best focus. The dotted line in Fig. 74.28(d) indicates the approximate effect of diffraction on the resolution for an assumed energy of 1.25 keV (worst case, i.e., lowest practical energy to be used). Diffraction is seen to limit the resolution to ~2 μm for such soft x rays. The measured resolution of 3 μm at best focus indicates that the optical system is limited to $\geq$1.5 times the diffraction limit. For comparison the resolution that would have been obtained if 9-mm-thick mirrors had been used is shown in Fig. 74.28(d) as a dot–dashed line. The smaller mirrors clearly provide a more optimum on-axis and off-axis resolution at the expense of solid angle.

The edge response function ε of the microscope (image of the shadow of the edge of a wire) is given by

$$\varepsilon(x)=\int_{-\infty}^{x}\ell(x')dx', \tag{2}$$

where ℓ is the line spread function, which is itself a function of x and y, but assumed to vary slowly. We can make the simplifying assumption that the point spread function (PSF) is given by the product of the line spread functions in the two perpendicular directions x and y. This is a good assumption provided the axes x and y are aligned along the axes of the microscope mirrors, as is the case for all of the images analyzed in this article. The PSF is thus computed from the observed edge response function by differentiation. The result of one such computation from the image of Fig. 74.28(a) near best focus is shown in Fig. 74.29(a). The computed PSF has a full width at half-maximum of 3.0 μm. Figure 74.29(b) shows the modulation transfer function (MTF)

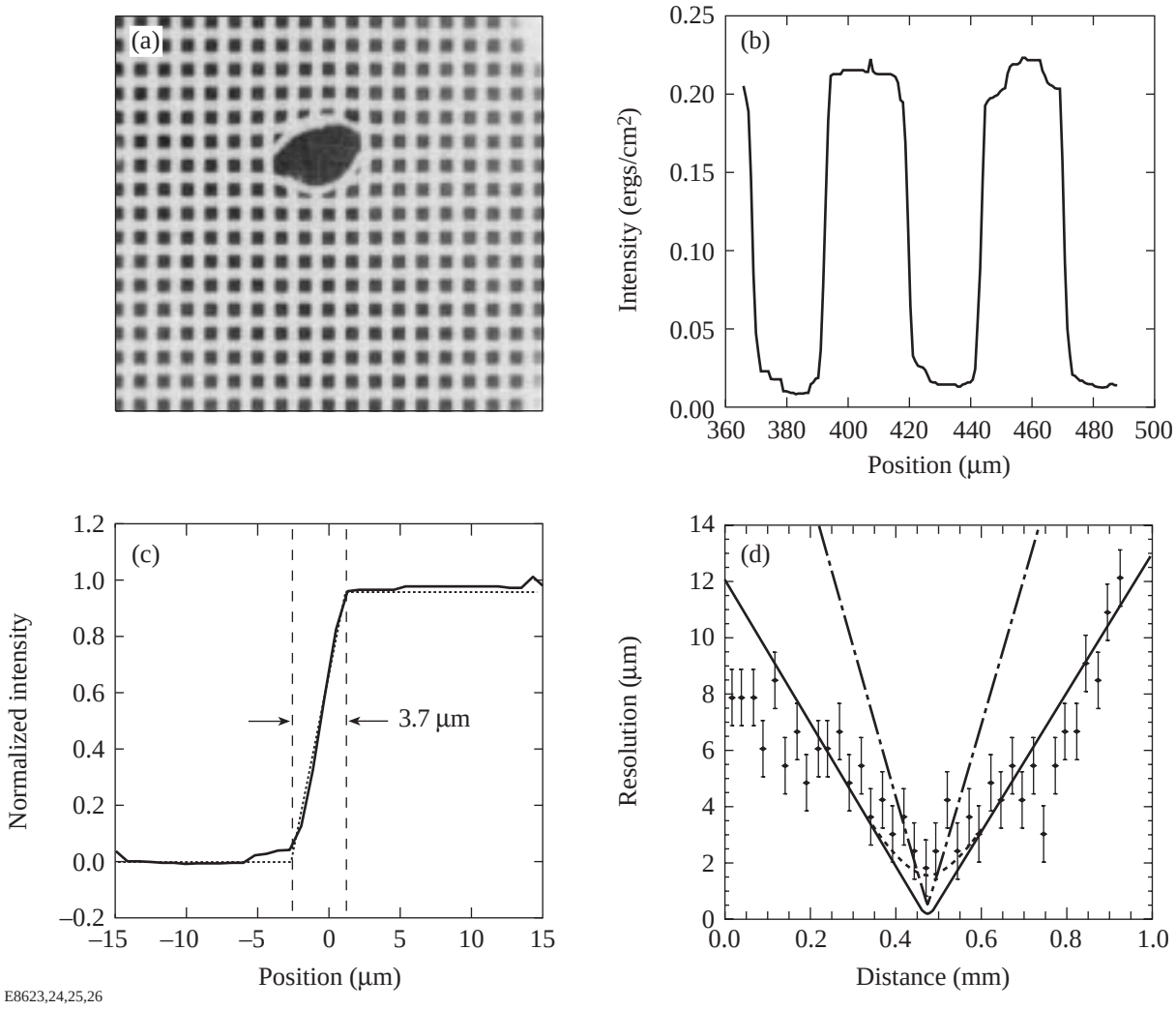

Figure 74.28
Laboratory tests of imaging with the KB microscope. (a) Image of a backlit Cu mesh taken with a cw x-ray source; (b) lineout below hole in grid passing through best focus; (c) enlargement of lineout near best focus; (d) width of the shadow of each wire versus position in the object plane of (a). The solid line is the resolution computed by ray tracing; the dotted line includes the effect of diffraction by 1.25-keV x rays. The dot–dashed line is the resolution computed by ray tracing for 9-mm-thick mirrors (as used in Ref. 12).

$$\mathrm{MTF} = F\left[\mathrm{PSF}(x)\right], \tag{3}$$

computed from the PSF by Fourier transform as a function of position about best focus. The ideal MTF of a pinhole camera with a 10-μm aperture at comparable magnification is shown for comparison.

Framed imaging with the KB microscope is accomplished with a pair of custom microchannel plate (MCP)–based cameras built at the Los Alamos National Laboratory[13] and originally designed to be used in the gated monochromatic x-ray imager[18] (GMXI), which also uses a KB optic for imaging. The GMXI vacuum housing and KB microscope chassis with the uncoated KB microscope optic were used to obtain framed images on the OMEGA target chamber. Each camera consists of a pair of 25-mm-diam MCP's proximity focused to P-11 phosphor-coated fiber-optic faceplates. Two such cameras record the four images of the KB microscope on Kodak TMAX 3200 film. A frame time of ~80 ps results when the cameras are electrically gated. Each camera can be independently triggered, while the separation of the images (~48 mm) results in a time between images on a camera of ~320 ps. Laboratory tests of the framing camera/KB microscope combination were

performed with the cw x-ray source described above, prior to its use on OMEGA. Figure 74.30(a) shows one such image. The resultant MTF is shown in Fig. 74.30(b) and is compared to the MTF's of the KB microscope without a framing camera and the MTF of a 10-μm pinhole at comparable magnification. As is evident, some amount of spatial resolution is lost when using the framing cameras with the KB microscope. The framing camera allows flexibility, however, in choosing the time of the radiograph when not using a short-pulse backlighter.

The energy dependence of the KB optic reflectivity was measured with the same tungsten x-ray source described above using the method described in Dhez *et al.*[19] The spectrum of both the reflected and unreflected x rays were recorded with a AMPTEK XR-100T Si(Li) detector.[20] The reflectivity was computed from the ratio of the two observed spectra and is shown in Fig. 74.31 along with the reflectivity computed from the tabulated values of the atomic scattering factors[21] and assuming a grazing angle of 0.70°. Both the ideal calculated response and the response convolved with the Si(Li) detector energy resolution are shown. The measurements were taken through a path that contained 38 μm of Be, which limited the sensitivity below 1.5 keV. The difference between the measured and computed reflectivities is small and may be due to

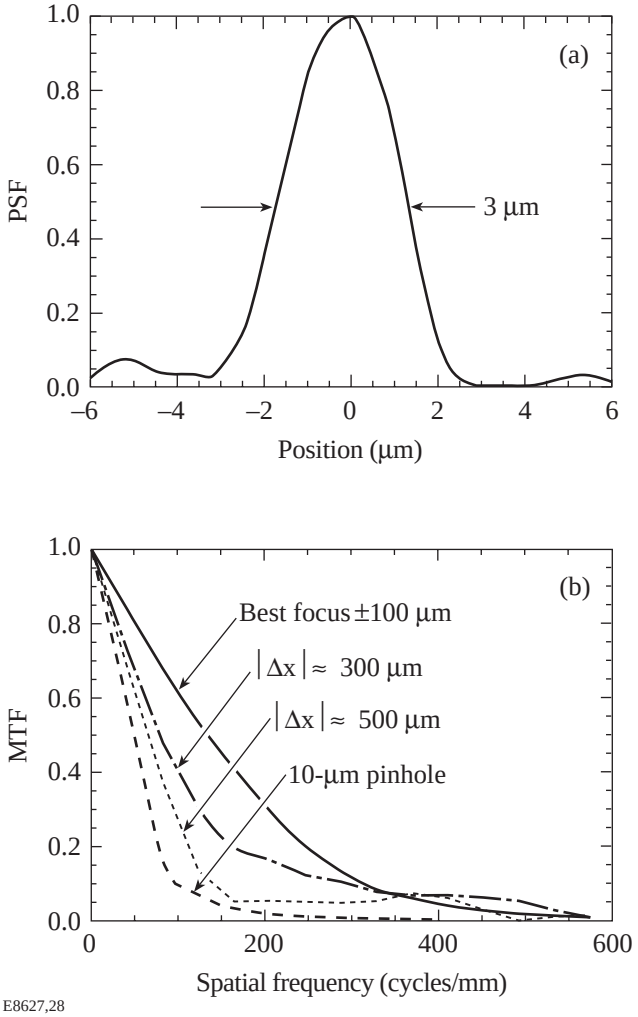

Figure 74.29
The PSF and MTF of the KB microscope recorded with DEF film. (a) The PSF near best focus; (b) the MTF versus position compared to that of a 10-μm pinhole at comparable magnification.

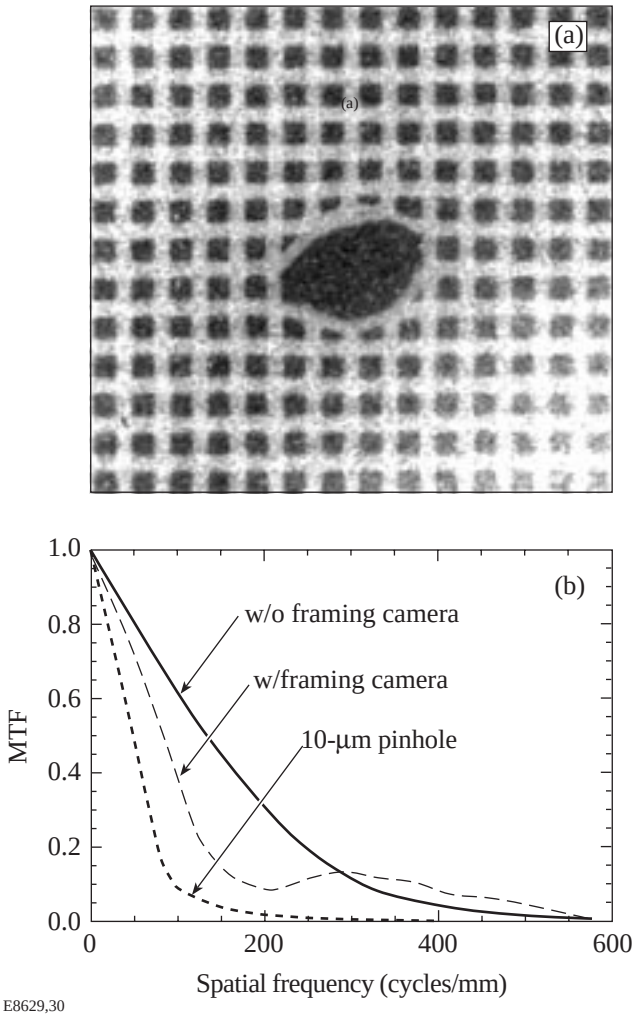

Figure 74.30
Laboratory test of the KB microscope with images recorded by a framing camera. (a) Image of the grid taken with a framing camera and a cw x-ray source; (b) the MTF of the KB microscope with framing camera–recorded images compared to the same obtained without framing cameras. The MTF of a 10-μm-pinhole-camera–based framing camera is also shown for comparison (dotted line).

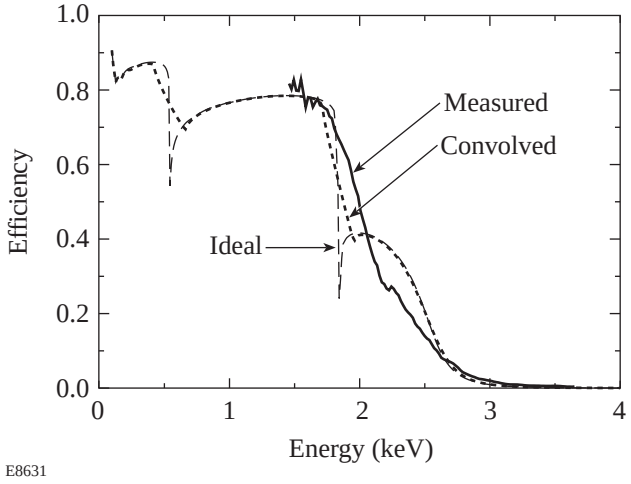

Figure 74.31
The reflectivity of the KB microscope versus energy. The solid line is the measured reflectivity, the dashed line is the reflectivity computed using tabulated values of the atomic scattering constants, and the dotted line includes the convolved response of the Si(Li) detector.

imprecise knowledge of the energy resolution of the Si(Li) detector at the low energies involved. The reflectivity is seen to fall at the Si edge (1.8 keV) and cut off at ~3 keV as expected due to the usual grazing-angle dependence of the x-ray reflectivity.

The choice of uncoated glass as the reflecting surface for planar-foil radiography is further elucidated by the following spectral analysis: A typical backlighter used for these experiments is a uranium foil illuminated at intensities of ~3 × 10^{14} W/cm^2. The spectrum of x rays emitted by such a backlighter[22] is shown in Fig. 74.32(a). Most of the emission comes from the uranium *N*-band (which is unresolved in this measured spectrum) with an additional peak at 3.5 keV due to *M*-band emission. A sensitivity weighted toward the low-energy end of the spectrum (<1.5 keV) is desired since the radiography is to be performed on a plastic (CH) foil. The uncoated-glass optic has a sharp dip in the reflectivity at 1.8 keV followed by a gradual decrease to nearly zero from 2 to 3 keV. The cutoff above 3 keV provides for complete rejection of *M*-band x rays (which would decrease the contrast of the radiography). The response to the U-backlighter spectrum can be further optimized with filtration. Figure 74.32(b) shows the computed efficiency of the KB optic when a 25.4-μm-thick Be plus a 6-μm Al filter is used. Figure 74.32(c) shows the spectral flux density seen at the image plane calculated for 10 J in a 300-μm-diam spot in a 100-ps interval (~1.5 × 10^{14} W/cm^2). This combination of microscope reflectivity and filter transmission is seen to result in a spectrum of x rays in a narrow band from ~1 to ~1.5 keV. The 1/*e* depth of x rays through plastic (such as parylene) in the midpoint of the band (1.25 keV) is ~9 μm. Conversely, a 0.5-μm variation in thickness through the foil would produce a modulation in the x-ray signal of ~5%. The calculated flux density is more than adequate to produce a good exposure on Kodak DEF (as would be the case when using a short-pulse backlighter).

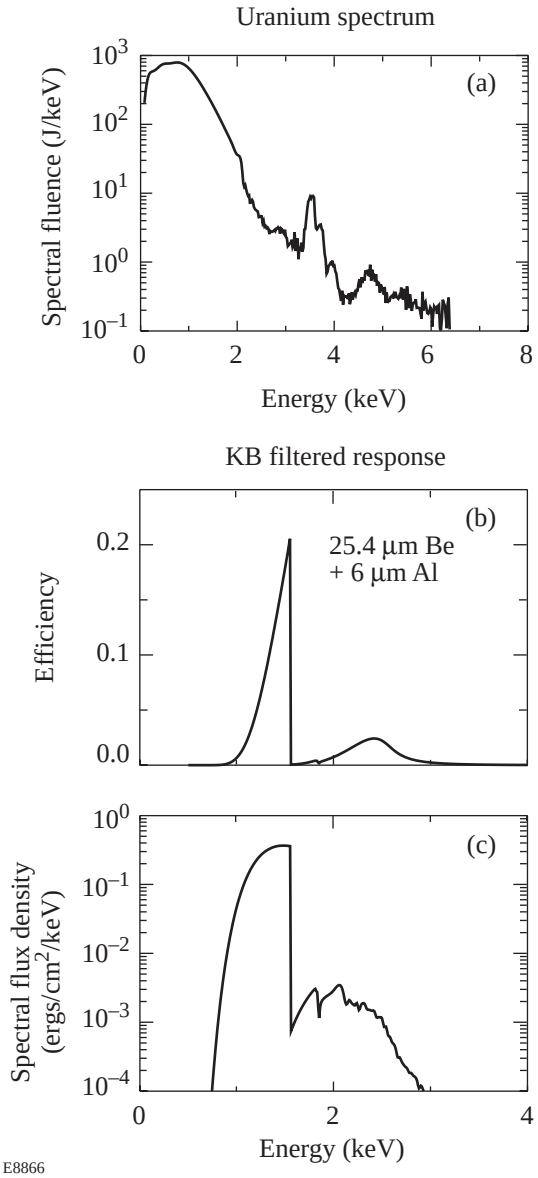

Figure 74.32
The response of the KB microscope to a uranium backlighter. (a) U-backlighter spectrum;[22] (b) the KB microscope response with a 25.4-μm Be plus 6-μm Al filter; (c) spectral flux density at the image plane calculated from the spectrum in (a) and the filter in (b).

Experiments on the OMEGA Laser Facility

Experiments were performed on the OMEGA 60-beam, UV (351-nm) laser system[14] using the soft x-ray KB optic to image laser–plasma x-ray emission. The KB microscope arrangement and the target-illumination method are shown in Fig. 74.33. Targets consisted of test grids and/or driven modulated foils backlit by U foils, illuminated by up to six beams of OMEGA at an intensity of up to 2.5×10^{14} W/cm^2. Figure 74.34 shows a set of such images of backlit grids. [The grids in this case were 25-μm-thick electroetched Ni mesh with a 500/in. pattern (e.g., 50-μm pattern) and 10-μm-square holes.] Grid shots were used to verify the system alignment and provide an *in-situ* measurement of the resolution. Figure 74.34(a) is a DEF-recorded image of a long-pulse (~3-ns) backlit grid, Fig. 74.34(b) is a DEF-recorded image of a short-pulse (~200-ps FWHM Gaussian) backlit grid, and Fig. 74.34(c) is a framing camera–recorded image of a long-pulse backlit grid. Analysis of the images yields MTF's indistinguishable from those shown in Fig. 74.30(b), verifying that the resolution of the microscope is maintained when using a laser–plasma source as a backlighter. Again, spatial resolution of 3 μm is obtained when the radiographs are recorded without the aid of a framing camera.

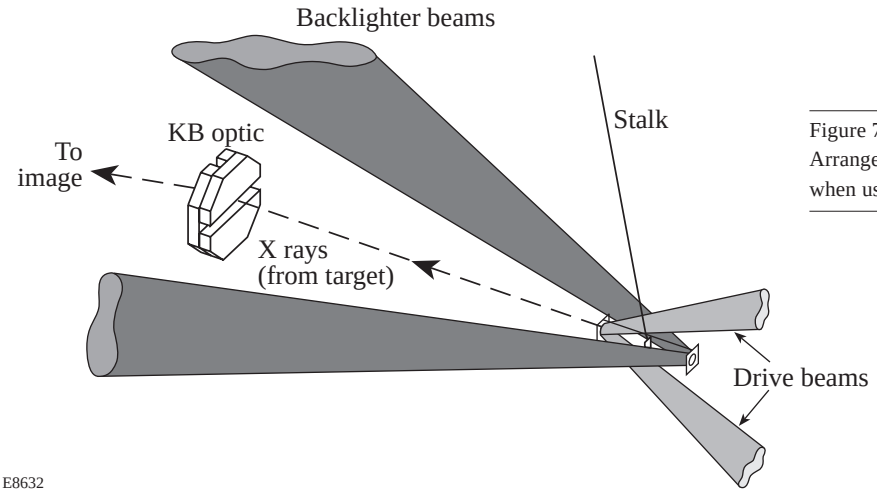

Figure 74.33
Arrangement of KB microscope, target, and beams of OMEGA when used for backlit flat-foil imaging.

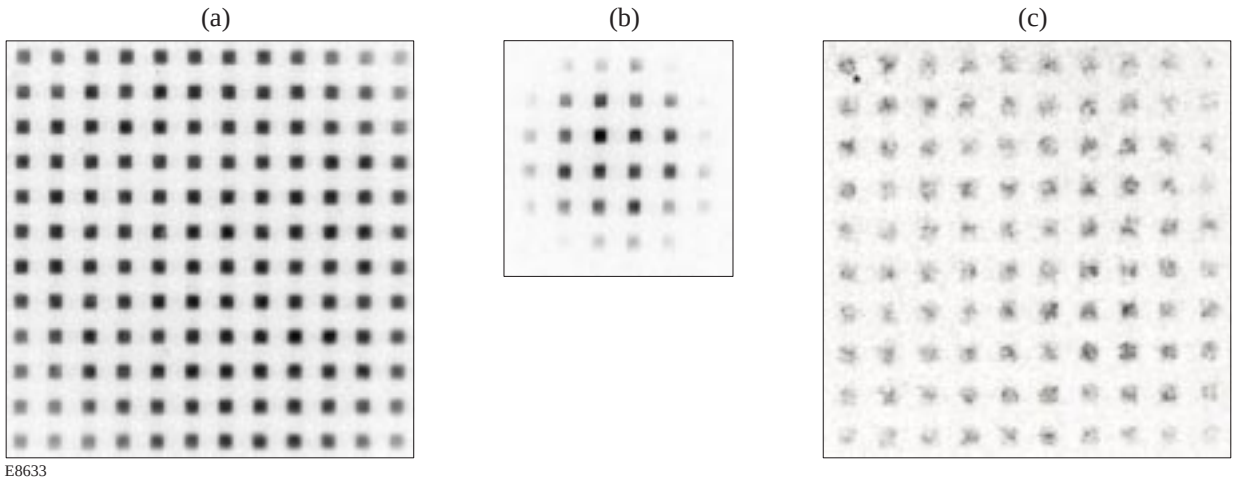

Figure 74.34
Resolution tests performed on the OMEGA laser system. (a) DEF-recorded image of a long-pulse backlit grid; (b) DEF-recorded image of a short-pulse backlit grid; and (c) framing camera–recorded image of a long-pulse backlit grid.

The framing cameras were used to image radiographs of driven perturbed foils. The overall experiments to observe Rayleigh–Taylor (RT) growth are more completely described in Knauer *et al.*[6] Figure 74.35(a) shows a framed image of one such driven foil, which consisted of a 20-μm-thick plastic foil with a 1.0-μm peak-to-valley, 20-μm period modulation on the driven side. The drive intensity was ~2×10^{14} W/cm^2. An intensity-converted lineout taken vertically through the image is shown in Fig. 74.35(b). (The values are deviations from the local average intensity.) An observed variation of ~6% peak-to-valley is evident, which is consistent with early-time (t < 0.5 ns) modulation, assuming the average energy of the x rays producing the modulation is ~1.25 keV. The image shown in Fig. 74.35 serves as an example of the microscope's capabilities.

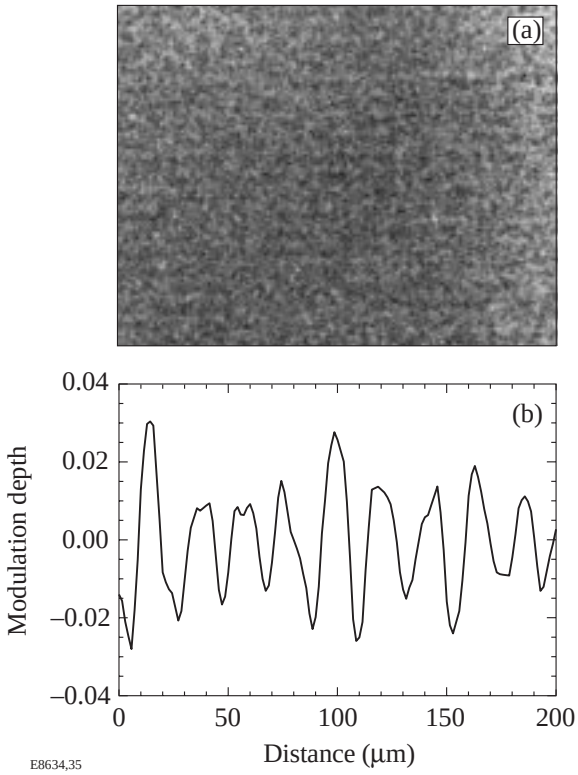

Figure 74.35
Radiograph of driven modulated foil. (a) Framed image of driven foil having an initial modulation depth of 1.0 μm and a 20-μm period; (b) lineout through the image.

Multiple-Beam, Short-Pulse Backlighting

The best possible method for utilizing the high spatial resolution of the KB microscope is to record the radiographs directly with x-ray sensitive film, or with a solid-state device having comparable spatial resolution, as was demonstrated in the preceding section. Since it is necessary to observe the time evolution of the object being radiographed in this instance (i.e., the modulated driven foil), a short-pulse (~100 ps or less) backlighter is required. This can be accomplished on OMEGA with up to six beams, as shown schematically in Fig. 74.36. The short pulses are staggered in time to arrive at the backlighter, spaced by the desired delay, and arranged to backlight the target from separate but nearby directions as seen from the microscope. Since the microscope, as installed in the OMEGA target chamber, is surrounded by six beams, a natural arrangement is for the beams to backlight the driven target in a hexagonal pattern. Tests are currently underway to provide for this experimental configuration on OMEGA.

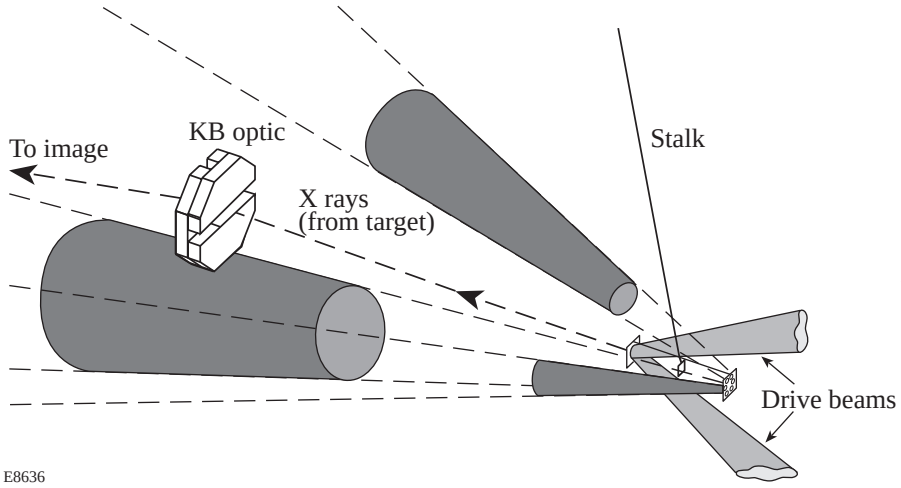

Figure 74.36
Configuration for obtaining multiframe radiographs by multibeam, short-pulse backlighter irradiation.

Conclusions

The KB microscope described in this article has a demonstrated resolution of ~3 μm at optimum focus and a sensitive energy range of ~1 to 3 keV dependent on filtration. When used with a framing camera, the obtainable resolution is degraded to ~7 μm, but with the benefit of ~80-ps time resolution afforded by the cameras. Both high-spatial (~3-μm) and temporal resolution can be obtained by using a multiple-beam, short-pulse backlighter configuration. In conclusion, the KB microscope described here as used in the GMXI is a flexible diagnostic of laser-driven, planar-foil experiments, providing the desired time-resolved, high-spatial-resolution x-ray radiographs.

ACKNOWLEDGMENT

The authors acknowledge the support of the staffs at the Laboratory for Laser Energetics and the Los Alamos National Laborabory. This work was supported by the U.S. Department of Energy Office of Inertial Confinement Fusion under Cooperative Agreement No. DE-FC03-92SF19460, the University of Rochester, and the New York State Energy Research and Development Authority. The support of DOE does not constitute an endorsement by DOE of the views expressed in this article.

REFERENCES

1. J. Grun *et al*., Phys. Rev. Lett. **58**, 2672 (1987).
2. M. Desselberger *et al*., Phys. Rev. Lett. **65**, 2997 (1990).
3. S. G. Glendinning, S. V. Weber, P. Bell, L. B. DaSilva, S. N. Dixit, M. A. Henesian, D. R. Kania, J. D. Kilkenny, H. T. Powell, R. J. Wallace, P. J. Wegner, J. P. Knauer, and C. P. Verdon, Phys. Rev. Lett. **69**, 1201 (1992).
4. K. Shigemori *et al.*, Phys. Rev. Lett. **78**, 250 (1997).
5. S. G. Glendinning, S. N. Dixit, B. A. Hammel, D. H. Kalantar, M. H. Key, J. D. Kilkenny, J. P. Knauer, D. M. Pennington, B. A. Remington, R. J. Wallace, and S. V. Weber, Phys. Rev. Lett. **78**, 3318 (1997).
6. J. P. Knauer, C. P. Verdon, D. D. Meyerhofer, T. R. Boehly, D. K. Bradley, V. A. Smalyuk, D. Ofer, P. W. McKenty, S. G. Glendinning, D. H. Kalantar, R. G. Watt, P. L. Gobby, O. Willi, and R. J. Taylor, in *Laser Interaction and Related Plasma Phenomena*, edited by G. H. Miley and E. M. Campbell (American Institute of Physics, Woodbury, NY, 1997), Vol. 406, pp. 284–293.
7. C. Brown *et al.*, Phys. Plasmas **4**, 1397 (1997).
8. S. G. Glendinning *et al.*, Rev. Sci. Instrum. **63**, 5108 (1992).
9. H. F. Robey, K. S. Budil, and B. A. Remington, Rev. Sci. Instrum. **68**, 792 (1997).
10. B. A. Remington *et al.*, Rev. Sci. Instrum. **63**, 5080 (1992).
11. R. Kodama *et al.*, Opt. Lett. **21**, 1321 (1996).
12. F. J. Marshall and Q. Su, Rev. Sci. Instrum. **66**, 725 (1995).
13. J. A. Oertel, T. Archuleta, C. G. Peterson, and F. J. Marshall, Rev. Sci. Instrum. **68**, 789 (1997).
14. T. R. Boehly, D. L. Brown, R. S. Craxton, R. L. Keck, J. P. Knauer, J. H. Kelly, T. J. Kessler, S. A. Kumpan, S. J. Loucks, S. A. Letzring, F. J. Marshall, R. L. McCrory, S. F. B. Morse, W. Seka, J. M. Soures, and C. P. Verdon, Opt. Commun. **133**, 495 (1997).
15. Sydor Optics, Inc., Rochester, NY.
16. P. Kirkpatrick and A. V. Baez, J. Opt. Soc. Am. **38**, 766 (1948).
17. B. L. Henke *et al.*, J. Opt. Soc. Am. B **3**, 1540 (1986).
18. F. J. Marshall and J. A. Oertel, Rev. Sci. Instrum. **68**, 735 (1997).
19. P. Dhez, H. Duval, and J. C. Malaurent, J. X-Ray Sci. Technol. **3**, 176 (1992).
20. A. C. Huber, J. A. Pantazis, and V. T. Jordanov, Nucl. Instrum. Methods Phys. Res. B **99**, 665 (1995).
21. B. L. Henke, E. M. Gullikson, and J. C. Davis, At. Data Nucl. Data Tables **54**, 181 (1993).
22. S. G. Glendinning *et al*., in *Applications of Laser Plasma Radiation II*, edited by M. C. Richardson and G. A. Kyrala (SPIE, Bellingham, WA, 1995), Vol. 2523, pp. 29–39.

Measurements of Core and Pusher Conditions in Surrogate Capsule Implosions on the OMEGA Laser System

The primary objective of the experimental program at LLE is to evaluate the direct-drive approach to laser-driven inertial confinement fusion (ICF). In particular, its central goal is to validate, by using the 30-kJ, 351-nm, 60-beam OMEGA laser system,[1] the performance of high-gain, direct-drive target designs planned for use on the National Ignition Facility (NIF). This will be achieved by diagnosing the implosion of cryogenic, solid-DT-shell capsules that are hydrodynamically equivalent to the ignition/high-gain capsules planned for use on the NIF with a 1- to 2-MJ drive. In the direct-drive approach to fusion, the capsule is directly irradiated by a large number of symmetrically arranged laser beams, as opposed to the indirect approach in which the driver energy is first converted into x rays, which then drive the capsule. Direct drive has the potential to be more efficient since it does not require this intermediate x-ray conversion step. In both cases the high densities and core temperatures necessary for ignition require that the capsules must be imploded with minimal departures from one-dimensional behavior. For direct-drive capsules, the dominant effect contributing to degradations in capsule performance is believed to be the development of Rayleigh–Taylor (RT) unstable growth,[2] seeded by either laser-irradiation nonuniformities or capsule imperfections.

In a direct-drive capsule implosion, the development of hydrodynamic instabilities occurs in a number of stages. In the start-up, or imprinting, phase the laser is directly incident on the solid capsule surface. Eventually, a plasma is created due to either dielectric breakdown or other processes, a critical surface is formed, and the absorption of laser light sends a series of shocks into the target, eventually causing the shell to move and begin to accelerate. During this initial phase, nonuniformities present in the laser will cause nonuniform shocks to be launched into the target, resulting in imposed modulations and a certain amount of unstable growth during the shock transit period due to Richtmyer–Meshkov[3] (shock-driven) or RT (acceleration-driven) instability. During the subsequent acceleration phase of the implosion, RT growth continues to grow at the ablation surface with a growth rate that can be approximated by[4,5]

$$\gamma = \alpha\sqrt{[kg(t)]} - \beta kV_a(t), \tag{1}$$

where k is the unstable wave number, $g(t)$ is the acceleration, and $V_a(t)$ is the ablation velocity. The distortions that grow at the ablation surface can eventually feed through to the inner surface of the shell, where they add to any existing mass perturbations, thus seeding an instability that can grow at that surface as the target begins to decelerate during stagnation. If the resultant distortions are large enough, the performance of the capsule will be severely compromised. An integrated understanding of hydrodynamic instabilities, fuel–pusher mix, and their effect on capsule performance requires quantitative data and a study of the processes involved in each phase.

In this article we present the results of direct-drive experiments carried out on OMEGA to investigate each of the stages described above. First, we summarize the results of experiments designed to study the imprint and acceleration stages, in both planar and spherical geometries. Next we present the first phase of the investigation of the deceleration stage. [This stage has previously been investigated in indirectly driven targets at the Lawrence Livermore National Laboratory (LLNL) using plastic targets with an inner layer of Ti-doped CH and an Ar-doped D_2 fill.[6–8]] The goal of our initial experiments was to ensure that our diagnostics could measure the conditions in both the core and the shell during shell deceleration and stagnation and that they had enough sensitivity to observe differences in core conditions under various RT-growth conditions. The RT growth was modified by varying the temporal pulse shape (Gaussian or square) and by doping the outer 6 μm of the CH shell with chlorine.

The deceleration stage was studied by irradiating ~1-mm-diam, 20-μm-thick CH shells with 30 kJ of 351-nm, 1-ns laser pulses. No smoothing techniques were applied to the laser beams. The one-dimensional simulations of the experiments were carried out with the hydrodynamic code *LILAC*,[9] which includes ray tracing of the laser light, SESAME[10] equations of state, multigroup radiation transport, and non-LTE average-

ion capability. A few simulations were carried out with the two-dimensional code *ORCHID*[11] to investigate qualitatively the effect of the RT growth on the target during the acceleration, deceleration, and stagnation of the shell.

Imprint and Acceleration Phases

Direct measurements of laser imprinting are extremely difficult, although Kalantar *et al.*[12] have reported measurements of imprint in thin Si and Al foils using an x-ray laser as a backlighter. Measurements on OMEGA to date have relied on the technique of x-ray radiography of laser-accelerated CH foils in planar geometry,[13–17] using a uranium backlighter with an average photon energy of ~1.3 keV. Modulations in the optical depth of the driven foil measured at different times by an x-ray framing camera are used to observe the growth of perturbations seeded by imprinting. However, since the initial perturbations created by the laser imprint are too small to be measured directly by this method, the optical-depth measurements are not taken until the foil has accelerated and undergone a significant amount of RT growth in order to amplify the initial perturbation to detectable levels. This measurement therefore incorporates the combined effects of the imprint phase, shock transit phase, and a portion of the acceleration phase. Despite the complication added by the RT growth, such measurements are invaluable for comparing the effects of irradiation-uniformity changes, beam-smoothing techniques, and other mitigation schemes.

Face-on radiography of foils with intentionally imposed single-mode, sinusoidal mass perturbations were used to compare calculated RT-growth rates with experimental measurements. (These experiments are a continuation of the collaboration between LLE and LLNL.[14] Similar experiments have also been performed in indirect drive.[18]) In these measurements an x-ray streak camera or framing camera is used to measure the optical depth of the imposed mode as a function of time in much the same way as in the imprint measurements. In addition, side-on measurements of foil trajectory were used[19] to confirm that coupling of laser energy into the foils was in agreement with simulations. Results from single-mode experiments carried out on OMEGA are shown in Fig. 74.37. In these plots, the optical depth of the observed modulation of the backlighter, as seen through the accelerated foil, is plotted as a function of time, together with predictions from the 2-D hydrodynamic code *ORCHID*. (A more detailed description of this data can be found in Ref. 19.) The excellent agreement between the experimental data and the simulations is strong evidence that, for polymer materials, the RT unstable growth can be calculated accurately.

In spherical target experiments, where there is no diagnostic access to the rear surface of the shell, we have inferred the development of instability growth at the ablation surface during the acceleration phase through use of the so-called "burnthrough" technique.[20] In this method, time-resolved

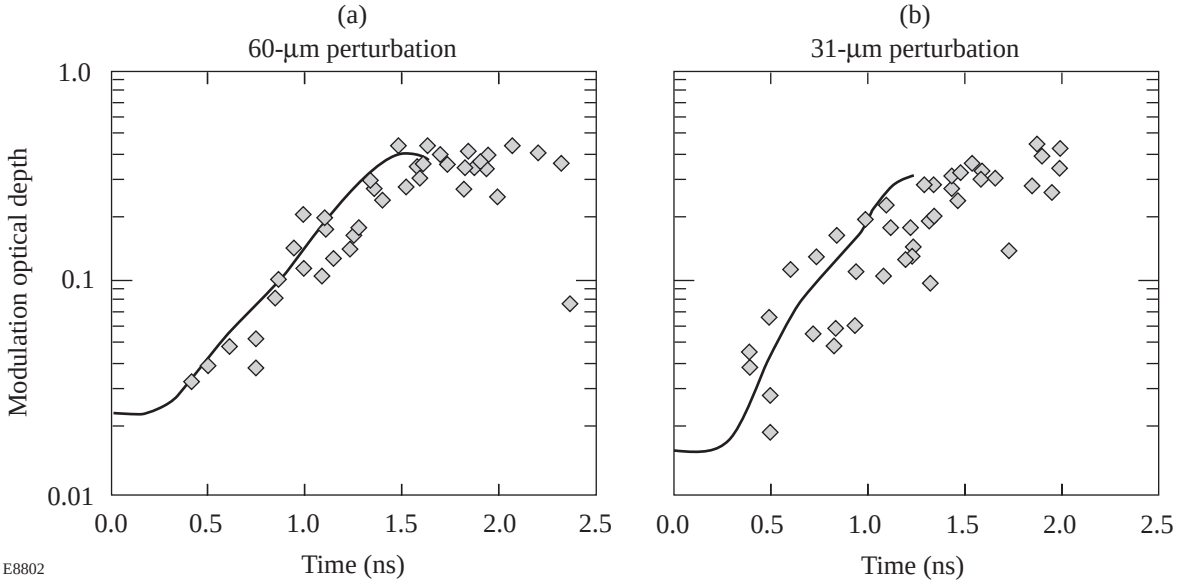

Figure 74.37
Results from the single-mode planar experiments (◆) conducted on the OMEGA laser compared to *ORCHID* simulations (solid line) for (a) 60-μm and (b) 31-μm perturbation wavelengths.

spectroscopy, using a spectrally dispersing x-ray streak camera, is used to detect the onset of x-ray emission from a buried signature layer. In the absence of any unstable growth or perturbation, the heat front propagates uniformly through the CH ablator until it reaches the signature layer and heats it, resulting in characteristic x-ray line emission. The presence of unstable growth, however, produces a mix region that can leach signature layer material out to the heat front, causing early emission. This method has been shown to be very sensitive to initial beam uniformity[21] and to target acceleration and effective Atwood number.[20] As with the planar-foil imprint measurements, this method measures the combined effects of imprint coupled with RT growth.

We conducted a series of burnthrough experiments with unsmoothed laser beams to provide a baseline for subsequent uniformity improvements scheduled for the OMEGA laser system. The targets used chlorinated plastic (C_8H_7Cl) as the signature layer, with CH ablator overcoats ranging from 8 to 12 μm. The target diameters were 900 to 950 μm, and in all cases the total shell thickness was 20 μm. The capsules were overcoated with a 1000-Å Al barrier layer to act as a timing reference mark and to prevent shinethrough[22] of the early part of the laser pulse into the target before formation of the critical surface. In these experiments, the targets were imploded by 60 beams, focused tangentially to the target, with a 1-ns full-width-at-half-maximum (FWHM) Gaussian temporal profile and a total of 20 to 25 kJ. Spectral dispersion for the x-ray streak camera was provided by a flat rubidium acid phthalate (RbAP) crystal, providing coverage of the *K*-shell spectrum of the Al overcoat in first-order Bragg diffraction, simultaneous with coverage of chlorine lines in second order. The data from these experiments, together with a typical streak camera image, are shown in Fig. 74.38(a). The time-resolved spectrum [Fig. 74.38(a)] shows Al lines, formed when the laser is initially incident on the outside of the capsule, and, after a delay of several hundred picoseconds, emission from the buried C_8H_7Cl layer. The measurements have been modeled using a postprocessor to *LILAC* that calculates the mix thickness using the Haan[23] method from an experimentally measured initial perturbation spectrum. (Full details of the model are given in Ref. 20.) Figure 74.38(b) shows a comparison of the experimental burnthrough times and those predicted by the model, as a function of CH ablator thickness. The two cases were normalized for one of the 9-μm cases. Variations in burnthrough time for a given ablator thickness are caused primarily by laser energy variations between shots. The burnthrough times predicted by *LILAC* for the uniform 1-D case are also shown and

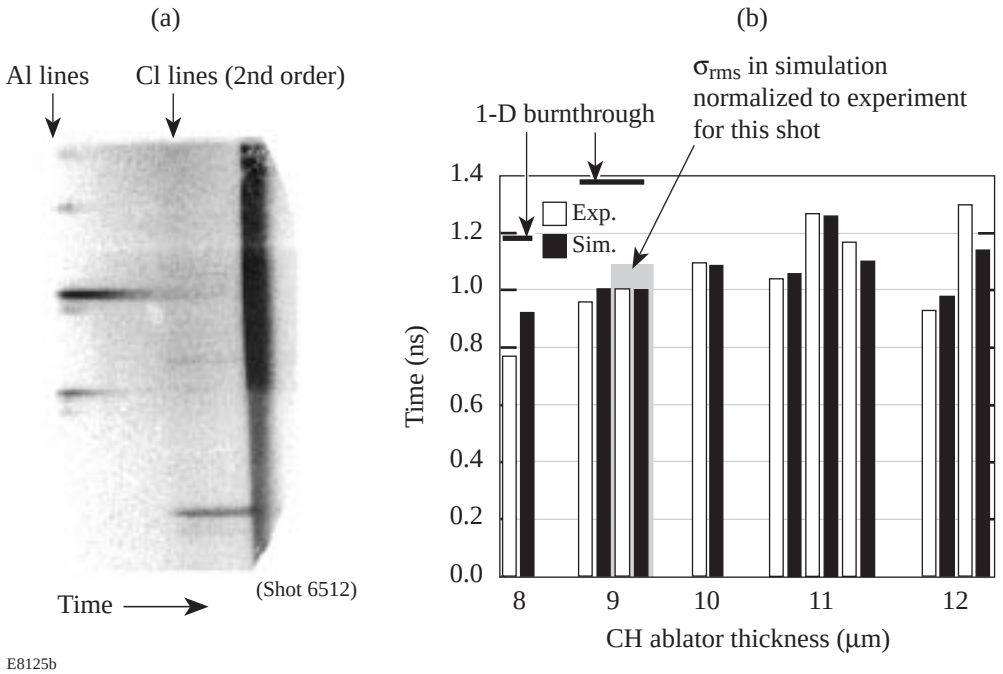

Figure 74.38
Results from burnthrough experiments carried out on the 60-beam OMEGA laser. (a) The streak camera spectrum shows the onset of the Cl lines from the Cl-doped substrate at the time of burnthrough. (b) Burnthrough times from the mix postprocessor to *LILAC* are compared to the experimental data for targets with increasing ablator thickness.

indicate that much-later-than-observed burnthrough would be expected for the 8- and 9-μm ablators, with no burnthrough expected for the thicker cases. The good agreement between the simulations and the experiment over a range of target parameters confirms our confidence in the model and shows that we are now well placed to diagnose planned improvements to laser uniformity.

Deceleration Phase

Initial measurements on deceleration-phase instability utilized a series of surrogate capsules, consisting of a CH shell filled with deuterium gas. These targets are designed to mimic the behavior of future OMEGA cryogenic DT capsules (and, by extension, NIF ignition capsules) by approximating their gross hydrodynamic behavior (e.g., similar in-flight aspect ratio and convergence). For the purposes of these experiments, the CH shell represents the main-fuel-layer region in a cryogenic ignition target, and the D_2 gas represents the fuel hot spot. Figure 74.39 shows the standard capsule we have used to investigate these two regions. The hot spot, or in our case the gas region, consists of 20 atm of D_2, doped with 0.25% Ar as a spectroscopic signature. The shell consists of a 20-μm CH layer in which is buried a 1-μm layer of (1%–4%) Ti-doped CH. The doped layer can be positioned at various distances from the shell/D_2 interface, allowing the study of conditions at different positions inside the shell/main fuel layer. This differs from the method described in Ref. 6, in which the Ti-doped layer was situated only at the pusher/fuel interface.

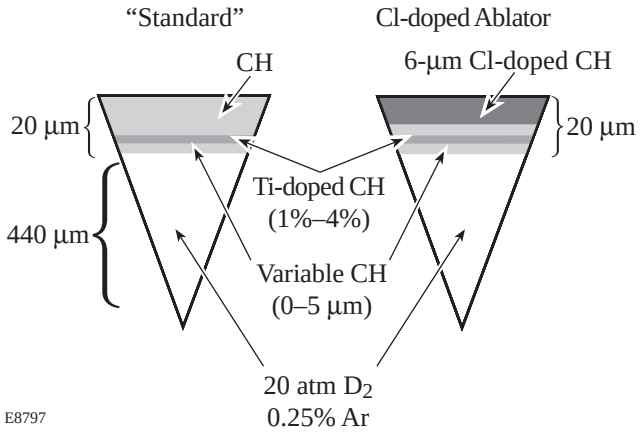

Figure 74.39
"Standard" and Cl-doped-ablator targets used during the deceleration phase experiments. The distance from the Ti-doped layer and the inner surface of the shell can be varied from 0 to 6 μm.

For future experiments the single-beam uniformity on the OMEGA laser system will be improved such that the on-target irradiation uniformity will be <1% σ_{rms}. This will be achieved through the use of distributed phase plates (DPP's),[24] 2-D smoothing by spectral dispersion (2-D SSD),[25] and distributed polarization rotators (DPR's).[26] However, current uniformity levels using unsmoothed beams are predicted to be in the region of 20% or more. To predict the effect these nonuniformities might have on capsule implosions, simulations were performed using the 2-D hydrodynamic code *ORCHID*. The simulations used the actual laser-beam nonuniformity spectrum, measured from single-beam, equivalent-target-plane (ETP) images mapped onto a sphere with the appropriate overlap parameters. Even modes 2 to 200 were consistent with each mode multiplied by $\sqrt{2}$ to account for the odd modes. Figure 74.40 shows predicted mass-density profiles at a time when the shell has reached half its initial radius for two cases: a 1-ns square pulse and a 1-ns FWHM Gaussian. In each case the shell is already showing signs of severe disruption, with the structure in the Gaussian case exhibiting longer-wavelength structures. For both cases the outside of the shell is more perturbed than the inside. As a check on the *ORCHID* predictions, we carried out a number of planar-target radiography experiments, using unmodulated foils of similar thickness (20 μm) and driven with similar intensities to the spherical targets. Figure 74.41 shows radiographs recorded on the x-ray framing camera for both the 1-ns square pulse and the 1-ns Gaussian, together with the predicted foil trajectories in each case. The radiographs show qualitative agreement with the *ORCHID* simulations in Fig. 74.40, both in terms of the type of structure seen and the fact that the Gaussian pulse shows longer-wavelength structure. Note that the Gaussian case is significantly more nonuniform despite having undergone less displacement. This is primarily due to the fact that the Gaussian pulse is predicted to imprint a factor of about 2.5 larger than the square pulse. The growth rates in the two cases are similar since the higher acceleration resulting from the square pulse is compensated by a higher ablation velocity. For an imploding target the growth factor will be larger for a Gaussian pulse because the shell will take longer to reach the same radial position.

Clearly implosions driven by these levels of nonuniformity are expected to be severely disrupted. For comparison purposes only, we investigated a series of targets in which the outer 6 to 7 μm of the ablator was replaced with C_8H_7Cl. The presence of chlorine in the ablator serves to radiatively heat the shell, causing it to decompress. The resultant reduction in peak shell density causes an increase in the ablation velocity V_a, thereby reducing the RT growth [see Eq. (1)]. (It should,

however, be pointed out that the radiation preheat in such a target does reduce the convergence ratio and 1-D performance of the implosion.) Figure 74.42 shows the *ORCHID* simulation for a target with a Cl-doped ablator. Comparison with Fig. 74.40 shows a clear improvement in the shell uniformity. This improvement is also in agreement with experimental measurements detailed in Ref. 20, in which delayed burnthrough times were observed for targets with Cl-doped ablators. *ORCHID* simulations near the time of peak compression are shown in Fig. 74.43. The undoped shell in Fig. 74.43(a) shows that although the core region appears to form relatively uniformly, the shell is clearly severely disrupted. In contrast, Fig. 74.43(b) shows a shell that is still relatively intact, although still not entirely uniform.

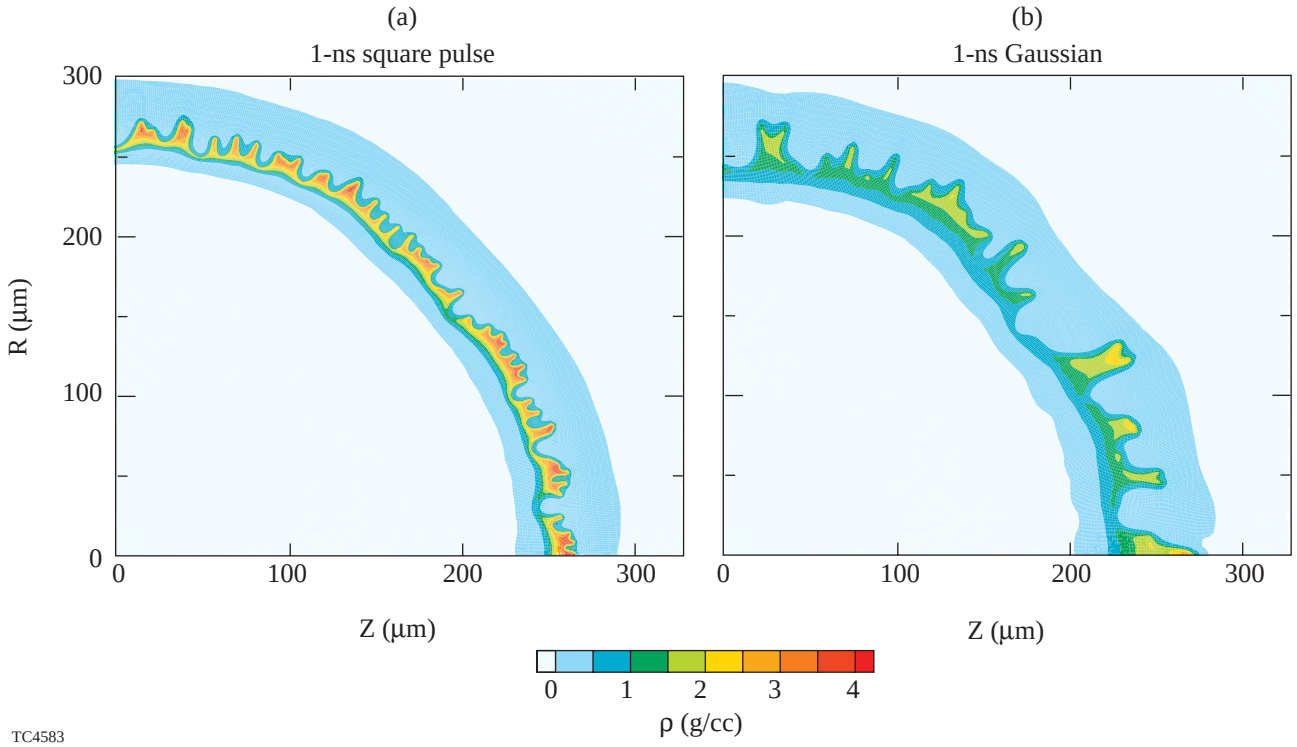

Figure 74.40
Shell conditions from *ORCHID* simulations compared for (a) a 1-ns square pulse and (b) a 1-ns Gaussian pulse irradiating the standard target. The actual laser beam nonuniformity measured from ETP images was used. The contours are for the mass density.

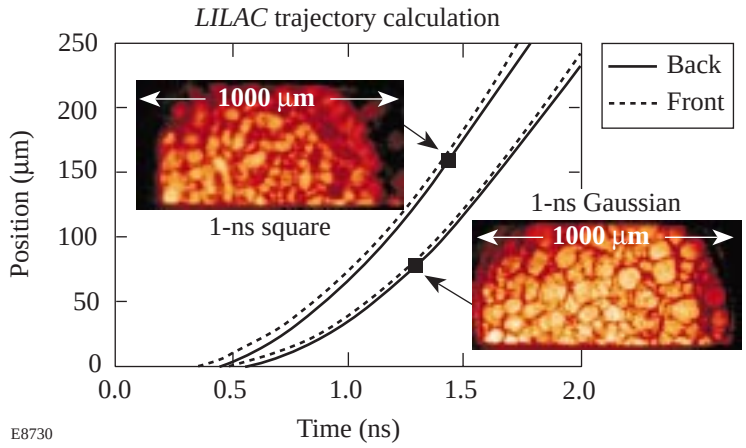

Figure 74.41
Backlit images from an experiment in which five unsmoothed OMEGA beams were focused on a planar 20-μm CH target confirm qualitatively the *ORCHID* simulation results in Fig. 74.40. The zero time for the Gaussian pulse is at 10% of peak intensity.

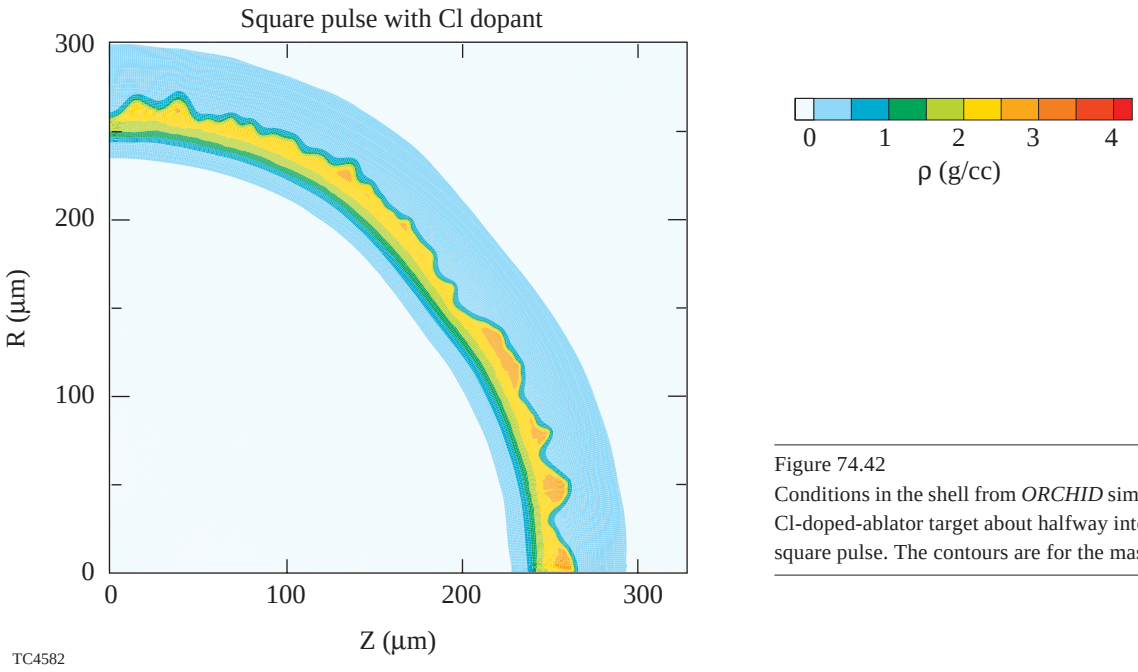

Figure 74.42
Conditions in the shell from *ORCHID* simulations compared for the Cl-doped-ablator target about halfway into the implosion for a 1-ns square pulse. The contours are for the mass density.

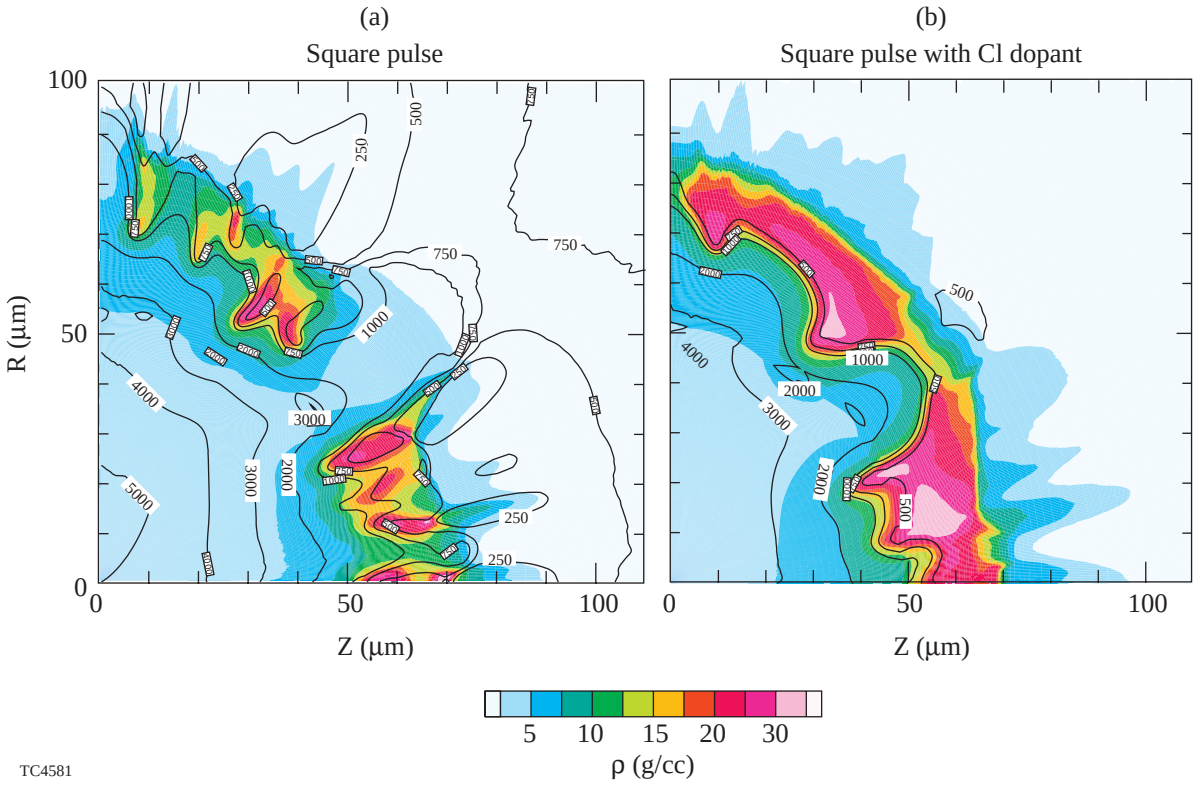

Figure 74.43
Core conditions from *ORCHID* simulations compared for (a) the standard target and (b) the Cl-doped target near time of peak core density for a 1-ns square pulse. The filled contour areas denote the mass density levels and the contour lines denote the electron temperature levels.

The experimental implosions were analyzed using a large number of diagnostics. Time-resolved imaging of the later stages of the shell trajectory and the core formation was recorded using a gated x-ray pinhole camera,[27,28] filtered to record emission >2 keV. Figure 74.44 shows a comparison of the measured shell and core radii as a function of time, compared with 1-D *LILAC* simulations. This comparison demonstrates our ability to reproduce the zeroth-order hydrodynamics of the implosion. Time-resolved x-ray spectra from the targets were recorded using a pair of streaked spectrographs. Both instruments used a RbAP crystal to disperse the spectrum onto a 250-Å Au photocathode. One spectrometer was set up with a wavelength range of ~2.8 to 4.3 Å to cover the Ar *K*-shell emission from the core, with the other spectrometer covering Ti and Ar emission in the approximate range of 1.9 Å to 3.4 Å. In each case the spectral resolution was approximately $E/\Delta E \sim 500$. Temporal resolution was 20 to 30 ps, depending on the camera used. The data were recorded on Kodak T-max 3200 film, digitized using a PDS microdensitometer and then corrected for film sensitivity and streak-camera–induced temporal curvature.[29] The sweep speed of each streak camera was measured using a temporally modulated fiducial pulse, although no absolute timing reference was used during actual target shots. The spectrometer dispersion was calculated using published wavelengths for the Ar and Ti lines.

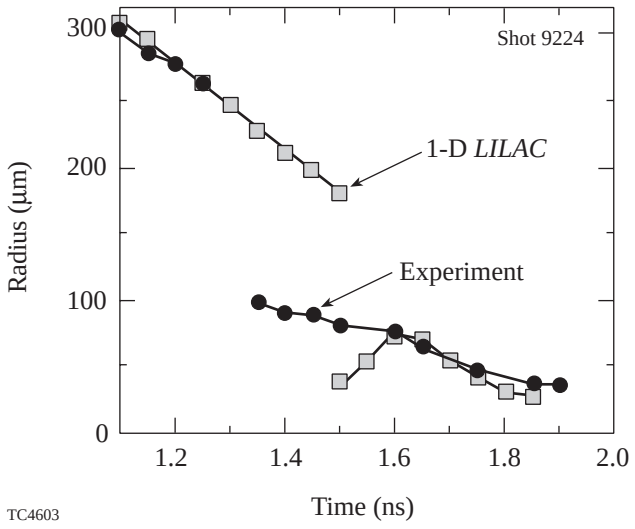

Figure 74.44
Trajectories of the peak emission from the framing camera images and from simulated images. The jump in the middle of the trajectories occurs when the peak emission moves from the heat front to the core.

Figure 74.45 shows a pair of time-resolved x-ray spectra recorded from the doped target implosions, one from a target with the Ti-doped layer at the gas/shell interface and the other with the Ti-doped layer situated 4 μm from the interface. In both streaks, Ar line emission, resulting from the initial shock heating of the core gas, appears first, followed by continuum emission from the stagnation. In Fig. 74.45(a), Ti He-like and H-like line emission from the inside surface of the shell can be seen a short time after the Ar emission, whereas the Ti in the buried layer is observed only in absorption. This absence of line emission occurred even when the Ti-doped layer was as close as 0.5 μm from the interface. Targets with a Cl-doped ablator showed little or no Ti emission, regardless of the position of the layer, in agreement with *LILAC* predictions.

The absorption feature seen in Fig. 74.45(b) around 4.6 keV corresponds to unresolved transitions of the type 1*s*–2*p* in titanium ions with incomplete *L* shells: Ti^{+13} to Ti^{+20}, formed when continuum from the core traverses the cold titanium layer. The envelope of the absorption feature, which changes as a function of time, indicates the ion specie of maximum abundance. The amount of absorption depends primarily on the areal density of the absorption region, but also on its temperature T and density ρ. It has been shown, however, that the measured integral over the absorption feature, together with the knowledge of the ion of peak absorption (which also depends on both T and ρ) can yield the areal density to within ±25% without knowing the temperature or the density.[30,31] Typical data is plotted in Fig. 74.46, together with the $\rho\Delta R$ predicted by *LILAC* for both a CH and a Cl-doped ablator. The measured areal density for the "standard" capsule case approximately follows the continuum emission and falls well below the *LILAC* prediction. This is not entirely surprising, based on the shell disruptions seen in Fig. 74.43(a). It is also possible that for such a severely distorted shell, low-density "holes" in the shell will cause the inferred areal density to be underestimated because the unabsorbed background signal distorts the spectrum. In contrast, the $\rho\Delta R$ measurements in Fig. 74.46(b) approach more closely to the 1-D simulations. In this shot, the timing of the density peak, delayed relative to the continuum emission, shows one of the limitations to this method since in the absence of any continuum emission we are unable to measure the $\rho\Delta R$ by absorption methods.

Measurements of the core/hot-spot region were carried out using both neutron-based and x-ray spectroscopic measurements. The burn history of these capsules was measured using the neutron temporal diagnostic (NTD).[32,33] Neutron collisions with a BC-422 plastic scintillator convert neutron kinetic

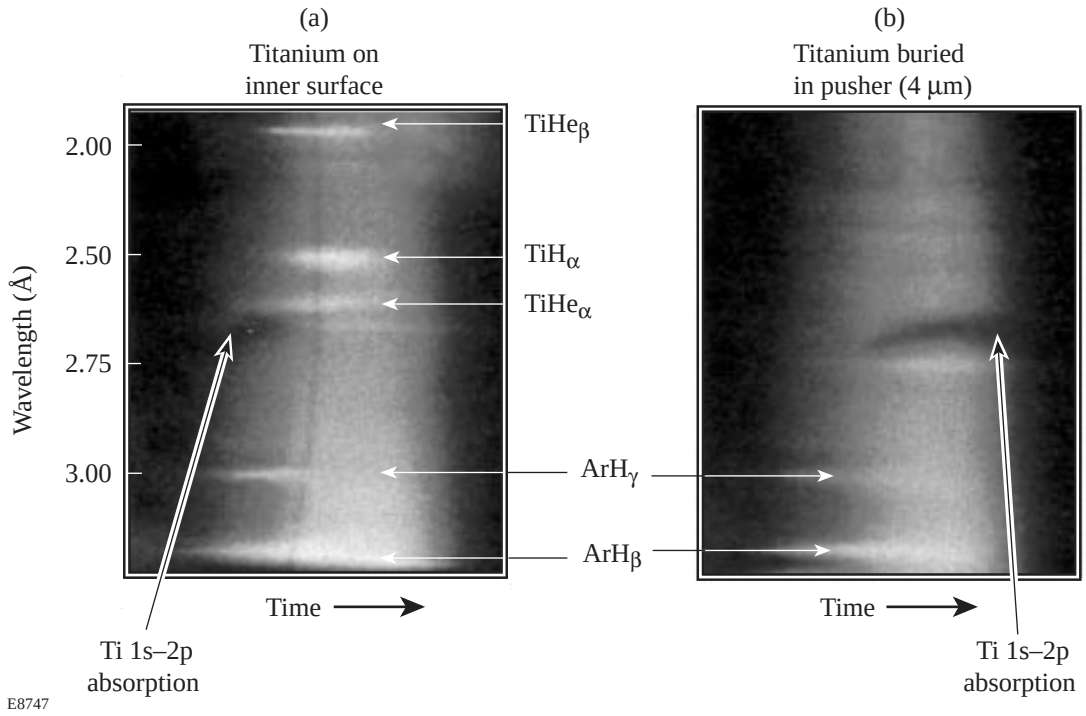

Figure 74.45
Time-resolved spectra for two positions of the Ti-doped layer for a standard target and a 1-ns square pulse: (a) at the inner surface and (b) 4 μm from the inner surface.

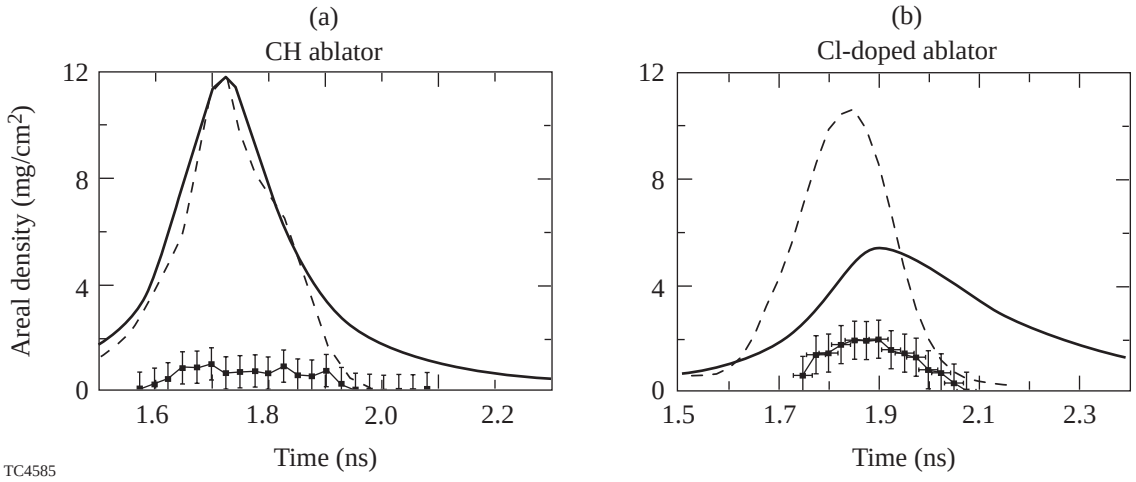

Figure 74.46
Areal densities obtained from the Ti absorption band (curve with error bars) and from the 1-D *LILAC* simulation (solid line) as a function of time for (a) the standard target and (b) the Cl-doped-ablator target. In both cases the Ti-doped layer was 4 μm from the inner surface. Also shown is the integrated continuum emission (dashed line) from the measured spectrum. Timing was made by matching the measured and predicted continuum peaks. The areal density can be measured only when the core emits continuum radiation.

energy to 350- to 450-nm-wavelength light, which is relayed to the photocathode of a fast streak camera whose output image is recorded by a charge-coupled device (CCD) camera. The temporal distribution of the emitted light is the convolution of the neutron emission history with the scintillator response; thus, the burn history is encoded in the leading edge of the light pulse. (The streak camera also records an optical fiducial signal to provide an absolute time base.) The shape of the neutron temporal distribution is obtained by deconvolving the effect of the scintillator decay rate from the recorded neutron signal. The quality of each deconvolution is checked by comparing the recorded signal with the convolution of the burn history and the exponential decay of the scintillator. Streak camera flat-field and time-base corrections are included in the signal processing. On OMEGA, NTD has demonstrated sensitivity to DD neutrons at yields above 1×10^8 and a temporal resolution of 25 ps. Figure 74.47(a) shows the measured neutron-production rate for a shot with a CH ablator, together with the rate predicted by *LILAC*. The rates agree fairly well early in time, when neutron production is dominated by the initial shock heating and compression, but as the implosion progresses toward full stagnation, where neutrons will be produced mainly by compression heating of the core, the measured rate falls significantly short of the 1-D predictions by a factor of about 20 to 30. We are, however, able to see a significant difference for implosions with the Cl-doped ablator [Fig. 74.47(b)]. In this case the predicted yield is lower due to radiative losses and preheating of the core. The measured neutron-production rates, however, come much closer to the simulations (a factor of 4 to 5 at peak production), although the experimental yield still cuts off earlier than the simulations.

Additional measurements of conditions inside the core were carried out by spectroscopic analysis of the *K*-shell line emission from the argon dopant.[34,35] For temperature and density regimes typically found in these implosions close to stagnation, the line shapes emitted by the *K*-shell argon ions depend strongly on electron density, while remaining relatively insensitive to changes in temperature. This fact combined with the temperature and density dependence of the relative intensity of the *K*-shell lines and their associated *L*-shell satellites allows the use of the argon line spectrum as an indicator of electron density and temperature. The effects of opacity broadening on the utility of this diagnostic are mitigated by the small concentration of argon in the fuel.

Stark-broadened line profiles for the argon He-γ, He-δ, and Ly-β resonant transitions and associated Li-like satellites were calculated using a second-order quantum mechanical relaxation theory.[36,37] These line profiles were combined using relative intensities derived from a detailed non-LTE kinetics code[38] corrected for the effects of radiative transfer using an escape-factor approximation.[39] The final state populations of the lines in the model were also derived from the results of the kinetics code. Source size was derived by assuming the emission was that of a homogeneous spherical region whose size was determined consistently with the electron number density. The Stark-broadened line profiles were cor-

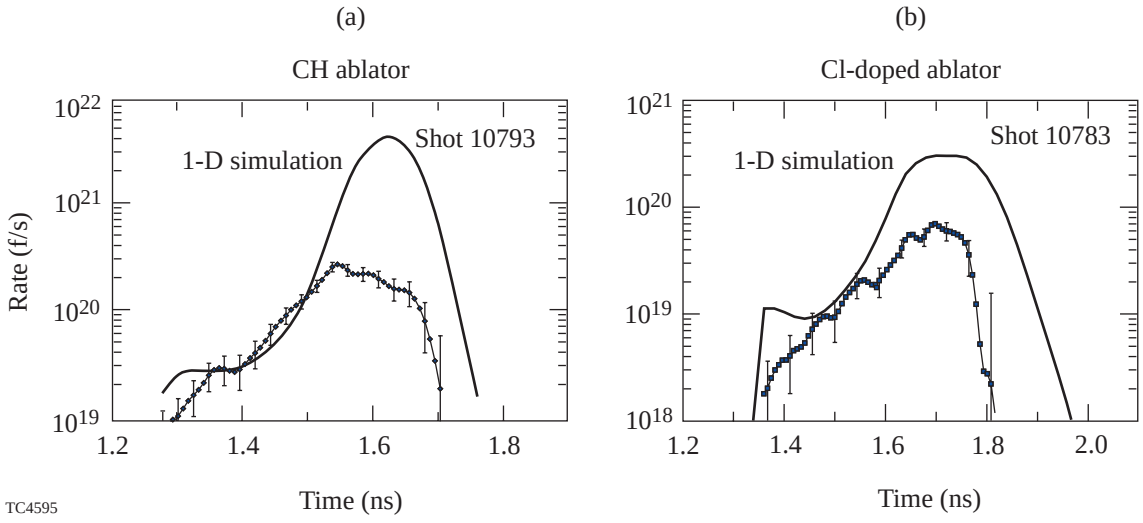

Figure 74.47
Neutron production rate obtained from the neutron temporal diagnostics (NTD) (curve with error bars) and from 1-D *LILAC* simulations (solid line) for (a) the standard target and (b) the Cl-doped-ablator target.

rected for the effects of opacity using a slab opacity model.[40] A similar theoretical spectrum was used in the analysis of the argon He-β line and its associated lithium-like satellites in Ref. 35. An example of the fits for shot 10778 is shown in Fig. 74.48. Comparison of the theoretical spectrum, after convolution with an appropriate instrumental response function, with time-resolved experimental spectra leads to an inference of the emissivity-averaged plasma electron temperature and density. Differences between the best-fitting theoretical spectrum and the experimental spectrum indicate the possible existence of gradients in the strongly emitting region of the plasma.

Figure 74.49 shows inferred electron temperature and density measurements as a function of time for the CH ablator target, imploded with the 1-ns square pulse. The temperatures and densities agree fairly well with the 1-D *LILAC* predictions at early times, but as the stagnation progresses, both parameters fall well short of the ideal case. These results are in qualitative agreement with the fusion-rate measurements. For the Cl-doped ablator (Fig. 74.50), the agreement between experiment and 1-D simulation is much closer, although the temperature still reaches only 75% of predicted.

Discussion and Conclusion

We have presented results that are part of an integrated program to investigate the physics of direct-drive ICF capsule implosions. Imprint and RT growth have been investigated in planar geometry using radiography of accelerated foils. The growth rates measured for CH foils are in excellent agreement with hydrocode simulations. The physics of the deceleration phase has been studied using a series of doped surrogate capsules. The main goal of these experiments was to develop techniques to diagnose the conditions in the shell (main fuel layer) and in the core (hot spot). The shell has been diagnosed using time-resolved spectroscopy of a Ti-doped tracer layer. With unsmoothed beams, experiments and simulations indicate that the shell is severely disrupted at time of shock convergence. When a Cl-doped ablator was used, the $\rho\Delta R$ inferred from the Ti absorption feature was much closer to 1-D predictions, confirming our diagnostic sensitivities to changes in target performance. These observations support the *ORCHID* simulations, which predict that the addition of a Cl-doped ablator results in a more intact shell.

The core has been diagnosed by both time-resolved neutron diagnostics and time-resolved spectroscopy of the Ar fuel dopant. From the analysis of the Ar line emission we find that the core conditions (electron densities and temperatures) just after the shock has reached the target center are close to those predicted by 1-D *LILAC* simulations. The same conclusion is reached from the analysis of the neutron-production rate. These conclusions are in qualitative agreement with *ORCHID* simulations, which predict near-spherical temperature profiles in the core. Conditions in the core deteriorate during compression and stagnation: both the electron temperature and density fail to reach *LILAC* predictions. This deterioration in core conditions occurs for both the square pulse and the Gaussian

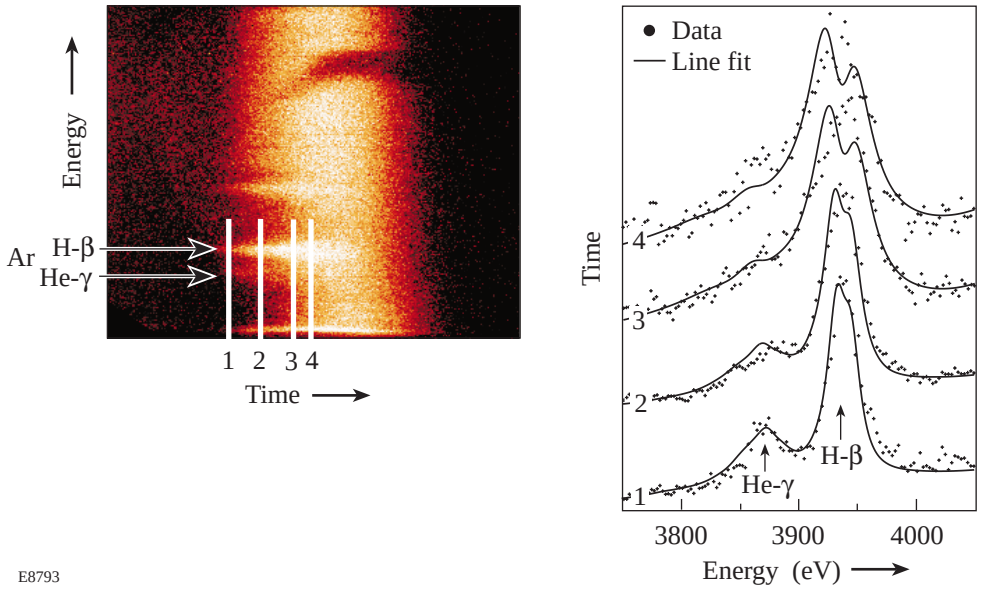

Figure 74.48
Time-resolved experimental spectrum and lineouts of the Ar H-β and He-γ lines for four times. The dots are the experimental values, and the lines are best fits from a quantum theory model combined with a non-LTE kinetics code[36–39] for a given electron temperature and density.

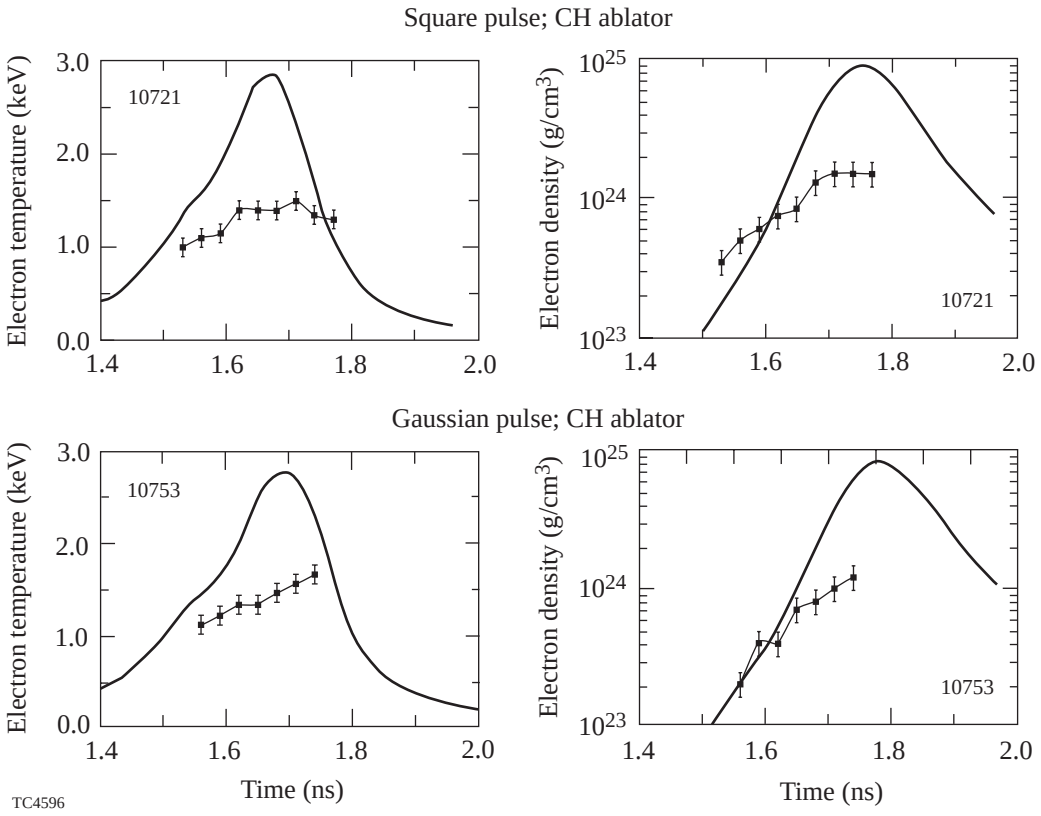

Figure 74.49
Measured and predicted electron temperatures and densities for the standard target for 1-ns square and Gaussian pulses. The predicted temperatures are mass-averaged temperatures from 1-D *LILAC* simulations (solid line).

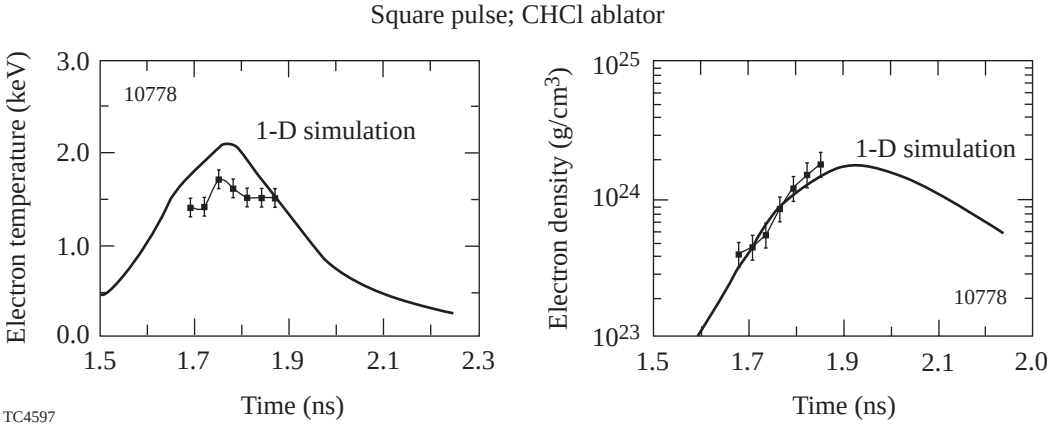

Figure 74.50
Measured and predicted electron temperatures and densities for the standard target and a Cl-doped-ablator target for a square pulse. The predicted temperatures are mass-averaged temperatures from 1-D *LILAC* simulations (solid line).

pulse. These observations indicate that final compression and resulting PdV work are not effective because the shell is probably not integral. Both diagnostics—time-resolved spectroscopy and neutron time detector—showed results that were closer to 1-D predictions when a Cl-doped ablator was used in agreement with simulations that predict reduced RT growth for those targets. The agreement between neutron and x-ray diagnostics is encouraging since cryogenic targets will be diagnosed primarily by neutron and charged-particle methods.

In conclusion, we have carried out initial mix implosion experiments with the unsmoothed OMEGA laser system to establish a base-line database for comparison with upcoming experiments in which full beam smoothing will have been implemented. We have also ascertained that the set of diagnostics used in these experiments can measure shell and core conditions and will enable us to study the effect of the RT instability on the main fuel layer (shell) and hot spot (core) in cryogenic targets.

ACKNOWLEDGMENT

This work was supported by the U.S. Department of Energy Office (DOE) of Inertial Confinement Fusion under Cooperative Agreement No. DE-FC03-92SF19460, the University of Rochester, and the New York State Energy Research and Development Authority. The support of DOE does not constitute an endorsement by DOE of the views expressed in this article.

REFERENCES

1. T. R. Boehly, D. L. Brown, R. S. Craxton, R. L. Keck, J. P. Knauer, J. H. Kelly, T. J. Kessler, S. A. Kumpan, S. J. Loucks, S. A. Letzring, F. J. Marshall, R. L. McCrory, S. F. B. Morse, W. Seka, J. M. Soures, and C. P. Verdon, Opt. Commun. **133**, 495 (1997).
2. Lord Rayleigh, Proc. London Math. Soc. **14**, 170 (1883); G. Taylor, Proc. R. Soc. London Ser. A **201**, 192 (1950).
3. R. D. Richtmyer, Commun. Pure. Appl. Math. **XIII**, 297 (1960); E. E. Meshkov, Izv. Akad. Nauk. SSSR Mekh. Zhidk. Gaza **4**, 33 (1970).
4. H. Takabe *et al.*, Phys. Fluids **28**, 3676 (1985).
5. R. Betti, V. N. Goncharov, R. L. McCrory, P. Sorotokin, and C. P. Verdon, Phys. Plasmas **3**, 2122 (1996).
6. O. L. Landen *et al.*, J. Quant. Spectrosc. Radiat. Transfer **54**, 245 (1995).
7. C. J. Keane *et al.*, J. Quant. Spectrosc. Radiat. Transfer **54**, 207 (1995).
8. O. L. Landen *et al.*, Phys. Plasmas **3**, 2094 (1996).
9. M. C. Richardson, P. W. McKenty, F. J. Marshall, C. P. Verdon, J. M. Soures, R. L. McCrory, O. Barnouin, R. S. Craxton, J. Delettrez, R. J. Hutchison, P. A. Jaanimagi, R. Keck, T. Kessler, H. Kim, S. A. Letzring, D. M. Roback, W. Seka, S. Skupsky, B. Yaakobi, S. M. Lane, and S. Prussin, in *Laser Interaction and Related Plasma Phenomena*, edited by H. Hora and G. H. Miley (Plenum Press, New York, 1986), Vol. 7, pp. 421–448.
10. B. I. Bennett *et al.*, Los Alamos National Laboratory Report LA-7130 (1978). Copies may be obtained from the National Technical Information Service, Springfield, VA 22161.
11. R. L. McCrory and C. P. Verdon, in *Inertial Confinement Fusion*, edited by A. Caruso and E. Sindoni (Editrice Compositori, Bologna, Italy, 1989), pp. 83–124.
12. D. H. Kalantar, M. H. Key, L. B. Da Silva, S. G. Glendinning, B. A. Remington, J. E. Rothenberg, F. Weber, S. V. Weber, E. Wolfrum, N. S. Kim, D. Neely, J. Zhang, J. S. Wark, A. Demir, J. Lin, R. Smith, G. J. Tallents, C. L. S. Lewis, A. MacPhee, J. Warwick, and J. P. Knauer, Phys. Plasmas **4**, 1985 (1997).
13. C. J. Pawley *et al.*, Phys. Plasmas **4**, 1969 (1997).
14. S. G. Glendinning, S. N. Dixit, B. A. Hammel, D. H. Kalantar, M. H. Key, J. D. Kilkenny, J. P. Knauer, D. M. Pennington, B. A. Remington, R. J. Wallace, and S. V. Weber, Phys. Rev. E **54**, 4473 (1996).
15. H. Azechi *et al.*, Phys. Plasmas **4**, 4079 (1997).
16. R. J. Taylor *et al.*, Phys. Rev. Lett. **76**, 1643 (1996).
17. T. R. Boehly, V. A. Smalyuk, D. D. Meyerhofer, J. P. Knauer, D. K. Bradley, C. P. Verdon, and D. Kalantar, in *Laser Interaction and Related Plasma Phenomena*, edited by G. H. Miley and E. M. Campbell (American Institute of Physics, Woodbury, NY, 1997), Vol. 406, pp. 122–129.
18. B. A. Remington *et al.*, Phys. Fluids B **4**, 967 (1992).
19. J. P. Knauer, C. P. Verdon, D. D. Meyerhofer, T. R. Boehly, D. K. Bradley, V. A. Smalyuk, D. Ofer, P. W. McKenty, S. G. Glendinning, D. H. Kalantar, R. G. Watt, P. L. Gobby, O. Willi, and R. J. Taylor, in *Laser Interaction and Related Plasma Phenomena*, edited by G. H. Miley and E. M. Campbell (American Institute of Physics, Woodbury, NY, 1997), Vol. 406, pp. 284–293.
20. J. Delettrez, D. K. Bradley, and C. P. Verdon, Phys. Plasmas **1**, 2342 (1994).
21. D. K. Bradley, J. A. Delettrez, and C. P. Verdon, Phys. Rev. Lett. **68**, 2774 (1992).
22. D. K. Bradley, T. Boehly, D. L. Brown, J. Delettrez, W. Seka, and D. Smith, in *Laser Interaction and Related Plasma Phenomena*, edited by H. Hora and G. Miley (Plenum Press, New York, 1991), Vol. 9, pp. 323–334.
23. S. W. Haan, Phys. Rev. A **39**, 5812 (1989).
24. Y. Lin, T. J. Kessler, and G. N. Lawrence, Opt. Lett. **20**, 764 (1995); Laboratory for Laser Energetics LLE Review **65**, 1, NTIS document No. DOE/SF/19460-117 (1995). Copies may be obtained from the National Technical Information Service, Springfield, VA 22161.
25. S. Skupsky, R. W. Short, T. Kessler, R. S. Craxton, S. Letzring, and J. M. Soures, J. Appl. Phys. **66**, 3456 (1989).

26. Laboratory for Laser Energetics LLE Review **45**, 1, NTIS document No. DOE/DP40200-149 (1990). Copies may be obtained from the National Technical Information Service, Springfield, VA 22161.

27. O. L. Landen, P. M. Bell, J. A. Oertel, J. J. Satariano, and D. K. Bradley, in *Ultrahigh- and High-Speed Photography, Videography, and Photonics '93*, edited by P. W. Roehrenbeck (SPIE, Bellingham, WA, 1993), Vol. 2002, pp. 2–13.

28. D. K. Bradley, P. M. Bell, J. D. Kilkenny, R. Hanks, O. Landen, P. A. Jaanimagi, P. W. McKenty, and C. P. Verdon, Rev. Sci. Instrum. **63**, 4813 (1992).

29. D. H. Kalantar *et al.*, in the *22nd International Congress on High-Speed Photography and Photonics*, edited by D. L. Paisley, and A. M. Frank (SPIE, Bellingham, WA, 1997), Vol. 2869, pp. 680–685.

30. B. Yaakobi, R. S. Craxton, R. Epstein, and Q. Su, J. Quant. Spectrosc. Radiat. Transfer **58**, 75 (1997).

31. B. Yaakobi, F. J. Marshall, D. K. Bradley, J. A. Delettrez, R. S. Craxton, and R. Epstein, Phys. Plasmas **4**, 3021 (1997).

32. R. A. Lerche, D. W. Phillion, and G. L. Tietbohl, in *Ultrahigh- and High-Speed Photography, Videography, and Photonics '93*, edited by P. W. Roehrenbeck (SPIE, Bellingham, WA, 1993), Vol. 2002, pp. 153–161.

33. T. J. Murphy and R. A. Lerche, *ICF Quarterly Report* **3**, 35, Lawrence Livermore National Laboratory, Livermore, CA, UCRL-LR-105821-93-1 (1992). Copies may be obtained from the National Technical Information Service, Springfield, VA 22161.

34. H. R. Griem, Phys. Fluids B **4**, 2346 (1992).

35. D. A. Haynes, Jr., D. T. Garber, C. F. Hooper, Jr., R. C. Mancini, Y. T. Lee, D. K. Bradley, J. Delettrez, R. Epstein, and P. A. Jaanimagi, Phys. Rev. E **53**, 1042 (1996).

36. R. C. Mancini *et al.*, Comput. Phys. Commun. **63**, 314 (1991).

37. L. A. Woltz and C. F. Hooper, Jr., Phys. Rev. A **38**, 4766 (1988).

38. Y. T. Lee, J. Quant. Spectrosc. Radiat. Transf. **38**, 131 (1987).

39. R. C. Mancini, R. F. Joyce, and C. F. Hooper, Jr., J. Phys. B: At. Mol. Phys **20**, 2975 (1987).

40. N. D. Delamater *et al.*, Phys. Rev. A **31**, 2460 (1985).

Accurate Formulas for the Landau Damping Rates of Electrostatic Waves

Laser–plasma instabilities[1] are important in the field of inertial confinement fusion[2] because they scatter laser light away from the target, which reduces the laser energy available to drive the compression of the nuclear fuel, or generate energetic electrons that preheat the fuel, which makes the fuel harder to compress. In stimulated Raman scattering an incident, or pump, light wave (0) decays into a frequency-downshifted, or Stokes, light wave (1) and an electron-plasma wave (2). In stimulated Brillouin scattering a pump light wave decays into a Stokes light wave and an ion-acoustic wave (2). The initial evolution of both instabilities is governed by the linearized equations[3]

$$\left(\partial_t + v_1\partial_z\right)A_1 = \gamma_0 A_2\,, \tag{1}$$

$$\left(\partial_t + \nu_2\right)A_2 = \gamma_0 A_1\,, \tag{2}$$

where A_1 and v_1 are the amplitude and group speed of the Stokes wave, respectively, A_2 and ν_2 are the amplitude and damping rate of the plasma wave (electron-plasma or ion-acoustic), respectively, and the coupling constant γ_0 is proportional to the amplitude of the pump wave. The convective amplification of an existing Stokes wave and the generation of a Stokes wave by plasma fluctuations are both characterized by the gain exponent[3]

$$g = \gamma_0^2 l/v_1\nu_2\,, \tag{3}$$

where l is the plasma length. Because the aforementioned parametric instabilities are important only when $g >> 1$, a small error in the damping rate of the plasma wave can produce a large error in the predicted amplitude of the Stokes wave. For this reason, it is important to determine accurately the Landau contribution to the damping rates of plasma waves.[4]

The properties of electrostatic plasma waves are determined by the dielectric function

$$\varepsilon(\omega,k) = 1 + \chi_e(\omega,k) + \chi_i(\omega,k), \tag{4}$$

where χ_e and χ_i denote the electron and ion susceptibilities, respectively. For each species s

$$\chi_s(\omega,k) = -\frac{\omega_s^2}{2v_s^2k^2}\,Z'\left(\frac{\omega}{\sqrt{2}v_s k}\right), \tag{5}$$

where ω_s is the plasma frequency, v_s is the thermal speed, and Z is the plasma dispersion function.[5] The electrostatic dispersion equation is simply

$$\varepsilon(\omega,k) = 0\,. \tag{6}$$

The solution of this dispersion equation has two branches: the high-frequency (electron-plasma) branch and the low-frequency (ion-acoustic) branch, both of which are studied in this article. In both cases our approximate analytical solution of the dispersion equation is compared to the numerical solution. Our analytical solutions are more accurate than the standard analytical solutions found in textbooks.[6–8]

Electron-Plasma Waves

The electron Debye length $\lambda_e = v_e/\omega_e$. For the case in which $k\lambda_e << 1$, Krall and Trivelpiece,[6] Ichimaru,[7] and Chen[8] all assert that

$$\omega_r \approx \omega_e\left[1 + 3\left(k\lambda_e\right)^2\right]^{1/2}, \tag{7}$$

$$\omega_i \approx -\left(\frac{\pi}{8}\right)^{1/2}\frac{\omega_e}{\left(k\lambda_e\right)^3}\exp\left[-\frac{1}{2\left(k\lambda_e\right)^2} - \frac{3}{2}\right]. \tag{8}$$

To gauge the accuracy of these formulas, we considered a numerical example. When $(k\lambda_e)^2 = 0.1$, formula (7) predicts that $\omega_r/\omega_e \approx 1.140$. The correct value of this frequency ratio, obtained by solving Eq. (4) numerically, with the ion term omitted, is 1.179. Formula (8) predicts that $\omega_i/\omega_e \approx 0.02979$, whereas the correct value is 0.01845. Although the predicted frequency is in error by only 3.3%, the predicted damping rate is in error by 61%. Clearly there is room for improvement.

In the aforementioned parameter regime $\omega \approx \omega_e$ and $\omega/v_e k \approx 1/(k\lambda_e) >> 1$. The electron-plasma dispersion function has the asymptotic expansion[5]

$$Z(\zeta) \sim i\sigma\pi^{1/2}\exp(-\zeta^2) - \sum_{n=0}^{\infty}\Gamma(n+1/2)/\left[\Gamma(1/2)\zeta^{2n+1}\right], \quad (9)$$

where

$$\sigma = \begin{cases} 0, & \text{if } \zeta_i > 1/|\zeta_r|, \\ 1, & \text{if } |\zeta_i| < 1/|\zeta_r|, \\ 2, & \text{if } \zeta_i < -1/|\zeta_r|, \end{cases} \quad (10)$$

$\Gamma(n+1/2) = (n-1/2)\Gamma(n-1/2)$ and $\Gamma(1/2) = \pi^{1/2}$. It is convenient to introduce the dimensionless parameters $K = k\lambda_e$ and $\Omega = \omega/\omega_e$. If one neglects the ion term in Eq. (4), the electron-plasma dispersion equation can be written as

$$D_r(\Omega) + iD_i(\Omega) = 0, \quad (11)$$

where

$$D_r(\Omega) = 1 - \sum_{n=1}^{\infty}(2n-1)!!\,K^{2n-2}/\Omega^{2n}, \quad (12)$$

$(2n-1)!! = (2n-1)(2n-3)\ldots(3)(1)$, and

$$D_i(\Omega) = \left(\frac{\pi}{2}\right)^{1/2}\frac{\Omega}{K^3}\exp\left(-\frac{\Omega^2}{2K^2}\right). \quad (13)$$

Because the exponent in Eq. (13) is proportional to $1/K^2$, $|D_i/D_r|$ and $|\Omega_i|/\Omega_r$ are exponentially small when $K^2 << 1$.

If one assumes that $|\Omega_i|/\Omega_r$ is less than any power of K required for an accurate solution of Eq. (11), then Ω_r is determined by the equation

$$D_r(\Omega_r) = 0 \quad (14)$$

and Ω_i is given by the formula

$$\Omega_i \approx -\left.\frac{D_i}{\partial D_r/\partial\Omega}\right|_{\Omega_r}. \quad (15)$$

By using Eq. (12) to evaluate the derivative in Eq. (13), one finds that

$$\Omega_i \approx -\left(\frac{\pi}{8}\right)^{1/2}\frac{C(\Omega_r)}{K^3}\exp\left(-\frac{\Omega_r^2}{2K^2}\right), \quad (16)$$

where the coefficient function

$$C(\Omega) = \Omega^4\Big/\left[\sum_{n=1}^{\infty} n(2n-1)!!\,K^{2n-2}/\Omega^{2n-2}\right]. \quad (17)$$

It is clear from Eqs. (12) and (17) that the dispersion equation (14) is an equation for Ω_r^2 that involves the small parameter K^2, and formula (16) depends on Ω_r^2. The efficient way to proceed is to solve Eq. (14) and evaluate formula (16) perturbatively, by expanding Ω_r^2 and D_r in powers of K^2. We chose to expand Ω_r and D_r in powers of K^2 to facilitate the analysis in the **Ion-Acoustic Waves** section. Specifically, we made the third-order expansions

$$\Omega \approx 1 + K^2\Omega_1 + K^4\Omega_2 + K^6\Omega_3, \quad (18)$$

$$D(\Omega) \approx D_0(\Omega) + K^2 D_1(\Omega) + K^4 D_2(\Omega) + K^6 D_3(\Omega), \quad (19)$$

where $D_0(\Omega) = 1 - 1/\Omega^2$, $D_1(\Omega) = -3/\Omega^4$, $D_2(\Omega) = -15/\Omega^6$, and $D_3(\Omega) = -105/\Omega^8$, and

$$D_n(\Omega) \approx D_n(1) + D_n'(1)(\Omega-1) + D_n''(\Omega-1)^2/2 + D_n'''(1)(\Omega-1)^3/6. \quad (20)$$

We substituted these expansions in Eq. (14) and collected terms of like order.

The zeroth-order equation is satisfied identically. The first-order equation is

$$D_0'\Omega_1 + D_1 = 0, \tag{21}$$

from which it follows that

$$\Omega_1 = 3/2. \tag{22}$$

The second-order equation is

$$D_0'\Omega_2 + D_0''\Omega_1^2/2 + D_1'\Omega_1 + D_2 = 0, \tag{23}$$

from which it follows that

$$\Omega_2 = 15/8. \tag{24}$$

The third-order equation is

$$D_0'\Omega_3 + D_0''\Omega_2\Omega_1 + D_0'''\Omega_1^3/6 + D_1'\Omega_2 + D_1''\Omega_1^2/2 + D_2'\Omega_1 + D_3 = 0, \tag{25}$$

from which it follows that

$$\Omega_3 = 147/16. \tag{26}$$

By combining Eqs. (22), (24), and (26), one finds that

$$\Omega_r \approx 1 + 3K^2/2 + 15K^4/8 + 147K^6/16, \tag{27}$$

from which it follows that

$$\Omega_r^2 \approx 1 + 3K^2 + 6K^4 + 24K^6. \tag{28}$$

Since the exponent in Eq. (16) is proportional to $1/K^2$, the third-order formula for Ω_r^2 determines the exponential term correct to second order. Consequently, one need only determine C correct to second order.[9] The result is

$$C \approx 1 - 6K^4. \tag{29}$$

It follows from Eqs. (16), (28), and (29) that

$$\Omega_i \approx -\left(\frac{\pi}{8}\right)^{1/2}\left(\frac{1}{K^3} - 6K\right) \times \exp\left(-\frac{1}{2K^2} - \frac{3}{2} - 3K^2 - 12K^4\right). \tag{30}$$

We refer to formulas (27) and (30) as the third-order formulas, even though the latter formula is only accurate to second order. In a similar way, one could refer to the textbook formulas as the first-order formulas. Notice, however, that the textbook formula $\Omega_r \approx (1+3K)^{1/2}$ is less accurate than the true first-order formula $\Omega_r \approx 1 + 3K/2$.

The approximate analytical solutions of the electron-plasma dispersion equation are compared to the numerical solution in Fig. 74.51. The dashed lines represent the textbook solution, the solid lines represent the third-order solution, and the dotted lines represent the numerical solution. For $K^2 = 0.1$ the third-order formulas predict that $\Omega_r \approx 1.178$ and $\Omega_i \approx 0.01840$. These values of Ω_r and Ω_i differ from the correct values by 0.085% and 0.27%, respectively. For the displayed range of K^2 the maximal error associated with the third-order formula for Ω_r is 0.57% and the maximal error associated with the third-order formula for Ω_i is 14%. The third-order formulas are more accurate than the textbook formulas, even though the assumption on which they are based, that $|\Omega_i|/\Omega_r << K^6$, is only valid for $K^2 < 0.04$. Neither pair of formulas is accurate when K^2 is significantly larger than 0.1.

Ion-Acoustic Waves

The electron contribution to the ion-acoustic speed $c_e = (ZT_e/m_i)^{1/2}$, where Z is the ionization number. For the case in which $k\lambda_e << 1$ and $T_i/ZT_e << 1$, we define the baseline formulas

$$\omega_r \approx c_e k\left(1 + 3T_i/ZT_e\right)^{1/2}, \tag{31}$$

$$\frac{\omega_i}{c_e k} \approx -\left(\frac{\pi}{8}\right)^{1/2}\left[\left(\frac{Zm_e}{m_i}\right)^{1/2} + \left(\frac{ZT_e}{T_i}\right)^{3/2}\exp\left(-\frac{ZT_e}{2T_i} - \frac{3}{2}\right)\right]. \tag{32}$$

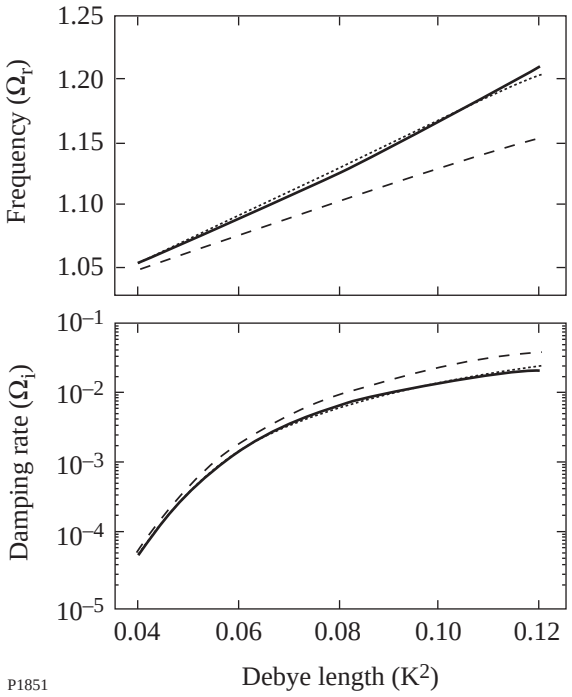

Figure 74.51
(a) Normalized frequency (ω_r/ω_e) and (b) damping rate (ω_i/ω_e) of an electron-plasma wave plotted as functions of the square of the normalized Debye length ($k\lambda_e$). The dashed lines represent the textbook formulas (7) and (8), the solid lines represent the third-order formulas (27) and (30), and the dotted lines denote numerical solutions of the electron-plasma dispersion equation.

Krall and Trivelpiece[6] omit the ion-temperature contribution to the frequency (31) and the associated factor of exp(–3/2) in the ion contribution to the damping rate (32). Ichimaru[7] and Chen[8] retain these ion-temperature contributions. They agree on formula (31) for the frequency but differ on the formula for the damping rate. Ichimaru multiplies formula (32) by a factor of $\left(1+3T_i/ZT_e\right)^{1/2}$, whereas Chen, who considers only the ion contribution to the damping rate, multiplies the ion term in formula (32) by a factor of $1+3T_i/ZT_e$. In a recent paper[10] we showed empirically that Ichimaru's formula for the damping rate is the better of the two. To gauge the accuracy of Ichimaru's formulas, we considered a numerical example: When $T_i/ZT_e = 0.1$, formula (31) predicts that $\omega_r/c_e k \approx 1.140$. The correct value of the frequency ratio, obtained by solving Eq. (4) numerically with $k\lambda_e = 0.001$, is 1.181. Formula (32), multiplied by $\left(1+3T_i/ZT_e\right)^{1/2}$, predicts that $\omega_i/c_e k \approx 0.05064$, whereas the correct value is 0.03219. Although the predicted frequency is only in error by 3.4%, the predicted damping rate is in error by 57%. [For comparison, the damping rate predicted by formula (32) is in error by 38%.] Clearly there is room for improvement in the accuracy of the formula for the damping rate and the self-consistency of the method by which it is derived.

In the aforementioned parameter regime $\omega \approx c_e k$, $\omega/v_e k \approx \left(Zm_e/m_i\right)^{1/2} << 1$, and $\omega/v_i k \approx \left(ZT_e/T_i\right)^{1/2} >> 1$. One can use the expansion[5]

$$Z(\varsigma) = i\pi^{1/2}\exp\left(-\varsigma^2\right) - \varsigma\sum_{n=0}^{\infty}\left(-\varsigma^2\right)^n \Gamma(1/2)/\Gamma(n+3/2) \quad (33)$$

for the electron-plasma dispersion function and expansion (9) for the ion-plasma dispersion function. It is convenient to introduce the dimensionless parameters $T = T_i/ZT_e$ and $\Omega = \omega/c_e k$.

If one makes the assumption that $Z'(\varsigma_e) \approx -2$, which omits the electron contribution to the ion-acoustic damping rate, the ion-acoustic dispersion relation can be written in the form of Eq. (11), where

$$D_r(\Omega) = 1 + K^2 - \sum_{n=1}^{\infty}(2n-1)!!\,T^{n-1}/\Omega^{2n}, \quad (34)$$

$$D_i(\Omega) = \left(\frac{\pi}{2}\right)^{1/2}\frac{\Omega}{T^{3/2}}\exp\left(-\frac{\Omega^2}{2T}\right). \quad (35)$$

Since the dispersion functions can be rewritten as

$$\frac{D_r(\Omega)}{\left(1+K^2\right)} = 1 - \sum_{n=1}^{\infty}\frac{(2n-1)!!\left[T\left(1+K^2\right)\right]^{n-1}}{\left[\Omega^2\left(1+K^2\right)\right]^n}, \quad (36)$$

$$\frac{D_i(\Omega)}{\left(1+K^2\right)} = \left(\frac{\pi}{2}\right)^{1/2}\frac{\left[\Omega^2\left(1+K^2\right)\right]^{1/2}}{\left[T\left(1+K^2\right)\right]^{3/2}}\exp\left[-\frac{\Omega^2\left(1+K^2\right)}{2T\left(1+K^2\right)}\right], \quad (37)$$

Ω_r and Ω_i satisfy the equation

$$\Omega[K,T] = \Omega\left[0, T\left(1+K^2\right)\right]\Big/\left(1+K^2\right)^{1/2}. \quad (38)$$

Thus, one need only solve the ion-acoustic dispersion equation for the case in which $K^2 = 0$. In this case Eq. (34) has the same

form as Eq. (12), with K^2 replaced by T. It follows from this observation, and Eqs. (27) and (30), that the third-order solution is

$$\Omega_r \approx 1 + 3T/2 + 15T^2/8 + 147T^3/16, \tag{39}$$

$$\Omega_i \approx -\left(\frac{\pi}{8}\right)^{1/2}\left(\frac{1}{T^{3/2}} - 6T^{1/2}\right) \times \exp\left(-\frac{1}{2T} - \frac{3}{2} - 3T - 12T^2\right). \tag{40}$$

Equations (38)–(40) apply to all values of K^2 that satisfy the inequality $T(1 + K^2) << 1$.

If one makes the approximation $Z'(\zeta_e) \approx -2 - i\pi^{1/2}\zeta_e$, which retains the electron contribution to the ion-acoustic damping rate, one must add to Eq. (35) the term

$$D_i(\Omega) = i\left(\frac{\pi}{2}\right)^{1/2} \Omega M^{1/2}, \tag{41}$$

where $M = Zm_e/m_i$ and Z is the ionization number. Since

$$\frac{D_i(\Omega)}{1+K^2} = i\left(\frac{\pi}{2}\right)^{1/2} \frac{\left[\Omega^2\left(1+K^2\right)\right]^{1/2} M^{1/2}}{\left(1+K^2\right)^{3/2}}, \tag{42}$$

Ω_r and Ω_i satisfy the equation

$$\Omega[K, M, T] = \Omega\left[0, M/\left(1+K^2\right)^3, T\left(1+K^2\right)\right]/\left(1+K^2\right)^{1/2}. \tag{43}$$

Thus, one need only solve the ion-acoustic dispersion equation for the case in which $K^2 = 0$.

Unlike the ion contribution to D_i, the electron contribution is not exponentially small when $T << 1$, so one cannot evaluate formula (15) correct to an arbitrary power of T. This formula suggests, however, that the electron contribution to Ω_i is of order 0.01. It follows from Eq. (40) and Fig. 74.51(b) that the ion contribution to Ω_i is much smaller than the electron contribution for $T \le 0.06$ and is comparable to the electron contribution for $0.08 \le T \le 0.12$. In the latter range, both contributions to Ω_i are of order T^2. To make a perturbation expansion based on this ordering, we defined the damping parameters

$$\Gamma = \left(\frac{\pi}{8}\right)^{1/2} \frac{M^{1/2}}{T^2}, \tag{44}$$

$$\Delta = \left(\frac{\pi}{8}\right)^{1/2} \frac{1}{T^{7/2}} \exp\left(-\frac{1}{2T} - \frac{3}{2}\right) \tag{45}$$

and made the approximation

$$\exp\left(-\frac{\Omega^2}{2T}\right) \approx \exp\left(-\frac{1}{2T} - \frac{3}{2}\right)\left[1 - T\left(\Omega_2 + \frac{\Omega_1^2}{2}\right)\right], \tag{46}$$

which allowed us to write the real dispersion function as

$$D_r(\Omega) \approx D_{0r} + TD_{1r} + T^2 D_{2r} + T^3 D_{3r}, \tag{47}$$

where D_{0r}–D_{2r} were defined after Eq. (19) and

$$D_{3r} = -105 - 2\Delta\Omega_{2i}, \tag{48}$$

and the imaginary dispersion function as

$$D_i(\Omega) \approx T^2 D_{2i} + T^3 D_{3i}, \tag{49}$$

where

$$D_{2i} = 2(\Gamma + \Delta), \tag{50}$$

$$D_{3i} = 2\left[\Omega_{1r}(\Gamma + \Delta) - \Delta\left(\Omega_{2r} + \Omega_{1r}^2/2\right)\right]. \tag{51}$$

We then proceeded as described in the **Electron-Plasma Waves** section.

The zeroth-order and first-order equations are identical to the corresponding equations of the previous section, so $\Omega_{1r} =$

3/2 and $\Omega_{1i} = 0$ as we assumed in Eq. (46). The second-order equation is

$$D'_{0r}\left(\Omega_{2r} + i\Omega_{2i}\right) + D''_{0r}\Omega_{1r}^2/2 + D'_{1r}\Omega_{1r} + D_{2r} + iD_{2i} = 0, \quad (52)$$

from which it follows that

$$\Omega_{2r} = 15/8, \quad (53)$$

$$\Omega_{2i} = -(\Gamma + \Delta). \quad (54)$$

Formula (54) is equivalent to the base-line formula (32). The third-order equation is

$$\begin{aligned} &D'_{0r}\left(\Omega_{3r} + i\Omega_{3i}\right) \\ &+D''_{0r}\left(\Omega_{2r} + i\Omega_{2i}\right)\Omega_{1r} \\ &+ D'''_{0r}\Omega_{1r}^3/6 \\ &+D'_{1r}\left(\Omega_{2r} + i\Omega_{2i}\right) \\ &+ D''_{1r}\Omega_{1r}^2/2 + D'_{2r}\Omega_{1r} + D_{3r} + iD_{3i} = 0, \end{aligned} \quad (55)$$

from which it follows that

$$\Omega_{3r} = 147/16 + \Delta(\Gamma + \Delta), \quad (56)$$

$$\Omega_{3i} = \Delta\left(\Omega_{2r} + \Omega_{1r}^2/2\right). \quad (57)$$

By combining Eqs. (53) and (56), one finds that

$$\Omega_r \approx 1 + 3T/2 + 15T^2/8 + \left[147/16 + \Delta(\Gamma + \Delta)\right]T^3. \quad (58)$$

By combining Eqs. (54) and (57), one finds that

$$\Omega_i = -T^2\left\{\Gamma + \Delta\left[1 - T\left(\Omega_{2r} + \Omega_{1r}^2/2\right)\right]\right\}. \quad (59)$$

It is clear from Eq. (46) that the Δ terms represent the exponential $\exp\left(-\Omega_r^2/2T\right)$, with the exponent evaluated correct to first order; thus, one can rewrite Eq. (59) as

$$\Omega_i \approx -\left(\frac{\pi}{8}\right)^{1/2}\left[M^{1/2} + \frac{1}{T^{3/2}}\exp\left(-\frac{1}{2T} - \frac{3}{2} - 3T\right)\right]. \quad (60)$$

Notice that the algebraic factors of Ichimaru and Chen are both absent. We refer to formulas (58) and (60) as the third-order formulas, even though the exponent in the latter formula is only accurate to first order.

The approximate analytical solutions of the ion-acoustic dispersion equation are compared to the numerical solution in Fig. 74.52. The dashed lines represent Ichimaru's solution, the solid lines represent the third-order solution, and the dotted lines represent the numerical solution. For $T = 0.1$ formula (58) predicts that $\Omega_r \approx 1.191$, which differs from the correct value of Ω_r by 0.85%. It is clear from Figs. 74.51(a) and 74.52(a) that the additional third-order term improves the accuracy of the formula in the range $T \leq 0.09$ but decreases the accuracy in the

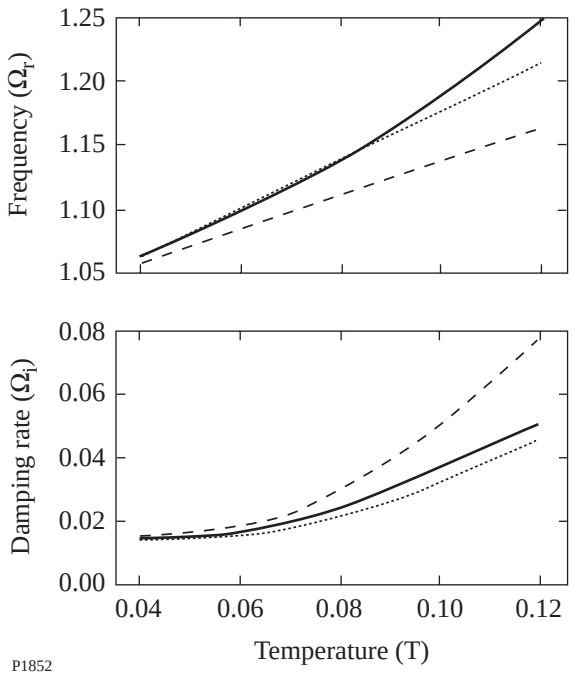

Figure 74.52
(a) Normalized frequency $\left(\omega_r/c_e k\right)$ and (b) damping rate $\left(\omega_i/c_e k\right)$ of an ion-acoustic wave plotted as functions of the temperature ratio $\left(T_i/ZT_e\right)$. The dashed lines represent Ichimaru's formulas (31) and (32) multiplied by $\left(1 + 3T_i/ZT_e\right)^{1/2}$, the solid lines represent the third-order formulas (58) and (60), and the dotted lines denote numerical solutions of the ion-acoustic dispersion equation.

range $T > 0.09$. Formula (60) predicts that $\Omega_i \approx 0.03670$, which differs from the correct value of Ω_i by 14%. For the displayed range of T the maximal error associated with the third-order formula for Ω_r is 2.7% and the maximal error associated with the third-order formula for Ω_i is 14%. The third-order formulas are more accurate than Ichimaru's formulas. Neither pair of formulas is accurate when T is significantly larger than 0.1.

Summary

We used systematic perturbation methods to derive formulas for the Landau damping rates of electron-plasma waves [Eq. (30)] and ion-acoustic waves [Eq. (60)]. The predictions of these formulas were compared to the predictions of the textbook formulas[6–8] and numerical solutions of the electrostatic dispersion equation. When $(k\lambda_e)2 \le 0.1$ (for electron-plasma waves) and $T_i/ZT_e \le 0.1$ (for ion-acoustic waves), our formulas are more accurate than the textbook formulas. When $(k\lambda_e)^2 > 0.1$ and $T_i/ZT_e > 0.1$, no pair of formulas is accurate and the electrostatic dispersion equation must be solved numerically.

ACKNOWLEDGMENT

This work was supported by the U.S. Department of Energy Office of Inertial Confinement Fusion under Cooperative Agreement No. DE-FC03-92SF19460, the University of Rochester, and the New York State Energy Research and Development Authority. The support of DOE does not constitute an endorsement by DOE of the views expressed in this article.

REFERENCES

1. W. L. Kruer, *The Physics of Laser Plasma Interactions*, Frontiers in Physics, Vol. 73, edited by D. Pines (Addison-Wesley, Redwood City, CA, 1988), Chaps. 7 and 8.

2. R. L. McCrory and J. M. Soures, in *Laser-Induced Plasmas and Applications*, edited by L. J. Radziemski and D. A. Cremers (Dekker, New York, 1989), pp. 207–268.

3. R. E. Giacone, C. J. McKinstrie, and R. Betti, Phys. Plasmas **2**, 4596 (1995) and references therein.

4. L. Landau, J. Phys., USSR **X**, 25 (1946).

5. J. D. Huba, NRL Plasma Formulary, Naval Research Laboratory, NRL/PU/6790—94-265 (1994) and references therein.

6. N. A. Krall and A. W. Trivelpiece, *Principles of Plasma Physics* (McGraw-Hill, New York, 1973), pp. 385 and 390.

7. S. Ichimaru, *Basic Principles of Plasma Physics* (W. A. Benjamin, Reading, MA, 1973), p. 71.

8. F. F. Chen, *Introduction to Plasma Physics and Controlled Fusion*, Vol. 1, 2nd ed. (Plenum Press, New York, 1984), pp. 270–273.

9. For the record, the third-order contribution to C is $-48K^6$. The fourth-order equation is $D_0'\Omega_4 + D_0''\Omega_3\Omega_1 + D_0''\Omega_2^2/2 + D_0'''\Omega_2\Omega_1^2/2 + D_0''''\Omega_1^4/24 + D_1'\Omega_3 + D_1''\Omega_2\Omega_1 + D_1'''\Omega_1^3/6 + D_2'\Omega_2 + D_2''\Omega_1^2/2 + D_3'\Omega_1 + D_4 = 0$, from which it follows that $\Omega_4 = 9531/128$. The fourth-order correction to Ω_r^2 is $180K^8$. For $K^2 \le 0.1$ the fourth-order formulas for Ω_r and Ω_i are more accurate than the third-order formulas. As K^2 increases beyond 0.1, however, the predictions of the fourth-order formulas diverge from the numerical results more rapidly than the predictions of the third-order formulas.

10. R. E. Giacone, C. J. McKinstrie, and R. Betti, Phys. Plasmas **5**, 1218 (1998).

Efficient, End-Pumped, 1053-nm Nd:YLF Laser

Diode-pumped lasers offer better stability and higher reliability than flashlamp-pumped laser systems. Most of the diode-pumping schemes can be divided into two major categories: end pumping and side pumping. High efficiency and good beam quality are potential advantages of end-pumped solid-state lasers over side-pumped ones. Practical realization of these advantages depends upon the possibility of reshaping a strongly astigmatic diode-laser beam into a beam with a circular symmetry. Recently, several practical schemes were suggested[1,2] that make it possible to effectively re-image the 1-μm × 10-mm emitting area of a high-power, cw laser diode bar into a few-hundred-micron spot size. These techniques have been used successfully for direct cw end pumping of solid-state lasers[1] and the efficient coupling of high-power, cw laser-diode radiation into the optical fiber.[2] Using a transport fiber to deliver the pump beam to the end-pumped active medium has a number of practical advantages: (a) the pump beam at the transport fiber output has a high-quality, centrally symmetric energy distribution; (b) the radial size of the pump beam can be easily up- or down-scaled by using simple and virtually lossless optics; (c) a transport fiber provides a simple and transparent interface between the pump source and the active medium, which greatly simplifies the whole diode-pumped laser characterization and maintenance; and (d) both the pumping source and the active medium can be changed simply by reconnecting transport fibers. Therefore, it seems very attractive to couple the high-power, quasi-cw diode laser into the optical fiber and to use this fiber-coupled, quasi-cw, high-power laser diode to end pump a solid-state laser.

In this article we report on an efficient Nd:YLF laser operated at 1053 nm that was end pumped by fiber-coupled, high-power, pulsed diode arrays. Two quasi-cw 100-W linear arrays[3] were used in this experiment. The emitting area of these diodes was 1 μm × 10 mm with ~100% aperture fill factor. The diode laser's 3.6-nm-wide output spectrum was centered at 805 nm. The output from the laser-diode arrays was coupled into 0.6-mm-diam, 0.22-numerical-aperture step-index fibers in a manner similar to that reported in Ref. 2. Fiber-coupling efficiencies of >50% were measured at the maximum diode-laser output (Fig. 74.53). At the transport fiber output the laser-diode radiation was re-imaged with 1.6× magnification into the Nd:YLF rod through a beam splitter that was HR coated for 1053 nm (R > 99%) and AR coated for 805 nm (R < 1.5%). In the course of our experiments we investigated a Nd:YLF rod pumped from one side by a single diode array and pumped from both sides by two arrays simultaneously. The pump energy that reached each of the Nd:YLF rod surfaces was ≥25 mJ for the 0.5-ms pump duration. This represents ~50% transport efficiency from the emitting surface of the laser diode to the input surface of the Nd:YLF active element. The active laser element was a 5-mm-diam, 20-mm-long Nd:YLF rod with 1.1 atm% of Nd and AR coated for 805 nm and 1053 nm on both sides. The focused pump beam formed a circularly symmetric spot on the input faces of the Nd:YLF rod with a pump beam cross section of ≤1.3-mm FWHM over the entire 20-mm length of the laser crystal (Fig. 74.54). More than 95% of the pump energy was absorbed in the Nd:YLF crystal. We found that for this pumping scheme the Nd:YLF lasing threshold at 1053 nm is insensitive to pump-wavelength variation within at least ±2 nm. We attribute this to the fact that Nd:YLF has a broad and almost–polarization-insensitive absorption

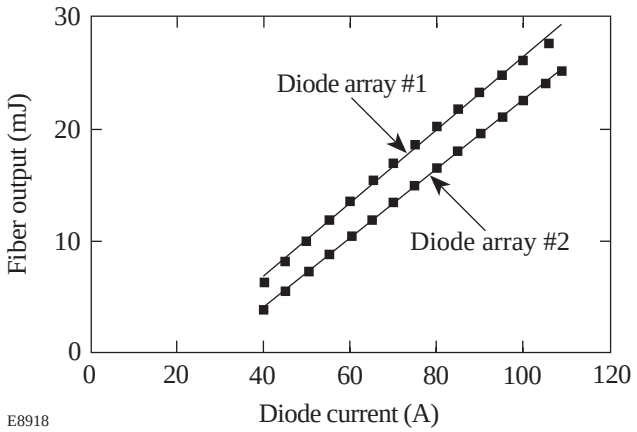

Figure 74.53
Fiber-coupled, 100-W, quasi-cw diode-array output versus diode current. Data presented are for the 0.6-mm-diam, 0.22-NA step-index fiber.

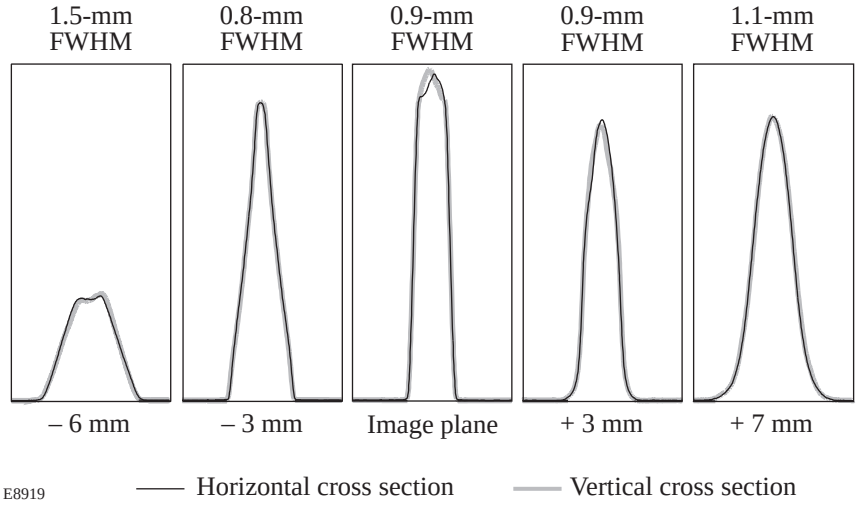

Figure 74.54
Pump-beam cross section along the axis of the active medium.

peak around 805 nm, which eliminates the need for the laser diode to be precisely wavelength tuned and externally cooled when the laser repetition rate is below 5 Hz. It should be pointed out that although all data presented here were taken at a 5-Hz repetition rate, we believe that a higher repetition rate can easily be achieved with proper heat removal from the diode laser and the active element.

The gain of the end-pumped rod was determined using a cw mode-locked Nd:YLF laser operated at 1053 nm that was collimated and apertured so that the probe beam used was ~1 mm in diameter. The single-pass, small-signal gain G_{ss} for the probe beam was observed with an analog oscilloscope[4] and measured with a digital oscilloscope.[5] The measured small-signal, single-pass gain for the ~1-mm beam at 1053 nm was 2.2 for pumping from one side and 4.2 for pumping from both sides (Fig. 74.55).

For the end-pumped Nd:YLF laser demonstration and characterization the following setup was used (Fig. 74.56): The cavity was 3.78 m in length and used a flat output coupler and a high reflector with a 5-m radius of curvature. Output couplers with reflectivity R = 85%, 70%, and 50% were tested. The 1053-nm wavelength for the Nd:YLF lasing was insured by the intracavity thin-film polarizer and appropriate Nd:YLF rod orientation in respect to this polarizer. The polarization of the output laser radiation was monitored by the extra-cavity Glan–Taylor polarizer. At the maximum one-sided pumping energy of ~27 mJ, the free-running output was 8.8 mJ in the multilongitudinal, fundamental TEM_{00} mode, which is 33% of the pump energy delivered to the Nd:YLF rod surface. At the maximum two-sided pump energy of 50 mJ, the free-running output was 20 mJ in the multilongitudinal fundamental TEM_{00} mode, which is 40% of the pump energy delivered to the Nd:YLF rod surface (Fig. 74.57). We believe that this is the highest TEM_{00} energy output reported to date for an end-pumped Nd:YLF laser operated at 1053 nm. The measured optical-to-optical differential efficiency was 54%. The spatial profile for the output beam was measured with a scientific-grade, cooled CCD camera.[6] The highly symmetric output beam has an intensity distribution very close to the intensity distribution calculated for our laser resonator parameters at 6.4-mJ output energy for the one-side pumping scheme (see Fig. 74.58). It should be emphasized that we observed the TEM_{00} output beam without any transverse mode control aperture in the cavity for the entire range of the pumping energies up to six times the threshold. We believe that this is attributed to the fact that the end-pumped volume cross section was smaller than the fundamental-mode cross section.[7]

The Q-switched mode of operation was also tested. To convert the Nd:YLF laser from the free-running mode to the Q-switching mode, a standard combination of the quarter-wave plate and Pockels cell was introduced into the laser cavity between the thin-film polarizer and the end mirror (Fig. 74.56). The reflectivity of the output coupler used for the Q-switched-mode operation was R = 70%. A high-voltage, step-function pulse was applied to the Pockels cell at the end of the pumping cycle to initiate the Nd:YLF laser Q-switching. The amplitude of this high-voltage pulse adjusted for maximum output energy at the highest pumping level (both ends pumping) was found to be 4.5 kV. The measured output energy in the Q-switched mode was 13.6 mJ (Fig. 74.59), and the Q-switched output pulse has a TEM_{00}-mode profile. The measured temporal FWHM of the Q-switched output pulse was 140 ns, which is less than six laser-resonator-cavity round-trips (Fig. 74.60).

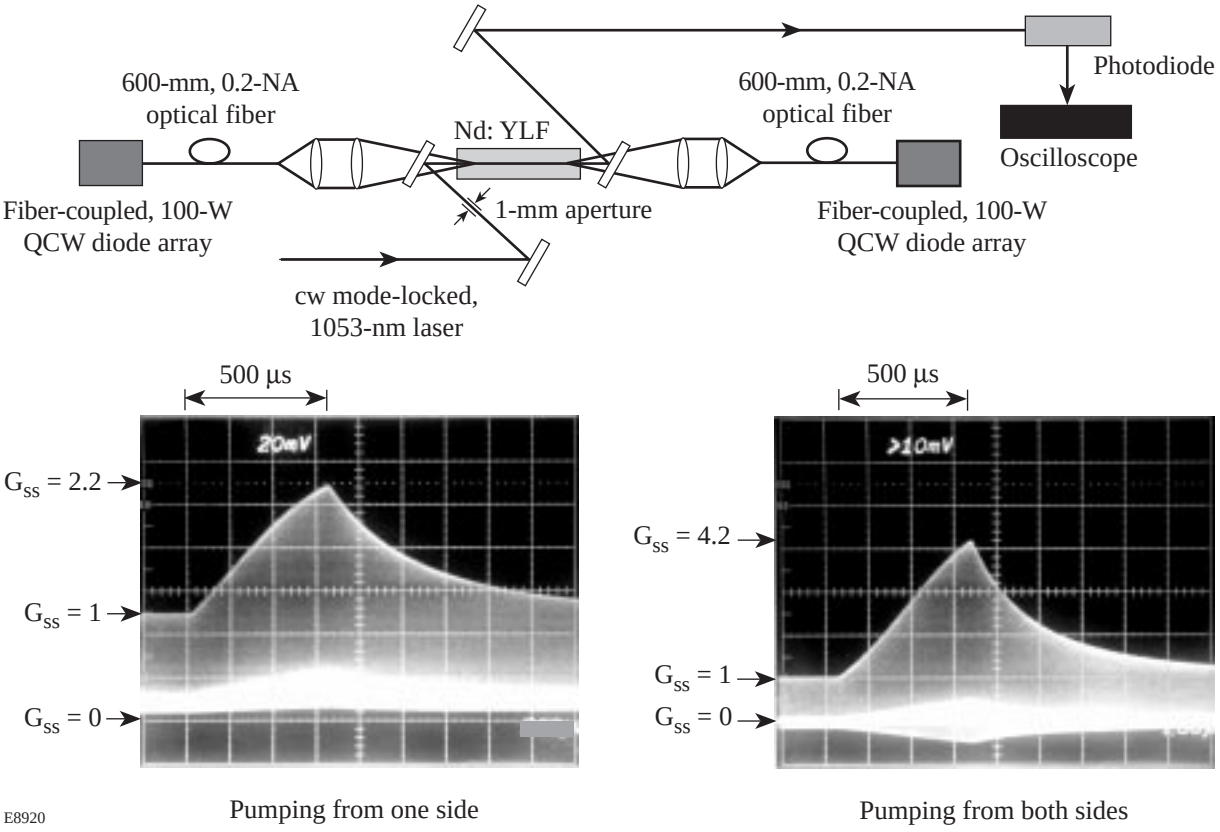

Figure 74.55
Small-signal-gain measurements: setup and experimental results.

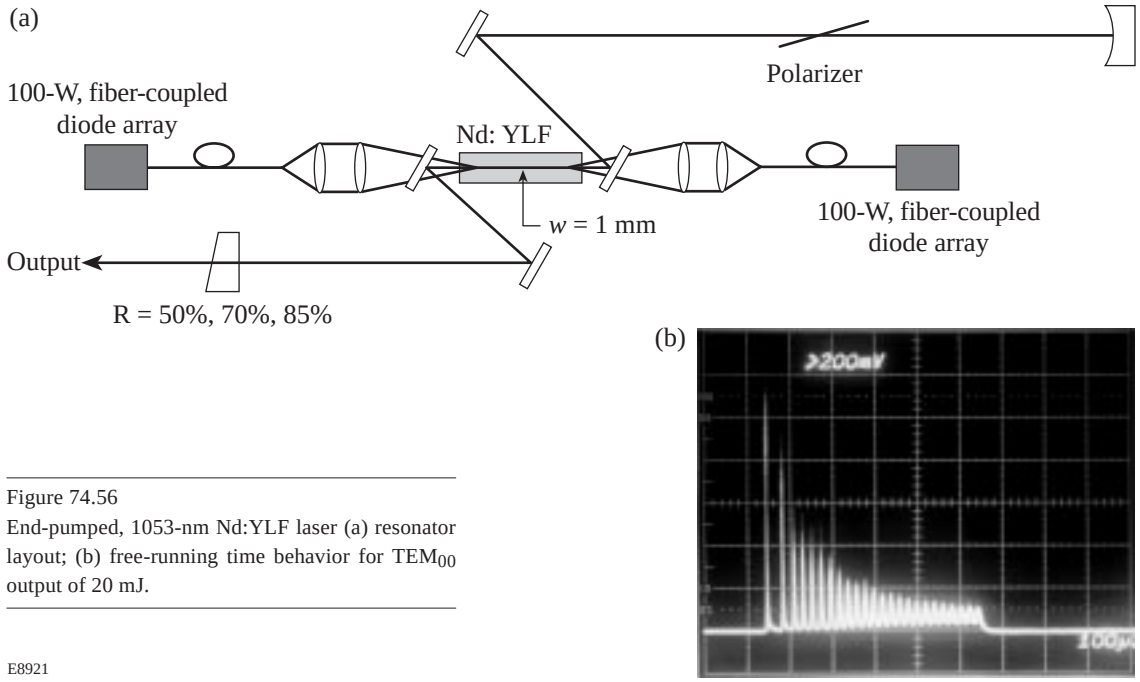

Figure 74.56
End-pumped, 1053-nm Nd:YLF laser (a) resonator layout; (b) free-running time behavior for TEM_{00} output of 20 mJ.

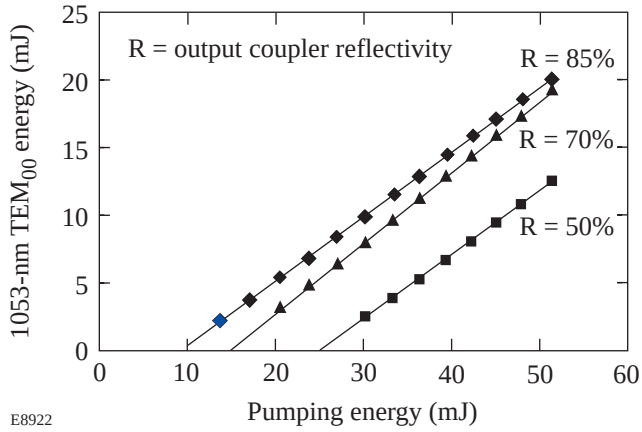

Figure 74.57
Measured, free-running, laser TEM_{00}-mode energy output at 1053 nm versus pump energy.

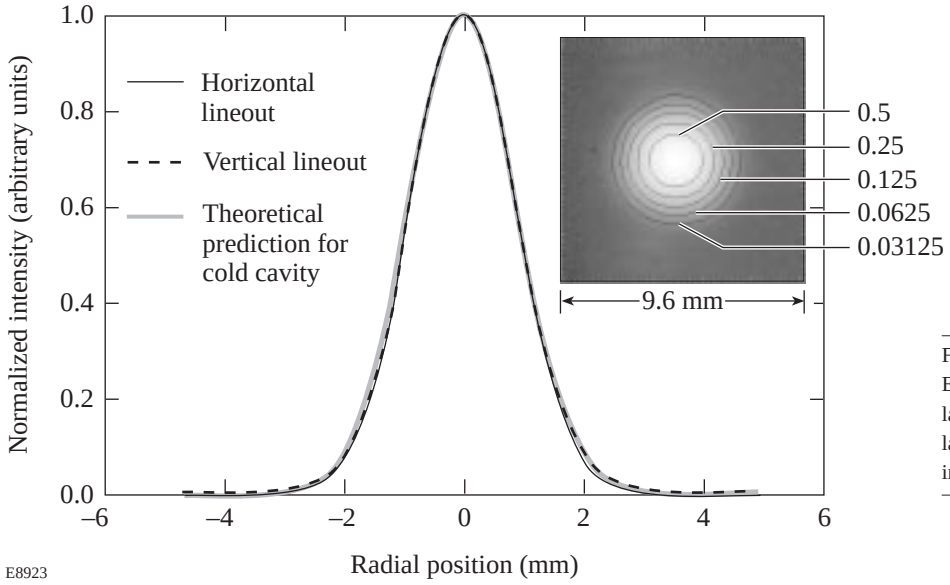

Figure 74.58
Experimentally measured and calculated output laser intensity beam profiles. An image of the laser beam on the logarithmic scale with superimposed contour lines is shown in the inset.

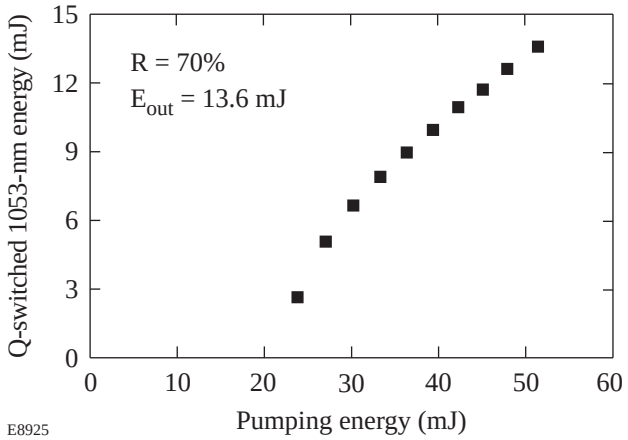

Figure 74.59
Measured *Q*-switched TEM_{00}-mode energy output versus pump energy.

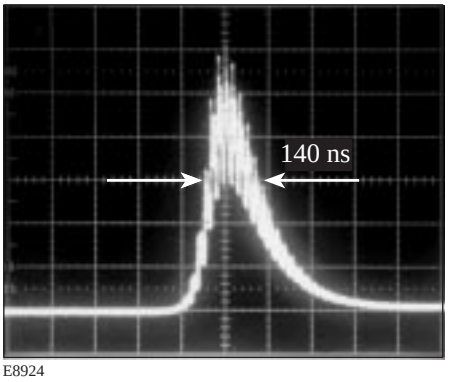

Figure 74.60
Q-switching pulse temporal profile for TEM_{00} output of 13.6 mJ.

In conclusion we developed an efficient Nd:YLF laser at 1053 nm that was end pumped by two fiber-coupled, 100-W, quasi-cw diode arrays. A 20-mJ TEM_{00} energy output with 54% differential efficiency for a free-running mode and 13.6-mJ TEM_{00} energy output for *Q*-switched operation were demonstrated. We believe that this is the highest TEM_{00} energy output reported to date for the efficient end-pumped Nd:YLF laser operated at 1053-nm wavelength.

ACKNOWLEDGMENT

This work was supported by the U.S. Department of Energy Office of Inertial Confinement Fusion under Cooperative Agreement No. DE-FC03-92SF19460, the University of Rochester, and the New York State Energy Research and Development Authority. The support of DOE does not constitute an endorsement by DOE of the views expressed in this article.

REFERENCES

1. W. A. Clarkson and D. C. Hanna, Opt. Lett. **21**, 375 (1996).
2. K. Du *et al*., in *Advanced Solid State Lasers, 1997*, edited by C. R. Pollock and W. R. Bosenberg, OSA Trends in Optics and Photonics Series, Vol. 10 (Optical Society of America, Washington, DC, 1997), pp. 390–393.
3. Diode array SDL 3251-A1, SDL, Inc., San Jose, CA 95134-1365.
4. Tektronix oscilloscope 7104, Tektronix, Corporate Office, Wilsonville, OR 97070-1000.
5. Hewlett-Packard oscilloscope HP54720A, Hewlett-Packard, Test and Measurement Organization, Palo Alto, CA 94303-9512.
6. 5122 CCD detector model 1530-PUV, EG&G Instruments, Princeton Applied Research, Princeton, NJ 08543-2565.
7. F. Salin and J. Squier, Opt. Lett. **17**, 1352 (1992).

Self- and Cross-Phase-Modulation Coefficients in KDP Crystals Measured by a *Z*-Scan Technique

In the interaction of strong fields with matter, considerable interest has been shown in the development of high-efficiency frequency up-conversion of ultrashort laser pulses. One important area of interest is in ultrafast laser–solid interactions where up-conversion can lead to higher absorption due to higher-density interactions[1] and to an enhancement of the pulse-intensity contrast by many orders of magnitude, allowing the high-intensity pulse to interact with the solid-density material.[2] Efficient second-harmonic generation in KDP has been reported for ultrafast laser beams at intensities up to 400 GW/cm^2.[3] In this intensity region, nonlinear effects such as self- and cross-phase modulation[4,5] (SPM, XPM) originating from third-order nonlinear susceptibility $\chi^{(3)}$ may limit the efficiency of ultra-intense frequency-conversion processes that involve co-propagation of two beams with different wavelengths. SPM and XPM are responsible for spectral broadening in optical fibers and have been used in pulse compression to produce ultrashort laser pulses.[6] XPM has been observed in fiber Raman soliton lasers[7,8] and has proven to be important in optical parametric oscillators, optical parametric amplifiers,[9] and the harmonic-generation process in bulk nonlinear crystals.[10,11] Nonlinear phase changes can destroy the phase coherence required for efficient conversion. *Z*-scan,[12,13] four-wave mixing,[14,15] ellipse rotation,[16] and nonlinear interferometer[17,18] techniques have been used to measure the nonlinear refractive index $n_2\left[n_2 = 3/8n\chi^{(3)}\right]$ associated with SPM. Nonlinear refractive index coefficients associated with SPM in KDP crystals, which are widely used in frequency conversion,[19,3] were measured by degenerate three-wave mixing[20] and time-resolved interferomery[21] at 1 μm. In this article we report on the results of the single-beam *Z*-scan measurement[12,13] of the nonlinear refractive index associated with SPM at wavelengths of 1.053 μm, 0.527 μm, and 0.351 μm and two-color *Z*-scan[22] to measure the nonlinear coefficients of XPM between 1.053 μm and 0.527 μm in a KDP crystal. In the two-color *Z*-scan measurement, two collinear beams with different wavelengths are used; a weak probe beam can be defocused by the action of the strong pump beam in a thin sample.[22] The far-field intensity variation is used to determine the optical nonlinearity from XPM as the sample is moved along the propagation direction (z axis) of the focused beams.

A schematic of the setup is shown in Fig. 74.61. Infrared (IR) laser pulses (λ_1 = 1.053 μm), second-harmonic (SH) pulses (λ_2 = 0.527 μm), or third-harmonic (TH) pulses (λ_3 = 0.351 μm) are transmitted through an aperture A1 and can be treated as top-hat beams. Second-harmonic pulses are generated using a KDP type-I crystal, and third-harmonic pulses are generated using two KDP type-II crystals.[23] We use the top-hat spatial profile because it increases the measurement sensitivity.[24] This top-hat beam then co-propagates through a lens with focal length f_1 for IR, f_2 for SH, and f_3 for TH. The focal lengths f_1, f_2, and f_3 are slightly different due to the dispersion of the lens. The electric-field distribution near the focal point $E_i(r,z,t)$ (i = 1,2,3) is described by Lommel functions.[25] It has an Airy radius at the focal spot of 1.22 $\lambda_i F_i$, where $F_i = f_i/2a$ and $2a$ is the diameter of aperture A1. The beam waist (w_{0i}) is defined as $w_{0i} = \lambda_i F_i$. The Rayleigh range (z_{0i}) is $\pi w_{0i}^2/\lambda_i$. A nonlinear crystal located in the focal region will introduce phase modulation proportional to the intensity. The single-beam *Z*-scan is performed when only one wavelength beam passes through A1. In these cases, if the sample thickness is much less than the Rayleigh range z_{0i} and the nonlinear absorption can be ignored, the field distribution at the exit surface of the sample can be expressed simply by

$$E_{ei}(r,z,t) = E_i(r,z,t)\,\exp\left\{ik_i L_{\mathrm{eff}_i}\left[\gamma_i\left|E_i(r,z,t)\right|^2\right]\right\}, \quad i = 1,2,3 \tag{1}$$

where $k_i = 2\pi/\lambda_i$, $L_{\mathrm{eff}_i} = \left[1-\exp\left(-\alpha_i L\right)\right]/\alpha_i$ is the effective sample thickness, α_i is the linear absorption coefficient, and γ_i is the nonlinear refraction coefficient, which is related to n_{2i} by $n_{2i} = \left(cn_0/40\pi\right)\gamma_i\left(m^2/\mathrm{W}\right)$, where c(m/s) is the speed of light in vacuum and n_0 is the linear index of refraction. The incident electric field $E_i(r,z,t)$ is normalized so that $I_i = \left|E_i(r,z,t)\right|^2$.

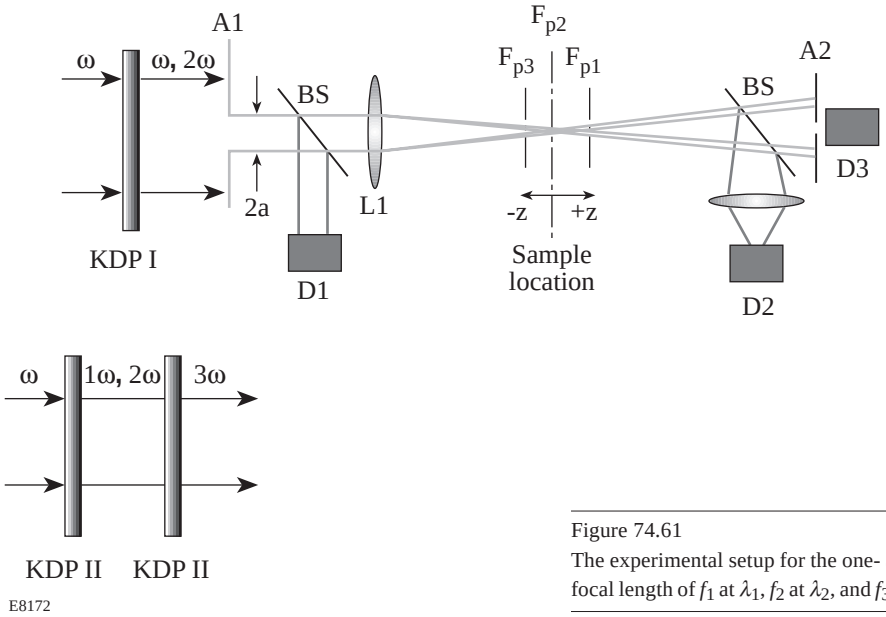

Figure 74.61
The experimental setup for the one- and two-beam *Z*-scans. A1, A2: aperture; L1: lens with focal length of f_1 at λ_1, f_2 at λ_2, and f_3 at λ_3; D1, D2, D3: photon detectors; BS: beam splitter.

In the two-color *Z*-scan, we measured the cross-phase-modulation coefficients between optical waves at λ_1 and λ_2. The output unconverted IR (pump beam) and SH pulses (probe beam) from a frequency doubler co-propagate through A1 (Fig. 74.61). The field distribution at the exit surface of the sample is

$$E_{e1}(r,z,t) = E_1(r,z,t) \exp\left\{ik_1 L_{\text{eff}_1}\left[\gamma_1 |E_1(r,z,t)|^2 + 2\gamma_{21}|E_2(r,z,t+\tau)|^2\right]\right\}, \quad (2)$$

$$E_{e2}(r,z,t+\tau) = E_2(r,z,t+\tau) \exp\left\{ik_2 L_{\text{eff}_2}\left[\gamma_2 |E_2(r,z,t+\tau)|^2 + 2\gamma_{12}|E_1(r,z,t)|^2\right]\right\}, \quad (3)$$

where τ is the time delay between IR and SH pulses introduced in the KDP type-I frequency-doubling crystal. In the exponent of Eqs. (2) and (3), the first term reflects the impact of self-phase modulation, and the second term reflects the phase modulation induced by an optical wave of the other wavelength. If the optical wave intensity at wavelength λ_2 is weak enough that $\gamma_2|E_2|^2 << \pi$, the second term in the exponential of Eq. (2) and first term in Eq. (3) can be ignored. Therefore, as the nonlinear crystal is moved along the z axis, the transmittance of the electric field at wavelength λ_1 through a finite aperture in the far field is determined by the self-phase modulation of the λ_1 optical wave, while the transmittance of the electric field at wavelength λ_2 is determined by the cross-phase modulation due to the λ_1 optical wave.

When the Fresnel number $w_{0i}/\lambda_i D$ is much smaller than unity, where D is the distance from sample to the aperture A2, the field distribution $E_{\text{A2}}(\rho,z,t)$ at the sampling aperture A2 (Fig. 74.61) is proportional to the Fourier transform of field at the exit surface of the sample.[26] The normalized *Z*-scan power transmittance is

$$T(z) = \frac{\int_{-\infty}^{\infty}\int_0^{r_a} \left|E_{\text{A2}}(\rho,z,t)\right|^2 \rho d\rho dt}{\int_{-\infty}^{\infty}\int_0^{r_a} \left|E_{i_{\text{A2}}}(\rho,z,t)\right|^2 \rho d\rho dt}, \quad (4)$$

where r_a is the radius of aperture A2 and $E_{i\text{A2}}$ is the electric field at A2 without nonlinear crystal. Equation (4) gives the *Z*-scan fluence transmittance $T(z)$ as a function of crystal position.

Figure 74.62 shows numerical examples of the normalized transmittance as a function of sample positions in the presence of SPM and XPM, respectively. For all of the curves the on-axis nonlinear phase accumulation (either self- or cross-phase) is chosen to be $\Phi_0 = 0.4$, where $\Phi_0 = k_i L_{\text{eff}_i}\gamma_i I_0$ and I_0 is the on-axis peak intensity. The curves compare the effects of self- and cross-phase modulation on the transmittance of the two beams through the aperture. Even though the phase shifts are the same, the different focusing of the two beams means that transmittance as a function of crystal position will differ for the

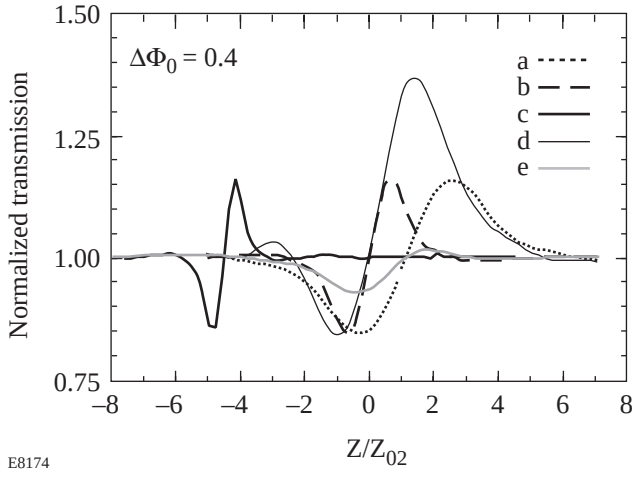

Figure 74.62
The effect of SPM and XPM on transmitting the beams at different wavelengths through the aperture (A2 in Fig. 74.61). In all cases, the nonlinear phase shift is $\Phi_0 = 0.4$. Curves (a), (b), and (c) are the transmittance of the single-color *Z*-scan at wavelengths of $\lambda_1 = 1053$ nm, $\lambda_2 = 527$ nm, and $\lambda_3 = 351$ nm. Curve (d) is the transmittance of the two-color (λ_1,λ_2) *Z*-scan with a strong λ_1 and weak λ_2. Curve (e) is the transmittance of the two-color (λ_1,λ_2) *Z*-scan for a strong λ_2 and λ_1. z/z_{02} is the position in terms of the Rayleigh range of the second-harmonic beam.

different physical processes. This can be beneficial in distinguishing the different effects, in particular, eliminating the contamination of SPM in the XPM measurements.

Curves (a), (b) and (c) in Fig. 74.62 show the effects of self-phase modulation on the transmittance for the beam at wavelengths of 1.053 μm (λ_1), 0.527 μm (λ_2), and 0.351 μm (λ_3), respectively. Since the *f* number of the system at λ_1 and λ_2 is about the same, the Rayleigh range z_{01} is twice z_{02}. The distance between peak and valley corresponding to the λ_2 optical wave is half that of the λ_1 optical wave. Curve (d) shows the effects of XPM of λ_1 on the transmittance of the weak λ_2 beam $\left(\lambda_2 = \lambda_1/2\right)$. The asymmetry in the relative decrease or increase in transmittance is mainly due to the dispersion of the focusing lens. The focal length is slightly longer for the λ_1 optical wave. The irradiance of electric field at 1.053 μm induces a positive lens for the λ_2 wave in the thin sample near its focus since $n_{21} > 0$. With the sample on the $-z$ side of the λ_1 focus (Fig. 74.61), the positive lensing effect tends to augment diffraction; therefore, the aperture transmittance is reduced. When the sample moves on the $+z$ side of the λ_1 focus, the positive lensing effect tends to collimate the beam and increase the transmittance through the aperture. The transmittance reaches a maximum when the sample is located approximately at the focal point of λ_1 (i.e, F_{p1} in Fig. 74.61) because the maximum intensity-dependent phase distortion takes place at F_{p1}. Curve (e) shows the effects of XPM of λ_2 on the transmittance of a weak λ_1 beam, which is opposite to curve (d). The asymmetry in the relative decrease or increase in transmittance is similar to curve (d) but the sensitivity is much smaller in this case. Because the pump beam's spot diameter is half that of the probe beam, only the center portion of the probe beam will experience nonlinear phase distortion.

In the experiment, 2.0-ps, 1-μm laser pulses are generated from a chirped-pulse-amplification laser system.[27] These 3-cm-diam pulses are incident on a 1-cm-thick, type-I KDP frequency-doubling crystal for cases where n_2 at 0.527 μm and a XPM coefficient between 1.052 μm and 0.527 μm were measured. These pulses are incident on two 1.6-cm-thick, type-II KDP crystals to generate TH when n_2 at 0.351 μm was measured. A half-wave plate placed before the doubler tunes the polarization of the IR to control the amount of SH or TH wave generated. A BG18 filter after doubler and UG11 filter after tripler were used respectively to block light at other wavelengths.[28] A 6.8-mm-diam aperture (A1 in Fig. 74.61) is placed after the crystal to select a small portion of the IR, SH, or TH waves. The spatial profile of the pulse passing through the aperture can be regarded as a top-hat pulse. The focal lengths of the lens after the A1 aperture were determined by a far-field spot-size scan using a CCD[29] camera. The measured focal lengths are $f_1 = 76.5 \pm 0.5$ cm at $\lambda_1 = 1.053$ μm, $f_2 = 74.3 \pm 0.5$ cm at $\lambda_2 = 0.527$ μm, and $f_3 = 65.4 \pm 0.5$ cm at $\lambda_3 = 0.351$ μm. The resulting beam waists (w_{01}, w_{02}, and w_{03}) were 118 μm, 58 μm, and 34 μm, respectively. The Rayleigh ranges (z_{01}, z_{02}, and z_{03}) were 4.2 cm, 2.0 cm, and 1.0 cm. For crystals with small n_2, a longer crystal is preferred as long as the thickness is less than one-third of the corresponding Rayleigh range. In all cases, the intensity is kept well below the damage threshold. Samples with different thicknesses and cuts were used for different wavelengths. The crystals were mounted on a translation stage. To simplify the experiment analysis, a 7.5-mm-thick KDP sample cut at 90° to the wave-propagation direction was used for measuring XPM coefficients to avoid generating additional second- and third-harmonic generation during the interaction. For other axis orientations, the **k**-vector spread due to focusing would allow part of the beam to satisfy the second- or third-harmonic phase-matching condition. The transmittance through the aperture would then be due to the combined effects from refractive index changes, second-, and third-harmonic generation.

The beam splitter after the aperture (A1 in Fig. 74.61) sends a small portion of the beam to a PIN diode[30] (D1 in Fig. 74.61),

which is used to monitor the top-hat IR energy. Part of the probe beam is reflected by the beam splitter before the analyzing aperture (A2 in Fig. 74.61) to a PIN diode (D2 in Fig. 74.61) and gives the open-aperture *Z*-scan curve. From the open-aperture scan the nonlinear absorption is measured. The change of transmission due purely to the nonlinear index of refraction is determined by dividing the closed-aperture transmittance by the one without the aperture. This has the advantage of compensating for the energy fluctuations during the experiment. The linear transmittance of aperture A2, defined as the ratio of power transmitted through A2 to the total power incident on the plane of the aperture, is 0.03. The incident IR temporal full width at half-maximum (τ_{FWHM}) was 2.0±0.2 ps as measured by a single-shot autocorrelator. The SH and TH pulse widths were calculated to be 1.41 ps and 1.45 ps, respectively, in the small-signal-gain region. The energy ε of the incident IR pulse was measured by an energy meter.[31] For a Gaussian temporal profile, the on-axis peak intensity I_0 within the sample is $I_0 = \sqrt{\pi \ln 2}\varepsilon / 2w_0^2 t_{FWHM}$.[32]

Figure 74.63 shows typical *Z*-scan results obtained to determine the SPM and XPM coefficients of KDP crystals. The parameters for each case are listed in Table 74.II. The peak-to-valley configuration of all these *Z*-scans indicates a positive nonlinearity. The solid line in each of the figures is the least squares fit to the experiment data using Eq. (3) to determine the total phase accumulation Φ_0. We use a temporal separation induced in the frequency-doubling crystal (KDP I), $\tau = 0.73$ ps in Eq. (2) in the case of XPM based on the predicted temporal walk-off between pulses at different wavelengths.[33] The extraordinary IR wave moves 0.73 ps ahead of the extraordinary SH wave at the exit of the 1-cm, KDP type-I doubler.

The nonlinear coefficient γ_2 can then be calculated from $\Phi_0 = kL_{eff}\gamma_{12}I_0$. There are several error sources in the measurement: the error in the curve fit, in measuring the crystal thickness, and in measuring the pulse width and energy that determine beam intensity. The least squares fit for the experiment data yields an error of 5%. The error for the crystal

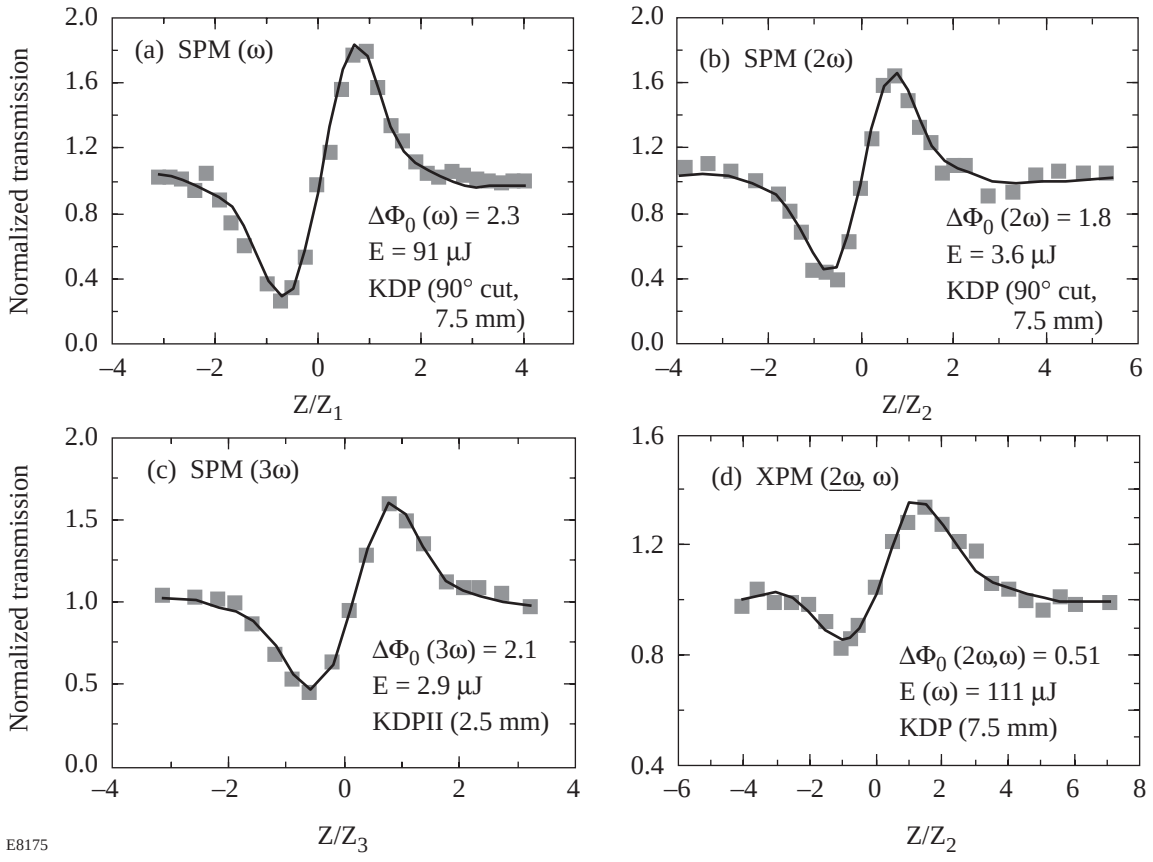

Figure 74.63
Experimental one- and two-beam *Z*-scans as a function of z/z_{0i}, $i = 1,2,3$. In all cases, the solid line is fit to determine the peak phase shift Φ_0. (a) Single beam, $\lambda_1 = 1.053$ μm, $\Phi_0 = 2.3$; (b) single beam, $\lambda_2 = 0.527$ μm, $\Phi_0 = 1.8$; (c) single beam, $\lambda_1 = 0.351$ μm, $\Phi_0 = 2.1$; and (d) two-color (λ_1,λ_2) beams, $\Phi_0 = 0.51$.

thickness is 1%. The errors for the beam waist coming from the measurement of focal length and diameter of the aperture are 1.6%. The largest error comes from measuring the IR pulse width and beam energy. The pulse widths of SH and TH were calculated based on the measurement of the IR pulse. The resultant error of the on-axis intensity is 12% for IR, 15% for SH, and 18% for UV. The nonlinear coefficients of SPM and XPM with different polarizations were measured, with the results presented in Table 74.III. Both n_2 and γ, which are related through the index of refraction, are presented. Our results for the nonlinear coefficient at 1.053-μm wavelength are in good agreement with the work reported in Refs. 20 and 21, which is shown in the last two columns of Table 74.III. To our knowledge, the nonlinear SPM coefficients at wavelengths of 0.527 μm, and 0.351 μm, and the XPM coefficient between 1.053 μm and 0.527 μm, are the first data set reported for KDP.

In the two-color *Z*-scan, there is a further temporal walk-off between the two colors with different wavelengths in the KDP sample. To measure n_2(*o*-*o*), in which both the probe and the pump beams are ordinary waves, the optical axis of the sample KDP (90° cut) is perpendicular to the polarization of IR and SH pulses. Both the pump and probe beams are *o*-waves in the sample, and the pump pulse (IR) moves 0.51 ps ahead of the probe pulse (SH) after the sample. For measuring n_2(*e*-*e*), both the pump (IR) and probe beams (SH) are *e*-waves in the sample, and the pump pulse moves 0.59 ps ahead of the probe pulse in the sample crystal. We include the walk-off effects in the theoretical fit by dividing the sample into segments and integrating the nonlinear phase experienced in each of the pieces. In each of the segments, the probe beam will experience a different nonlinear phase shift, which is due to the different time delay between the pump and probe; thus, the XPM can be

Table 74.II: The parameters of *Z*-scans for measuring SPM and XPM in KDP and the resultant phase shift Φ_0.

	λ (μm)	Pulse width (ps)	Energy (μJ)	Φ_0
(a)	1.053 (*e*) (SPM)	2.0	91±5	2.3±0.1
(b)	0.527 (*o*) (SPM)	1.41	3.6±0.4	1.8±0.1
(c)	0.351 (*o*) (SPM)	1.45	2.9±0.4	2.1±0.1
(d)	1.053 (*e*), 0.527 (*e*) (XPM) (pump) (probe)	2.0 (IR) 1.41 (SH)	111±7 (IR) <0.2 (SH)	0.51±0.04

Table 74.III: Measured values of n_2 and γ for KDP at 1.053 μm, 0.527 μm, and 0.351 μm for SPM and cross-phase coefficients between 0.527 μm and 1.053 μm. Also shown are results of previous work from Refs. 20 and 21.

	$n_2(10^{-13}$ esu)	$\gamma(10^{-16}$ cm^2/W)	$n_2(10^{-13}$ esu) other work	$\gamma(10^{-16}$ cm^2/W) other work
1.053 μm (*o*)	0.8±0.2	2.3±0.5	0.72[20]	2.9±0.9[21]
(*e*)	0.88±0.2	2.5±0.5	0.78,[20] 1.0±0.3[21]	
0.527 μm (*o*)	1.4±0.4	4.0±1.0		
	1.3±0.3	3.5±0.9		
0.351 μm (*o*)	2.4±0.7	7.0±2.0		
(*e*)	1.2±0.4	3.0±1.0		
0.527 (*e*); 1.053 (*e*) (weak; strong)	0.03±0.01	0.10±0.03		
0.527 (*o*); 1.053 (*o*) (weak; strong)	0.023±0.007	0.06±0.02		

well determined. We could improve the sensitivity of our measurement by putting a predelay crystal[34] before or after the frequency-doubling crystal to compensate for the walk-off introduced in the measured sample.

In conclusion, a top-hat *Z*-scan method was used to measure the phase shift caused by the self- and cross-phase nonlinearity in KDP crystals. The third-order nonlinear coefficient of KDP at different polarizations at wavelengths of 1.053 μm, 0.527 μm, and 0.351 μm was obtained. By considering the temporal walk-off between the pump and probe beams in the crystals, we are also able to estimate the nonlinear index of refraction due to the cross-phase modulation.

ACKNOWLEDGMENT

We thank R. Boni for providing several crystals, R. S. Craxton for performing pulse-width calculations, and both for many helpful discussions. This study was supported by the U.S. Department of Energy Office of Inertial Confinement Fusion under Cooperative Agreement No. DE-FC03-92SF19460, the University of Rochester, and the New York State Energy Research and Development Authority. The support of DOE does not constitute an endorsement by DOE of the views expressed in this article.

REFERENCES

1. W. L. Kruer, *The Physics of Laser Plasma Interactions*, Frontiers in Physics, Vol. 73, edited by D. Pines (Addison-Wesley, Redwood City, CA, 1988), Chap. 5.
2. J. C. Kieffer, P. Audebert, M. Chaker, J. P. Matte, H. Pépin, T. W. Johnston, P. Maine, D. Meyerhofer, J. Delettrez, D. Strickland, P. Bado, and G. Mourou, Phys. Rev. Lett. **62**, 760 (1989).
3. C. Y. Chien, G. Korn, J. S. Coe, J. Squier, G. Mourou, and R. S. Craxton, Opt. Lett. **20**, 353 (1995).
4. R. W. Boyd, *Nonlinear Optics* (Academic Press, Boston, 1992).
5. G. P. Agrawal, *Nonlinear Fiber Optics* (Academic Press, Boston, 1989).
6. K. J. Blow, N. J. Doran, and B. P. Nelson, Opt. Lett. **10**, 393 (1985).
7. M. N. Islam, L. F. Mollenauer, and R. H. Stolen, in *Ultrafast Phenomena V*, edited by G. R. Fleming and A. E. Siegman, Springer Series in Chemical Physics (Springer-Verlag, Berlin, 1986), pp. 46–50.
8. J. D. Kafka and T. Baer, Opt. Lett. **12**, 181 (1987).
9. R. H. Stolen and J. E. Bjorkholm, IEEE J. Quantum Electron. **QE-18**, 1062 (1982).
10. R. R. Alfano *et al.*, Phys. Rev. A **35**, 459 (1987).
11. L. Zheng, R. S. Craxton, and D. D. Meyerhofer, in *Conference on Lasers and Electro-Optics*, Vol. 15, 1995 OSA Technical Digest Series (Optical Society of America, Washington, DC, 1995), pp. 131–132; L. Zheng, "Third-Harmonic Generation of Intense Laser Pulses," Ph.D. thesis, University of Rochester, 1997.
12. M. Sheik-bahae, A. A. Said, and E. W. Van Stryland, Opt. Lett. **14**, 955 (1989).
13. M. Sheik-bahae *et al.*, IEEE J. Quantum Electron. **26**, 760 (1990).
14. S. R. Friberg and P. W. Smith, IEEE J. Quantum Electron. **QE-23**, 2089 (1987).
15. Y.-H. Chuang, Z. W. Li, D. D. Meyerhofer, and A. Schmid, Opt. Lett. **16**, 7 (1991).
16. A. Owyoung, IEEE J. Quantum Electron. **QE-9**, 1064 (1973).
17. M. J. Weber, D. Milam, and W. L. Smith, Opt. Eng. **17**, 463 (1978).
18. M. J. Moran, C.-Y. She, and R. L. Carman, IEEE J. Quantum Electron. **QE-11**, 259 (1975).
19. W. Seka, J. M. Soures, S. D. Jacobs, L. D. Lund, and R. S. Craxton, IEEE J. Quantum Electron. **QE-17**, 1689 (1981).
20. R. Adair, L. L. Chase, and S. A. Payne, Phys. Rev. B **39**, 3337 (1989).
21. D. Milam and M. J. Weber, J. Appl. Phys. **47**, 2497 (1976).
22. M. Sheik-Bahae *et al.*, Opt. Lett. **17**, 258 (1992).
23. R. S. Craxton, IEEE J. Quantum Electron. **QE-17**, 1771 (1981).
24. W. Zhao and P. Palffy-Muhoray, Appl. Phys. Lett. **63**, 1613 (1993).
25. M. Born and E. Wolf, *Principles of Optics: Electromagnetic Theory of Propagation, Interference and Diffraction of Light*, 6th ed. (Pergamon Press, Oxford, 1980), p. 435.
26. J. D. Gaskill, *Linear Systems, Fourier Transforms, and Optics* (Wiley, New York, 1978).
27. Y.-H. Chuang, D. D. Meyerhofer, S. Augst, H. Chen, J. Peatross, and S. Uchida, J. Opt. Soc. Am. B **8**, 1226 (1991).
28. Optical Glass Filters, Scott Glass Technologies, Inc., Duryea, PA 18642.
29. Model GP-MF 702, Panasonic, Secaucus, NJ 07094.
30. PIN 10D 4303, UDT Sensors, Inc., Hawthorne, CA 90250.
31. JD 1000 Joulemeter, Molectron Detector, Inc., Portland, OR 97224.
32. A. E. Siegman, *Lasers* (University Science Books, Mill Valley, CA, 1986).
33. Y. Wang and R. Dragila, Phys. Rev. A **41**, 5645 (1990).
34. Y. Wang, B. Luther-Davis, Y.-H. Chuang, R. S. Craxton, and D. D. Meyerhofer, Opt. Lett. **16**, 1862 (1991).

Micromechanics of Material-Removal Mechanisms from Brittle Surfaces: Subsurface Damage and Surface Microroughness

The cold processing of optical glasses usually involves rough grinding, microgrinding, and polishing. In microgrinding,[1,2] the resulting brittle-material-removal rate produces a cracked layer near the glass surface, referred to as subsurface damage (SSD). [Editor's note: The acronym for subsurface damage (SSD) used in this article should not be confused with its more common use as an acronym for smoothing by spectral dispersion.] Of course, the optical quality as well as the strength of the resulting surface is affected by such subsurface damage, so there is the need to understand the generation of subsurface damage as well as its measurement. Preston[3] was the first to observe that the damaged layer usually increases in proportion to the surface microroughness (SR). Preston measured a proportionality factor of 3 to 4, which seemed to be independent of the grinding conditions. We emphasize that subsurface damage is a statistical measure of the ground surface rather than a reflection of the deepest flaw that might control, say, the mechanical strength of the surface.

The direct measurement of SSD is tedious; therefore, fast and reliable techniques to measure subsurface damage are necessary: The dimple method, which is often used,[4,5] relies on the observation that a sufficiently deep spherical impression produced on the damaged optical surface must penetrate into and past the damaged layer. Wafering methods may also be used. The fact that SSD scales with SR was later confirmed, for example, by Aleinikov,[6] who showed that SSD induced by lapping of glasses and other brittle ceramics (with hardness changing 30-fold, fracture toughness 6-fold, and Young's modulus 20-fold) was 3.9±0.2 times SR for SiC abrasives (100 to 150 μm). This observation indicates that SSD may be estimated from SR, whose measurement is significantly simpler and less time consuming. Aleinikov also found that SSD increased with increasing size of microindentation cracks. Aleinikov's correlations between indentation crack length, subsurface damage, and surface roughness are summarized in Fig. 74.64.

Since the Preston[3] and Aleinikov[6] work showed the scaling of SSD with SR under loose-abrasive grinding conditions, it is interesting to extend their observations to bound-abrasive grinding. This issue was more recently examined by Edwards and Hed,[8] who studied the relation of SSD to SR under bound-diamond-abrasive conditions (53 to 65 μm and 180 to 250 μm in size). Edwards and Hed found that for the three glasses they studied (borosilicate crown BK7, zerodur, and fused silica) the average SSD exceeded the proportionality factor of about 4 found under loose-abrasive conditions: Specifically, they found that the average SSD was 6.4±1.3 times the peak-to-valley (p–v) surface roughness (as measured by a profilometer). The factor of 6.4 was arrived at by dividing SSD by SR for each glass. On the other hand, this proportionality factor becomes identical to that of Aleinikov when all three materials tested by Edwards and Hed are treated together (see Fig. 74.65). Similar observations have been reported for deterministic microgrinding of optical glasses with bound-abrasive-diamond tools of smaller size (2 to 4 μm to 70 to 80 μm) (see Lambropoulos *et al.*[9,10]).

In this article, we describe measurements of subsurface damage and surface roughness resulting from microgrinding optical glasses with metal-bonded diamond-abrasive ring tools and present a model for interpreting such data.

Experiments

To study the relation between surface microroughness (SR) and subsurface damage (SSD) in optical glasses, we selected eight glasses that are often used in optical design. The glasses included fused silica (Corning 7940), the borosilicate crown glass BK7, the crown glass K7, the lanthanum crown glass LaK9, the PbO containing dense flint glasses (SF7, SF58), the flint glass F7, the short (kurz) flint glass KzF6, and the dense tantalum flint glass TaFD5.

1. Glass Mechanical Properties

Glasses, like other brittle materials, are characterized by their hardness and fracture toughness.[11,12] Hardness was determined in air via the usual Vickers indentation method with loads ranging from 10 gf to 1 kgf. Fracture toughness was also determined from microindentation, via the model of Evans,[13] which, as we had previously shown,[9] is in good agreement with

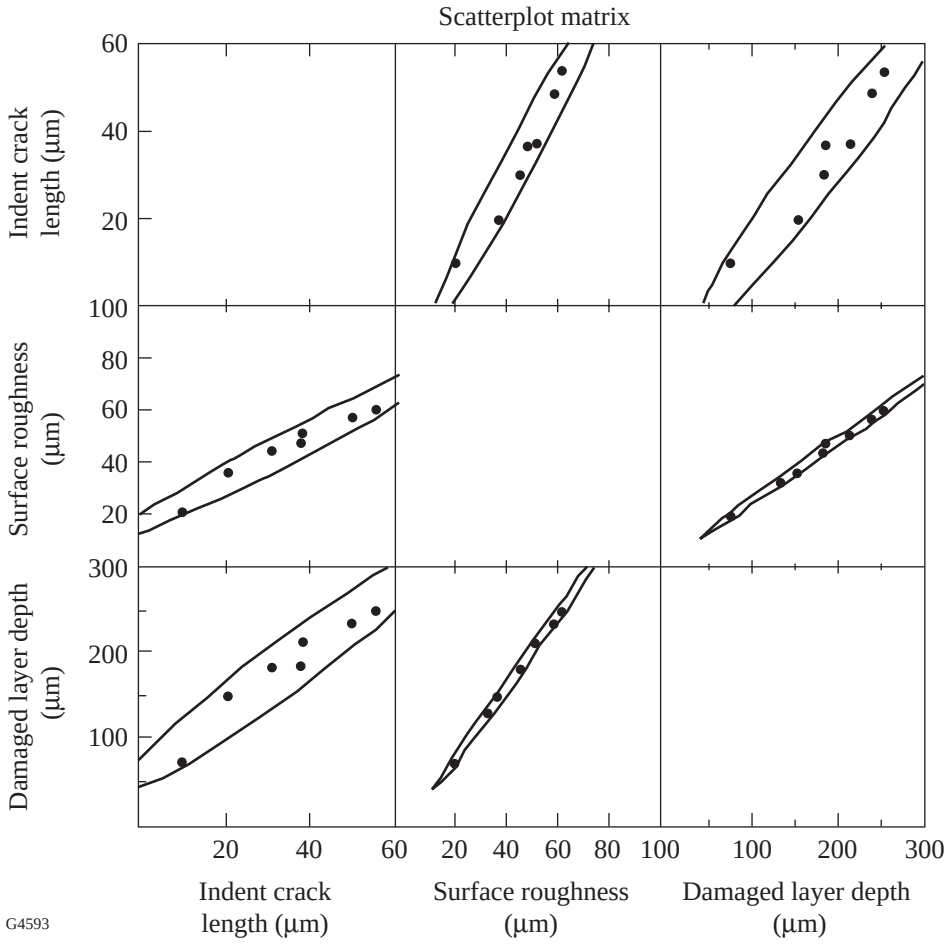

Figure 74.64
Correlations of indentation crack size, surface roughness, and subsurface damage under loose-abrasive conditions. Data are from Aleinikov.[6] Equivalents to Russian glasses can be found in Ref. 7. The individual brittle materials studied by Aleinikov are indicated in the work by Lambropoulos *et al.*[10]

the measurement of fracture toughness via bulk methods. Evans[13] used dimensional analysis and curve fitting over a range of $c/(D/2)$ from 1.5 to 7 and proposed

$$K_c = H\sqrt{D/2}\left(\frac{\mathrm{E}}{H}\right)^{0.4} 10^{f(x)}, \quad x = \log_{10}\left(\frac{c}{D/2}\right),$$
$$f(x) = -1.59 - 0.34x - 2.02x^2 + 11.23x^3 - 24.97x^4 + 16.32x^5, \tag{1}$$

where K_c is fracture toughness, H hardness (Vickers), D indentation diagonal, E Young's modulus, and c the half-crack size. Microindentation of densifying glasses, such as fused silica, cannot be analyzed in this manner.[14–16]

In our notation, H denotes hardness, or resistance to plastic, irreversible deformation, measured by estimating the area of an indentation impressed under load P. Hardness is defined in terms of either projected area or actual area of contact.

Specifically, H_K denotes Knoop hardness, extracted from measuring the long diagonal of a rhomboidal pyramid impression under load P by P/(projected contact area) = (constant) P/(long diagonal)^2, with the (constant) dependent on the rhomboidal pyramid geometry.

H_V denotes Vickers indentation, extracted from measuring the average diagonal of a square pyramid impression under load P by P/(actual contact area) = (constant) P/(average diagonal)^2, with the (constant) dependent on the square pyramid geometry.

For the same measured diagonal, Knoop indentations penetrate about half as much into the surface as Vickers indentations; thus, H_K more closely measures near-surface hardness. Generally, Knoop hardness H_K increases with Vickers hardness H_V. This correlation has been described in detail by Lambropoulos *et al.*[9]

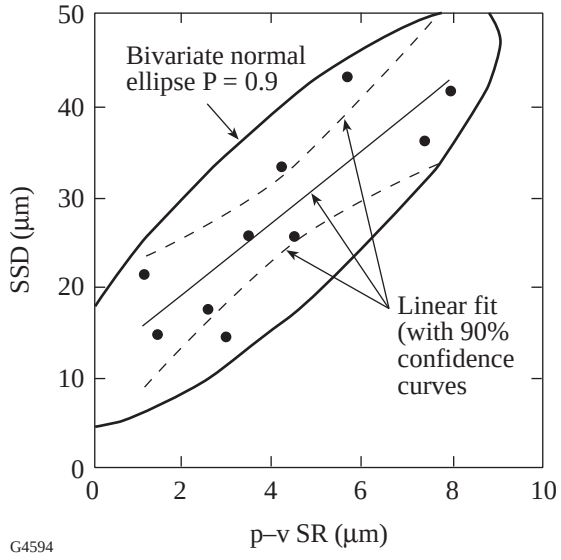

Figure 74.65
Relation of subsurface damage (SSD) to surface roughness (SR), measured in bound-diamond-abrasive grinding by Edwards and Hed.[8] Shown are the bivariate ellipse (at P = 90%, with aspect ratio of about 3.8) and the confidence curves at the level of 90% (dashed line). The straight line fit has a slope of 4.0±0.9 and an intercept of 11±4.

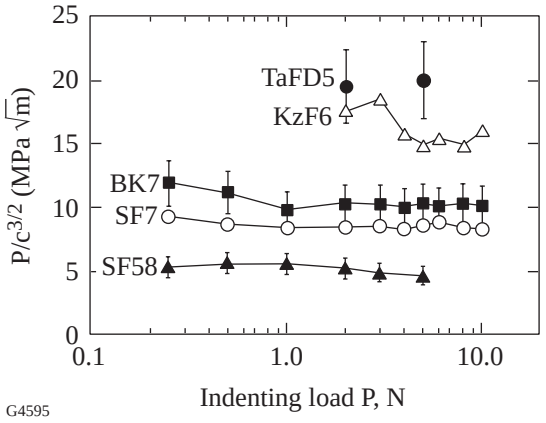

Figure 74.66
Correlation of the measured indentation crack length c (tip-to-tip surface trace length is 2c) with applied load P shows essentially a constant value of the ratio $P/c^{3/2}$.

Figure 74.66 shows the measured values of $P/c^{3/2}$ versus the applied load P for some of our tested glasses, indicating that this ratio is essentially constant over the indenting loads used. Table 74.IV shows the glass thermomechanical properties. Data for density ρ, glass transition temperature T_g, coefficient of thermal expansion α, Young's modulus E, and Poisson ratio ν are from manufacturers' catalogs. Knoop hardness H_K and Vickers hardness H_V are at 1.96 N. K_c for fused silica was taken from the Corning catalog. H_V and K_c data of LaK9 were estimated from that of neighboring glasses LaK10, LaK11.[9,17] Data in Table 74.IV other than Vickers hardness have been reported previously.[10]

2. Deterministic Microgrinding Experiments

The surface-grinding experiments were done on a deterministic microgrinding platform, where infeed rate is imposed, thus resulting in surfaces of minimal figure errors, superior finish, and minimal damage. Imposing infeed rate leads to precise knowledge of the amount of removed material when microgrinding optical glasses. In the platform used, both the tool and work axis spin. The variable angle between these axes of rotation can be used to produce spherical surfaces of variable radius of curvature (from 5 mm to planar surfaces).

Table 74.IV: Thermomechanical properties of optical glasses.

Glass	ρ g/cm^3	T_g °C	α $10^{-6\circ}$ C^{-1}	E GPa	ν	H_K GPa	H_V GPa	K_c MPa $\sqrt{m}$
FS-C7940	2.20	1,090	0.52	73	0.17	5.6	8.5	0.75
SF58	5.51	422	9.0	52	0.26	2.7	3.5	0.46
SF7	3.80	448	7.9	56	0.23	3.4	5.3	0.67
BK7	2.51	559	7.1	81	0.21	5.1	7.2	0.82
K7	2.53	513	8.4	69	0.21	4.6	6.2	0.95
KzF6	2.54	444	5.5	52	0.21	3.7	5.5	1.03
LaK9	3.51	650	6.3	110	0.29	5.7	(5.5)	(0.95)
TaFD5	4.92	670	7.9	126	0.30	7.3	10.0	1.54

Pollicove and Moore have described progress in fabrication of precision optical components via deterministic microgrinding with rigid, computer-controlled machining centers and high-speed tool spindles.[18,19] Deterministic microgrinding has been used to manufacture convex and concave spherical surfaces, as well as aspheres. Specular surfaces, resulting after less than 5 min of deterministic microgrinding, have typical rms microroughness of less than 20 nm, 1 μm of subsurface damage, and a surface figure better than 1/2 wave peak-to-valley. Typical infeed rates are 5 to 10 μm/min with 2- to 4-μm bound-abrasive-diamond tools.

Three metal-bonded diamond-abrasive ring tools were sequentially used on each surface (aqueous coolant Loh K-40, relative speed of work and tool of about 30 m/s): 70 to 80 μm, 10 to 20 μm, and 2 to 4 μm at infeed rates of 1 mm/min, 50 μm/min, and 5 μm/min, respectively. Three cuts were done with each tool, all at a tool speed of about 30 m/s (tool rotation of 11,250 rpm, work rotation of 150 rpm).

After each cut, the surface roughness (SR) at three locations on the optical surface was measured using the Zygo New View 100 white-light interferometer (20× Mirau), a 3-D imaging surface structure analyzer. It uses coherence-scanning white-light interferometry for noncontact imaging and measurement of surface microstructure and topography. One portion of a light beam reflects from a test surface and the other portion from an internal high-quality reference surface. Both portions are then directed onto a solid-state camera with 320 × 240 pixels. Interference between the two light-wave fronts results in an image of light and dark interference fringes, indicating the surface structure of the test part. The test part is scanned by vertically moving the objective with a piezoelectric transducer. As the objective scans, a video system captures intensities at each camera pixel. Lateral resolution is determined by the microscope objective field of view and the number of pixels and is ultimately limited by the wavelength of the light source. With a 20× objective, the field of view is 0.35×0.26 mm^2.

Subsurface damage (SSD) was measured with the dimple method,[4,5] in which a steel ball is gently ground with fine diamond paste (0.25 μm) onto the optical surface, thus penetrating into and past the SSD zone. Optical measurement of the image reveals an outer ring of SSD surrounding an inner circle of damage-free surface. Measurement of the ring radii and knowledge of the steel sphere radius lead to the extraction of the SSD. Three dimples were done for each cut for the 2- to 4- and 10- to 20-μm tools. Because of the time required to produce dimples into and past the SSD of the surfaces ground with the 70 to 80 abrasives, no SSD measurements were done on these surfaces. Figures 74.67 and 74.68 summarize the roughness and subsurface damage measurements.

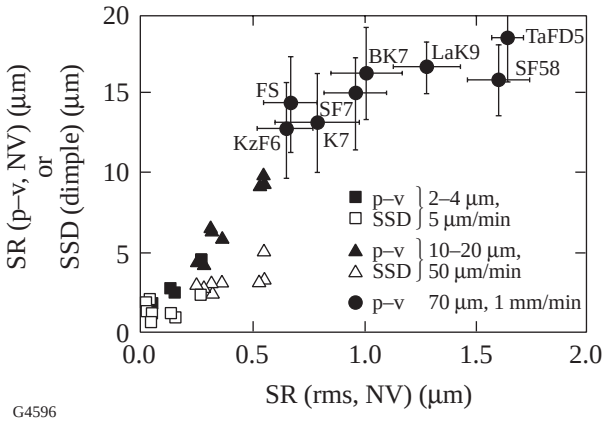

Figure 74.67
Summary of the measurements of peak-to-valley and rms surface roughness (SR) resulting from all three grinding tools used. Surface roughness was measured via the New View white-light interferometer, and subsurface damage (SSD) via the dimple method.

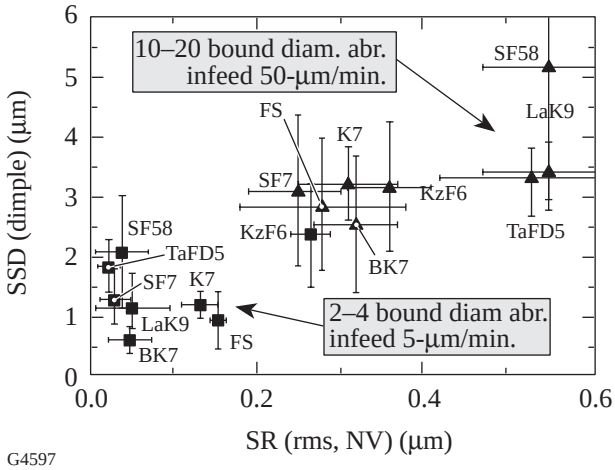

Figure 74.68
Summary of measurements for the rms surface roughness (SR) (white-light interferometry) and subsurface damage (SSD) (dimple method) for the deterministically microground surfaces with the 2- to 4-μm and 10- to 20-μm abrasives. A straight line correlation of all data has a slope of 5.5±0.9 and $R^2 = 0.73$.

Model for Ratio of Subsurface Damage to Surface Roughness

When a sharp indenter transmits normal load P into a brittle surface, the resulting indentation diagonal D is determined by the force P, the material hardness, and the sharpness of the indenting surface:

$$H = \frac{2P\sin\psi}{D^2} \tag{2}$$

with hardness defined via contact area between the indenter and the material (Fig. 74.69). Indentation mechanics can be simplified by considering the displaced material as occupying the volume of an equivalent half-sphere of radius a. Equating the volume displaced under the actual indenter (diagonal D) with that of the equivalent half-sphere volume $2\pi a^3/3$, we find

$$\frac{a}{D} = \left[\frac{3}{24\pi\sqrt{2}}\right]^{1/3}(\cot\psi)^{1/3} = 0.304(\cot\psi)^{1/3}. \tag{3}$$

Indentation induces a larger zone of plastically deformed material, approximately hemispherical with radius b. Length scales a (radius of indented half-sphere) and b (plastic zone size) can be correlated via the Hill model of the expanding cavity in a perfectly plastic material, discussed by Chiang *et al*.[20] This relation is further simplified to[20,21]

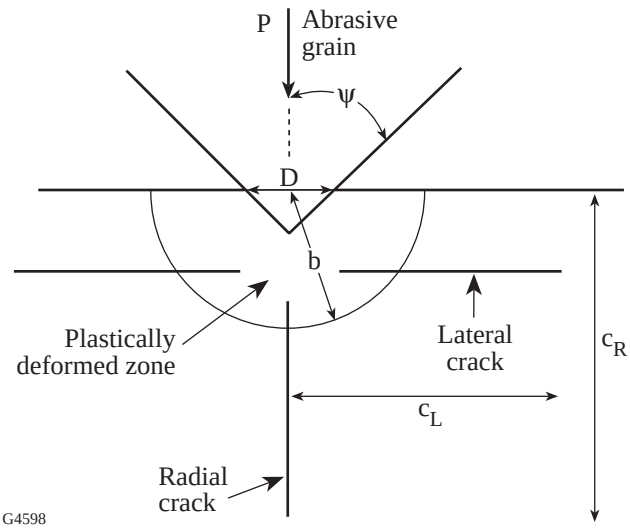

Figure 74.69
Schematic of sharp indentation shows indentation diagonal D, plastic zone size b, lateral and radial crack lengths c_L and c_R. Volume displaced by the indenter is equivalent to half-sphere of radius a.

$$\frac{b}{a} = \left(\frac{E}{H}\right)^m, \tag{4}$$

where m is a dimensionless constant in the range $m = 1/3$ to 1/2. The more traditional approach in the fracture literature uses $m = 1/2$.[22–24] More recent data analysis suggests that $m = 1/3$ may be more appropriate.[25]

When the load P exceeds some threshold value, surface cracks appear.[21] The length c_R of radial cracks emanating from the indentation is related to fracture toughness K_c and load P by[22–25]

$$K_c = \alpha_K\left(\frac{E}{H}\right)^{1-m}(\cot\psi)^{2/3}\frac{P}{c_R^{3/2}}. \tag{5}$$

α_K is a dimensionless number, found from indentation data of Fig. 74.66 for the three glasses TaFD5 (high fracture toughness K_c), BK7 (intermediate K_c), and SF58 (low K_c). We fitted Eq. (5) to the measured fracture toughness K_c for $m = 1/2$ and $m = 1/3$, and found

$$\alpha_K(m) = 0.027 + 0.090\left(m - \frac{1}{3}\right). \tag{6}$$

Fracture mechanics analysis of microindentation shows that the residual stress field is tensile at the boundary of the elastic and plastic zones at the symmetry axis of the indentation, where any lateral cracking is expected to originate.[21,26] As lateral cracks remove material from the surface, we assume that the resulting SR is equal to the plastic zone depth b, following Buijs and Korpel–Van Houten.[27,28] Other assumptions may also be made, as by Lambropoulos *et al*.[29] Such assumptions have been compared and discussed by Lambropoulos.[30] We also assume that the depth SSD of the subsurface damage zone is equal to the depth of the radial cracks c_R; thus, the ratio of SSD to SR is

$$\frac{\text{SSD}}{\text{SR}} = \frac{c_R}{b} = 2.326\,\alpha_K^{2/3}\left(\frac{E}{H}\right)^{(2-5m)/3}$$

$$\frac{(\cot\psi)^{1/9}}{(\sin\psi)^{1/2}}\left[\frac{P}{\left(K_c^4/H^3\right)}\right]^{1/6}. \tag{7}$$

Indenting load P naturally scales with the material length scale K_c^4/H^3, as has been observed previously by Lawn,[31,32] Chiang *et al*.,[21] and Marshall *et al*.[26] The dependence of the ratio SSD/SR on the actual load P is rather weak (power of 1/6), which explains the experimental fact that over a wide range of abrasives, speeds, and pressures used there seems to be a constant ratio of SSD to SR (for example, Refs. 6 and 8).

Figure 74.70 shows the dependence of the SSD/SR on load P and sharpness angle ψ. For sharp abrasives ($\psi \to 0$), the ratio SSD/SR $\to \infty$, whereas for flat abrasives $(\psi \to \pi/2)$, SSD/SR $\to 0$. Figure 74.71 shows that by using typical material properties for optical glasses, intermediate values of ψ(20° to 80°), and typical indenting loads from 0.1 to 10 N, the ratio SSD/SR is in the range 4±2. Our range of indenting loads includes loads estimated to occur under lapping conditions. Chauhan *et al*.[33] estimated the maximum transmitted force to vary from 1.2 to 4.1 N as lapping abrasives ranged in size from 10 to 65 μm.

Guided by the model predictions for the dependence of ratio SSD/SR on glass mechanical properties, we have plotted in Fig. 74.72 the measured ratio SSD/SR versus the factor K_c^4/H^3 for grinding with the 10 to 20 abrasives under deterministic micro-grinding conditions (data from Fig. 74.68). Plotted in this manner, the experimental data show a dependence on K_c^4/H^3 like a power of –0.15±0.08, which is in general agreement with the model predictions of a power of –0.167. Of course, such a comparison is valid only as long as the force transmitted by the bonded abrasive grains is essentially constant among the various ground glasses.

The model discussed above also allows us to address the question: Under what circumstances can the depth of subsurface damage actually be less than the surface roughness? Such a condition would essentially mean that no subsurface damage would be present in the ground surface, thus resembling a condition of ductile grinding or polishing. Requiring that ratio SSD/SR < 1 leads to

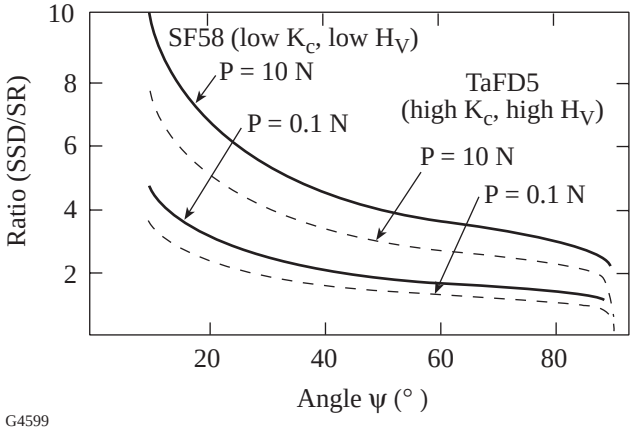

Figure 74.70
Ratio SSD/SR versus sharpness angle ψ for properties corresponding to glasses TaFD5 (hard, tough) and SF58 (soft, brittle). Indenting forces 0.1 or 10 N; factor $m = 0.40$.

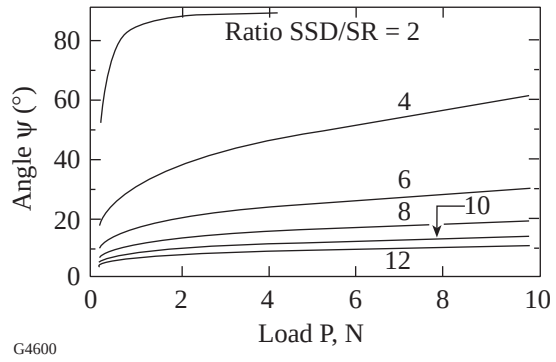

Figure 74.71
Ratio SSD/SR versus sharpness angle ψ and load P for typical optical glass (BK7). Factor $m = 0.40$.

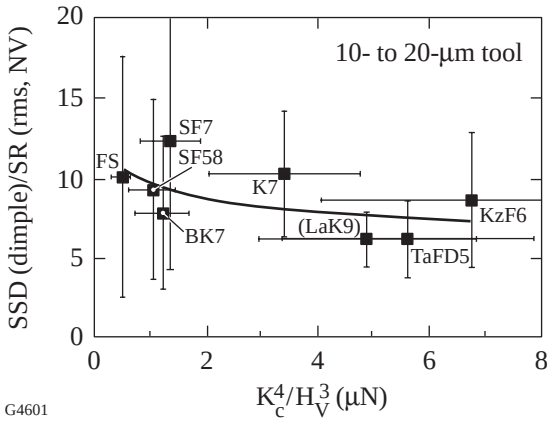

Figure 74.72
Measured ratio of subsurface damage (dimple method) to rms surface roughness (interferometry) versus the material-dependent load K_c^4/H^3 for the surfaces ground with the 10- to 20-μm metal-bonded diamond-abrasive tools. Hardness is H_V at 1.96 N. Datum for LaK9 is in parentheses since its K_c and H_V were estimated from neighboring glasses LaK10 and LaK11.

$$\frac{\mathrm{SSD}}{\mathrm{SR}} < 1 \Rightarrow P < \frac{\left(K_c^4/H^3\right)}{(2.326)^6\ \alpha_K^4 \left(\dfrac{\mathrm{E}}{H}\right)^{2(2-5m)}} \frac{(\sin\psi)^3}{(\cot\psi)^{2/3}}. \quad (8)$$

This result reveals that in order to promote more polishing-like conditions, the right-hand side of the above inequality must be made as large as possible to accommodate as large as possible a range of indenting forces P. Noticing that the dependence on the ratio (E/H) is rather weak (since m is in the range from 1/3 to 1/2), the polishing-like conditions can be achieved by a large value of the material-dependent load scale K_c^4/H^3, or by a large value of the angular factor $(\sin\psi)^3/(\cot\psi)^{2/3}$. This factor is a monotonically increasing function of the abrasive sharpness ψ; thus, polishing-like conditions are promoted by high fracture toughness K_c, low hardness H, and relatively flat abrasives contacting the manufactured optical surface. These effects are in addition to the chemical effects identified by Cook.[34] Notice, however, that other mechanical effects in polishing have been identified, both for polishing with traditional methods such as polyurethane pads[35,36] and for more recent polishing platforms that take advantage of subaperture material removal under computer–numerically controlled algorithms where the polishing slurry is a mixture of abrasive particles with a magnetorheological fluid, as discussed by Jacobs *et al.*[37] and interpreted by Lambropoulos *et al.*[38]

Figure 74.67 shows that for those instances where both the p–v roughness and the subsurface damage (SSD) were measured, the p–v roughness was an upper bound to the subsurface damage. For the finer 2- to 4-μm bonded diamond abrasives, the measured p–v roughness is a good approximation to the actual SSD. For the intermediate 10- to 20-μm abrasives, the p–v roughness is a close upper approximation to the SSD. The reason is that the dimple method reveals a statistical measure of subsurface damage, without being able to identify the deepest flaw. On the other hand, the p–v roughness is dictated by the single deepest flaw detected within the measured area. Thus, we expect that the p–v roughness would exceed the SSD measurement by the dimple method, as indeed our measurements indicate. The usefulness of this observation becomes clear from the fact that, when the subsurface damage from a very rough ground surface is to be determined, the dimple method must produce a dimple into and past the damaged zone. This would be a very time-consuming and labor-intensive task for deep SSD, while requiring only a few minutes when subsurface damage is only a few microns in depth.

Conclusions

We have presented a micromechanics model based on the sharp indentation of a brittle surface to interpret the measured ratio of subsurface damage (SSD) to surface microroughness (SR). The measurements were done under deterministic microgrinding conditions where the imposed infeed rate produces surfaces with minimal figure error, and optimum surface roughness and subsurface damage. The glasses ground span a wide range of optical glasses.

We used 70- to 80-μm, 10- to 20-μm, and 2- to 4-μm abrasives at infeeds of 1 mm/min, 50 μm/min, and 5 μm/min, respectively. For the 70- to 80-μm abrasives, the rms SR, measured with white-light interferometry, ranges from 0.65 to 1.6 μm and the p–v roughness from 12 to 19 μm. For the 10- to 20-μm abrasives, rms SR ranges from 0.25 to 0.55 μm, p–v from 4 to 10 μm, and the SSD (measured with the dimple method) from 2.5 to 5.1 μm. For the 2- to 4-μm abrasives, rms SR ranges from 0.02 to 0.27 μm, p–v from 1.3 to 4.4 μm, and the SSD (measured with the dimple method) from 0.90 to 2.3 μm.

These measurements support the conclusion that peak-to-valley surface roughness measured by interferometry provides an upper bound to the subsurface damage measured via the dimple method. This observation is useful, and its applicability should be further explored for a wider range of optical materials under a large range of manufacturing processing conditions.

The micromechanics model predicts the ratio of SSD/SR in terms of the load transmitted by the abrasive grain, the sharpness of the abrasive, and the glass mechanical properties (Young's modulus E, hardness H, fracture toughness K_c). The dependence on load is rather weak, in agreement with our measurements and others. The effect of abrasive sharpness is more pronounced. In the limit of SSD/SR < 1, i.e., when polishing-like or ductile grinding conditions prevail, no SSD can be identified because it is enveloped within the surface microroughness. Such conditions are promoted for brittle materials with high fracture toughness and low hardness. Flat abrasive grains have the same effect.

ACKNOWLEDGMENT

We acknowledge many helpful discussions with and insights from Mr. Don Golini of QED Technologies, LLC (Rochester, NY) and with Profs Paul Funkenbusch, Stephen Burns, and James C. M. Li of the Mechanical Engineering Department at the University of Rochester.

REFERENCES

1. T. S. Izumitani, *Optical Glass*, American Institute of Physics Translation Series (American Institute of Physics, New York, 1986), Chap. 4, pp. 91–146.
2. H. H. Karow, *Fabrication Methods for Precision Optics* (Wiley, New York, 1993), Chap. 5.
3. F. W. Preston, Trans. Opt. Soc. **XXIII**, 141 (1921–22).
4. A. Lindquist, S. D. Jacobs, and A. Feltz, in *Science of Optical Finishing*, 1990 Technical Digest Series (Optical Society of America, Washington, DC, 1990), Vol. 9, pp. 57–60.
5. Y. Zhou *et al.*, J. Am. Ceram. Soc. **77**, 3277 (1994).
6. F. K. Aleinikov, Sov. Phys. Tech. Phys. **27**, 2529 (1957).
7. L. B. Glebov and M. N. Tolstoi, in *CRC Handbook of Laser Science and Technology*, Vol. V: Optical Materials, Part 3, Supplement 2: Optical Materials, edited by M. J. Weber (CRC Press, Boca Raton, FL, 1995), pp. 823–826.
8. D. F. Edwards and P. P. Hed, Appl. Opt. **26**, 4677 (1987).
9. J. C. Lambropoulos, T. Fang, P. D. Funkenbusch, S. D. Jacobs, M. J. Cumbo, and D. Golini, Appl. Opt. **35**, 4448 (1996).
10. J. C. Lambropoulos, S. D. Jacobs, B. Gillman, F. Yang, and J. Ruckman, in *Advances in Fusion and Processing of Glass II*, edited by A. G. Clare and L. E. Jones, Ceramic Transactions, Vol. 82 (The American Ceramic Society, Westerville, OH, 1998), pp. 469–474. See also Laboratory for Laser Energetics LLE Review **73**, 45, NTIS document No. DOE/SF/19460-212 (1997). Copies may be obtained from the National Technical Information Service, Springfield, VA 22161.
11. R. F. Cook and G. M. Pharr, J. Am. Ceram. Soc. **73**, 787 (1990).
12. I. J. McColm, *Ceramic Hardness* (Plenum Press, New York, 1990).
13. A. G. Evans, in *Fracture Mechanics Applied to Brittle Materials*, edited by S. W. Freiman (American Society for Testing and Materials, Philadelphia, 1979), Vol. ASTM STP 678, Part 2, pp. 112–135.
14. A. Arora *et al.*, J. Non-Cryst. Solids **31**, 415 (1979).
15. H. Li and R. C. Bradt, J. Non-Cryst. Solids **146**, 197 (1992).
16. J. C. Lambropoulos, S. Xu, and T. Fang, J. Am. Ceram. Soc. **79**, 1441 (1996).
17. J. Schulman, T. Fang, and J. Lambropoulos, *Brittleness/Ductility Database for Optical Glasses*, ver. 2.0, Department of Mechanical Engineering and Center for Optics Manufacturing, University of Rochester, Rochester, NY (1996).
18. H. M. Pollicove and D. T. Moore, Laser Focus World, March 1991, 145.
19. H. M. Pollicove and D. T. Moore, in *Optical Fabrication and Testing Workshop Topical Meeting*, 1992 Technical Digest Series (Optical Society of America, Washington, DC, 1992), Vol. 24, pp. 44–47.
20. S. S. Chiang, D. B. Marshall, and A. G. Evans, J. Appl. Phys. **53**, 298 (1982).
21. *ibid.*, 312.
22. A. G. Evans and E. A. Charles, J. Am. Ceram. Soc. **59**, 371 (1976).
23. B. R. Lawn, A. G. Evans, and D. B. Marshall, J. Am. Ceram. Soc. **63**, 574 (1980).
24. G. R. Anstis *et al.*, J. Am. Ceram. Soc. **64**, 533 (1981).
25. M. T. Laugier, J. Mater. Sci. Lett. **4**, 1539 (1985).
26. D. B. Marshall, B. R. Lawn, and A. G. Evans, J. Am. Ceram. Soc. **65**, 561 (1982).
27. M. Buijs and K. Korpel-van Houten, J. Mater. Sci. **28**, 3014 (1993).
28. M. Buijs and K. Korpel-van Houten, Wear **166**, 237 (1993).
29. J. Lambropoulos, M. J. Cumbo, and S. D. Jacobs, in *Optical Fabrication & Testing Workshop Topical Meeting* (Optical Society of America, Washington, DC, 1992), Vol. 24, pp. 50–53.
30. J. C. Lambropoulos, S. Xu, and T. Fang, Appl. Opt. **36**, 1501 (1997).
31. B. R. Lawn, T. Jensen, and A. Arora, J. Mater. Sci. **11**, 573 (1976).
32. B. R. Lawn and D. B. Marshall, J. Am. Ceram. Soc. **62**, 347 (1979).
33. R. Chauhan *et al.*, Wear **162–64**, 246 (1993).
34. L. M. Cook, J. Non-Cryst. Solids **120**, 152 (1990).
35. T. S. Izumitani, in *Workshop on Optical Fabrication and Testing: A Digest of Technical Papers* (Optical Society of America, Washington, DC, 1982), pp. 1–4.
36. J. C. Lambropoulos, in *Optical Fabrication and Testing*, 1996 Technical Digest Series (Optical Society of America, Washington, DC, 1996), Vol. 7, pp. 88–91.
37. S. D. Jacobs, D. Golini, Y. Hsu, B. E. Puchebner, D. Strafford, Wm. I. Kordonski, I. V. Prokhorov, E. Fess, D. Pietrowski, and V. W. Kordonski, in *Optical Fabrication and Testing*, edited by T. Kasai (SPIE, Bellingham, WA, 1995), Vol. 2576, pp. 372–382.
38. J. Lambropoulos, F. Yang, and S. D. Jacobs, in *Optical Fabrication and Testing*, 1996 Technical Digest Series (Optical Society of America, Washington, DC, 1996), Vol. 7, pp. 150–153.

Cholesteric Liquid Crystal Flakes—A New Form of Domain

The last 20 years have seen a growth of mixed-media systems in which cholesteric liquid crystals (CLC's) are one component. These include polymer-dispersed CLC's[1] in which the CLC's are confined to microdroplets within a continuous isotropic polymer and CLC's in gels[2] in which there is a small amount of polymer to stabilize the CLC structure. In either case, the continuity of the cholesteric texture is interrupted.

CLC's are characterized by a structure in which the average direction of molecules in a given plane, indicated by a unit vector called the director **n**, rotates about an axis. The continuously rotating director produces a helix. The length through which the director makes a complete 360° cycle is called the pitch *P* of the cholesteric. When the orientation of the helix axis is normal to the boundary surfaces, the texture produced is called Grandjean or planar.[3] This texture is responsible for the selective wavelength and polarization reflection unique to CLC's.[4] The center of the selective reflection wavelength band is given by

$$\lambda_0 = \bar{n}_n P, \tag{1}$$

where $\bar{n}_n$ = the average refractive index at a given plane perpendicular to the helix, calculated[5] from the ordinary and extraordinary cholesteric refractive indices.

The optical characterization of the CLC structure may be done by several methods. One of the simplest ways to evaluate the homogeneity of the Grandjean texture is with a polarizing microscope. A CLC sample aligned to the Grandjean texture is viewed between crossed polarizers. Dark areas indicate that the molecules through which the light has passed are either perfectly aligned with the polarizer or analyzer or isotropically distributed. In either case, for CLC's, dark spots and lines indicate deviations from cholesteric structure that are referred to as *disclinations*.[6,7] Regions between the disclinations are called *domains*, although there is some lack of consensus about the physical nature of a domain. There is some sense of a discrete area in which the director orientation is essentially constant, although this is usually subjectively determined by judging areas that appear homogeneous.[8,9] The term *monodomain* refers to regions that can be characterized by a single director. When directors characterize domains that are rather random with respect to each other, the region is considered *polydomain*.[10]

While domain boundaries may exhibit clear-cut disclinations, domains may not always be separated by a well-defined surface. Instead, there may be a discontinuity in the director orientation.[11] These discontinuities were first observed by Grandjean[12] and correctly described by Cano[13] as being caused by pitch deformations. The helix stretches or contracts to span the gap of the cell with an integer multiple of half-pitches. When the elastic limit is reached, the helix structure either inserts or removes a half-pitch. Although these discontinuities are called Cano *lines*, they do not actually appear as lines but as borders between regions differing in thickness by one half-pitch. Between crossed linear polarizers, this manifests as different retardances and therefore different colors.[14,15]

Other imaging techniques, including scanning electron microscopy (SEM), transmission electron microscopy (TEM), and atomic force microscopy (AFM), have been developed to image the periodic structure of CLC's in the planar/Grandjean texture. For example, a sample of low-molecular-weight (LM) CLC was frozen between metal sheets, the sheets were forced apart, and platinum-carbon replicas of the resulting fractured edges were examined by SEM.[16–18] Periodic striations corresponding to the half-pitch suggested that the fracturing occurred along the helix profile. Even disclinations could be viewed by this technique. Not only replicated samples but also the frozen CLC's themselves were examined using SEM.[19] Because of LMCLC samples unfreezing or ice building up on the surfaces, DeGennes[20] suggested the use of polymerized CLC's for SEM study. This experiment was conducted for the first time in 1993[21] to visualize the molecular distribution around a Cano line. The images showed that there were layers to the molecular distribution, but no additional quantitative analysis was done.

Atomic force microscopy, developed in 1985,[22] has been used to examine Langmuir–Blodgett and transferred freely-suspended liquid crystal films[23] as well as liquid crystal films on graphite.[24] Liquid crystal films have shown some two-dimensional structure and some cholesteric periodicity but are often deformed by contact with the cantilever tip.

Cyclic polysiloxane oligomers,[25,26] in particular, have been examined by Bunning *et al*.[27,28] with TEM and AFM. Samples for these studies were aligned to the Grandjean texture by shearing between Teflon sheets, cooled to below their glass transition temperatures, and microtomed, producing samples free of the effect of underlying support[29] substrates. Results indicate that the cyclic polysiloxanes do show corrugated fresh surfaces with a periodicity equal to one-half the pitch. From TEM and AFM results, in conjunction with x-ray diffraction studies, Bunning *et al*.[30,31] drew further conclusions regarding the structural morphology. Their proposed structure consists of interdigitated sidechains, the extent of association being dependent on the composition and temperature. The siloxane backbones form layers that twist into the helical structure of the cholesteric with the sidechains aligned along the director **n**.

Imaging the multiple domains of the CLC's within mixed-media systems by the techniques described above is complicated by the production methods of these mixed-media systems. Methods include (a) emulsification[32] of the liquid crystal with a polymer and (b) phase separation[33] of the liquid crystal from solution with a polymer. The CLC domains are produced at the same time as the mixed medium itself. As a result, the domains can be characterized only *within* the medium. The domains may be diluted or contaminated by other components of the mixture.[34] Polymer "walls" may affect molecular alignment at domain boundaries.[35]

In this article, we describe the production and characterization of a new form of CLC's called *flakes*, proposed by Faris.[36] We examine individual flakes by optical light microscopy, SEM, and AFM. We will show that flakes maintain many of the optical properties of the continuous films from which they are made. The CLC flakes can be embedded into a host to form a new type of mixed medium in which the flakes provide well-characterized CLC domains. We will show how the orientation of these CLC flakes can be evaluated quantitatively using Bragg's Law in the form of Fergason's Equation:[37]

$$\lambda_r = \lambda_0 \cos\left\{\frac{1}{2}\left[\sin^{-1}\left(\frac{\sin\theta_i}{\bar{n}_{\mathrm{ch}}}\right)+\sin^{-1}\left(\frac{\sin\theta_r}{\bar{n}_{\mathrm{ch}}}\right)\right]\right\}, \quad (2)$$

where λ_0 = the wavelength at the center of the selective reflection band at normal incidence, λ_r = the wavelength at the center of the selective reflection band at oblique incidence, θ_i = incidence angle, θ_r = observation angle in air, and $\bar{n}_{\mathrm{ch}}$ = the approximate average cholesteric refractive index.

The orientation of CLC flakes can be further understood by using a function known as turbidity τ. This useful parameter has been developed[38] for nematic droplets dispersed in a matrix that does not absorb liquid crystal. It characterizes the extent of scattering as a function of incidence angle and refractive index mismatch in the anomalous diffraction regime. Turbidity has not yet been investigated for cholesteric materials, but for nematics has been defined as

$$\tau = -\ln\left[\frac{T_{\mathrm{sample}}(\theta_i)}{T_{\mathrm{blank}}(\theta_i)}\right]\frac{\cos\left[\sin^{-1}\left(\sin\theta_i / n_{\mathrm{med}}\right)\right]}{t}, \quad (3)$$

where $T_{\mathrm{sample}}(\theta_i)$ = transmittance of a sample, $T_{\mathrm{blank}}(\theta_i)$ = transmittance of a blank used to correct for reflection from the film and substrate, t = thickness of the sample, and n_{med} = the refractive index of the embedding medium.

Preparation of CLC Flakes

Two types of cyclic polysiloxanes were used in this study: (a) noncrosslinkable of the type shown in Fig. 74.73 (adapted from Ref. 26), obtained from Wacker–Chemie in Munich[39] and designated CLC670, which refers to its λ_0 in nm and (b) crosslinkable, designated CC3767 and similar to that of Fig. 74.73 but with terminal methacryl groups and crosslinked by UV curing in the presence of a photoinitiator.[40] The exact ratios of chiral to nonchiral side-chains and the amount of added monomer (to reduce viscosity for ease of workability) are proprietary to the manufacturer.

In a procedure referred to as "knife-coating," the noncrosslinkable material is applied onto a silicon wafer,[41] which is heated to 130°C on a hotplate;[42] polysiloxane is then melted onto the substrate surface. A microscope slide placed on edge and referred to as the "knife" is used to smear the polysiloxane across the surface. This knife-coating process causes the CLC to be aligned in the Grandjean texture as observed by reflective color. The substrate is then quickly removed from the hotplate, allowing the CLC to be quenched to room temperature, "freezing in" the helical structure of the Grandjean texture. The CLC films prepared in this way are ~30 μm thick.

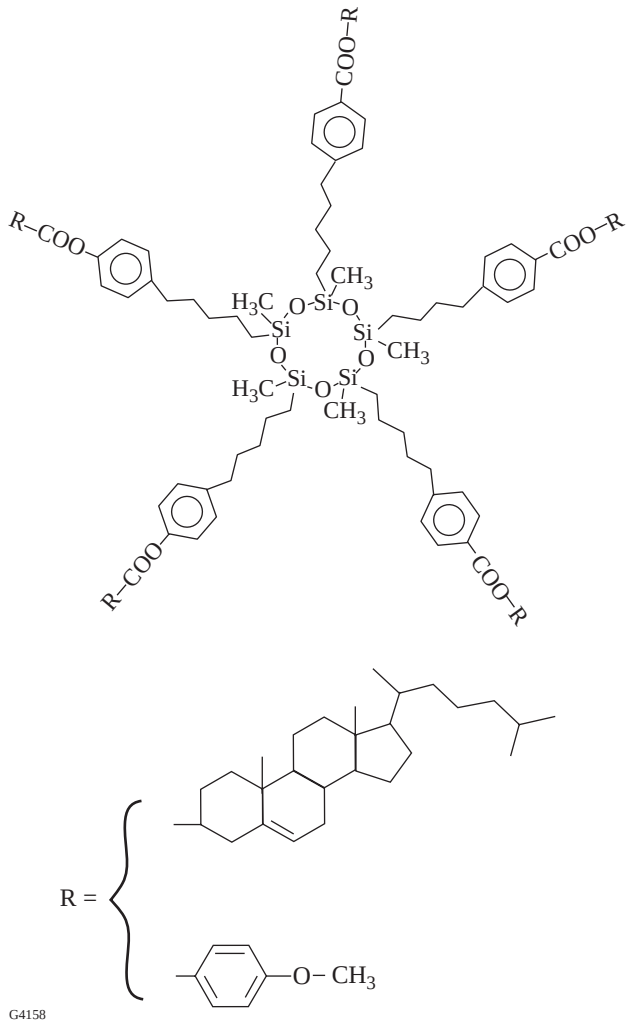

Figure 74.73
Structure of cyclic polysiloxane used in this study.

The crosslinked material is prepared by mixing the CLC with photoinitiator (1.5% by weight), sprinkling in 13-μm-sized glass fiber spacers,[43] and shearing the mixture between two 3-cm-diam, fused-silica substrates at 100°C. The sandwich cell, still at 100°C, is exposed for 2 min to ultraviolet light of $\lambda = 365$ nm and 15 mW/cm^2 at 5-cm distance.[44] After curing, the cell is pried open with a razor blade to expose the cured film.

For either method of preparation, the resulting "open-faced" film is placed in a Petri dish and covered with liquid nitrogen. The polymer CLC fractures and lifts slightly and temporarily off the silicon or glass surface. Methanol is used to wash the fractured CLC off the substrate.

Imaging Individual Flakes

1. Light Microscope

Viewed under a light microscope, flakes appear to be irregularly shaped with sharp corners. Figure 74.74 shows a micrograph of CLC670 flakes between crossed polarizers.[45] All samples show similar features. The flakes themselves appear to have few disclinations or Cano lines, suggesting that fracturing occurred along disclinations and discontinuities in the film, consistent with theoretical freeze-fracture models.[17]

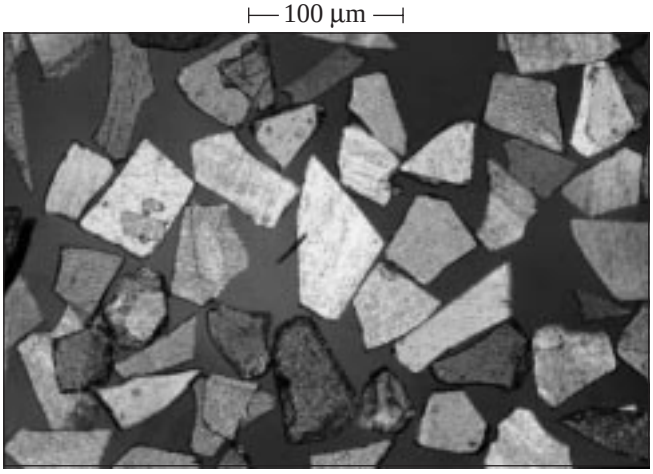

Figure 74.74
Photomicrograph of CLC670 flakes.

2. Scanning Electron Microscope

CC3767 (crosslinked) flakes were sputtered with silver and examined using scanning electron microscopy.[46] Samples like the one in Fig. 74.75 are seen to have an even more irregular structure than that which appeared under light microscopy. Some swelling is apparent at the edges of the flakes, which we attribute to absorption of the methanol used for the slurry. Periodic ridges are evident on many of the flakes. The freeze-fracture process appears to occur along the cholesteric helix profile, perpendicular to the director. From rough estimation of the magnitude of the pitch measured physically on the SEM observation screen, the pitch appears to be 486 nm. Based on Eq. (1) and prefracture measurements of λ_0 (= 712 nm) and $\bar{n}_n$ (= 1.5812 at 712 nm), the optically calculated pitch for this sample is 450 nm. The similar magnitude of the numbers suggests that the observed periodic ridges are, in fact, indicative of pitch. Due to parallax caused by the tilt of the sample and the SEM sample table, however, measurements from these photographs are only estimates.

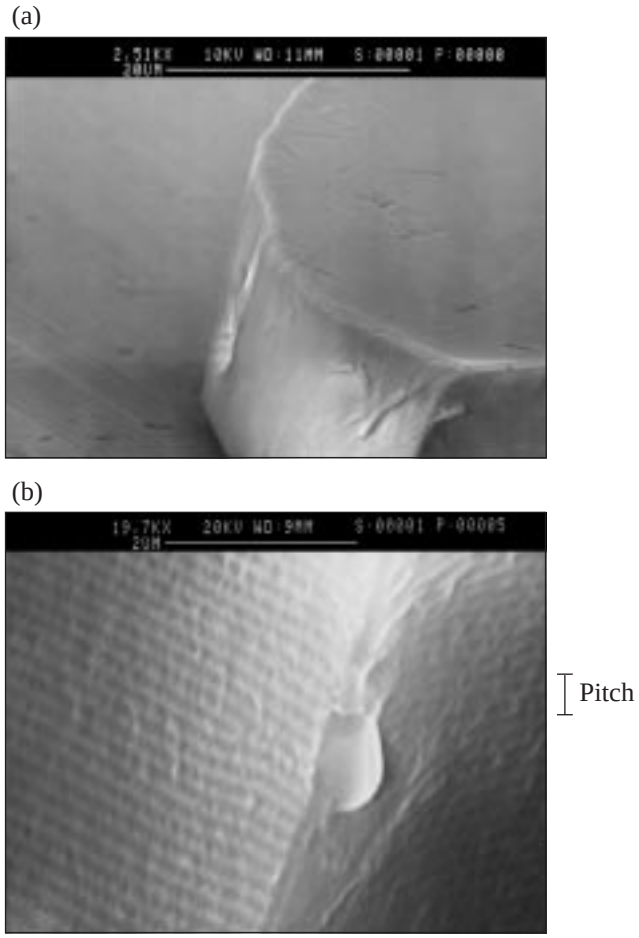

Figure 74.75
Scanning electron micrographs of a CLC flake (sample: CC3767). (a) There is slight swelling at the edges of a flake. (b) At higher magnification, periodic ridges corresponding to the pitch can be seen.

The noncrosslinked flakes were also examined with SEM. These also showed ridges consistent with half-pitch periodicity. Neither sputtering nor SEM voltage appeared to damage, melt, or decompose any of the flakes.

3. Atomic Force Microscope

To determine pitch physically and without parallax, a single CC3767 flake was mounted vertically against a small piece of glass using epoxy.[47] The flake was placed in an atomic force microscope[48] whose tip consisted of a pyramidal crystal of silicon nitride attached to a cantilever. The edge of the flake was rastered under this cantilever. Deflections of the cantilever by the surface resulted in an image profile of the surface like the one shown in Fig. 74.76. Our images are consistent with the microtomed and free-surface AFM images of cholesteric polysiloxanes obtained by Meister *et al.*[49] and provide a third unique view of the cholesteric corrugation due to pitch periodicity.

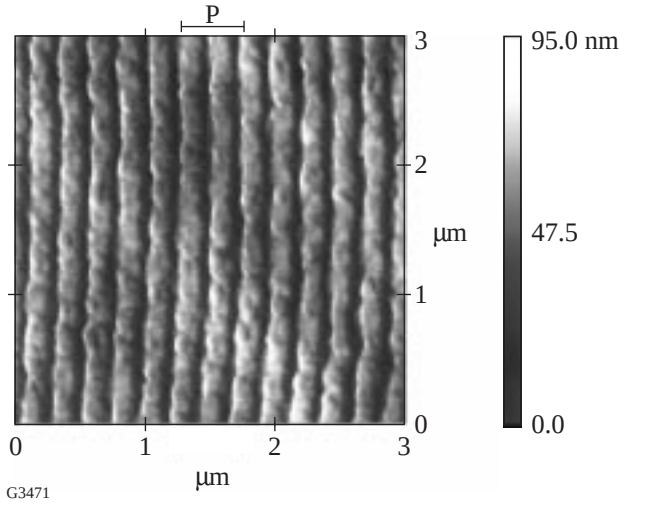

Figure 74.76
Atomic force micrograph of a CLC flake edge (sample: CC3767). The pitch measured from this image is 451 nm.

Since there is no parallax in this image, the pitch can be measured directly to be 451 nm. The pitch calculated from the prefracture optical measurements, listed in the **Scanning Electron Microscope** section, is 450 nm. The excellent agreement confirms that the ridges seen in both SEM and AFM images are those of the cholesteric helix profile exposed by freeze-fracturing. More importantly, the process of producing flakes from polymer CLC films maintains the pitch and, as we will show, the selective wavelength reflection capability of the original film.

AFM measurements of the noncrosslinkable CLC670 gave equally good agreement of physically measured and optically calculated pitch. The remaining tests described below used only the noncrosslinkable material to avoid the time-consuming process of preparing, curing, and splitting sandwich cells.

Sizing of CLC Flakes

To separate flakes by size, a stack of stainless steel screen sieves[50] is used. Table 74.V lists the mesh sizes and nominal particle-size ranges when stacked in order of increasing mesh number. Flakes in methanol slurry are dripped into the sieve stack, using methanol to wash the flakes through. Each stage is washed with methanol until the effluent appears visually clear. Material retained by each sieve is collected by methanol slurry and allowed to dry by evaporation. For a typical initial charge

Table 74.V: Sieve designations and measured ranges of CLC670 flakes.

Sieve designation (mesh size)	Nominal particle-size range (μm) that should be trapped in sieve	Median and standard deviation of each sieve group of CLC670 flakes measured by Horiba LA-900 (μm)
80	>180	218±204
170	90–180	124±28
325	45–90	66±26
635	20–45	35±16
Pan	<20	24±14

of about 5 g of flakes, the sieving process typically requires about 5 h to completely separate the larger-sized flakes (>45 μm) into three groups. The "20- to 45-μm" sieve cut takes an additional 4 h of sieving time. All separated samples are allowed to dry for 4 days.

To test whether the sieve separation technique was efficient, each sieve cut (what was trapped in the sieve as well as the final bottom collection pan) was tested for particle-size distribution using the Horiba LA-900 Particle Analyzer.[51] In this instrument, the particles are suspended in a fluid. For the CLC flakes, this fluid was methanol. No additional surfactant was used since initial testing with detergent as a surfactant led to the formation of bubbles, which interfered with particle detection. A small-fraction sample container of approximately 50-mL volume was used. In the small-fraction container, particles were kept in suspension in the instrument's light beam using a magnetic stirrer. The particles scattered and diffracted light from both a HeNe laser beam and a beam from a halogen lamp. The latter was equipped with two filters: one to pass 610-nm light and one to pass 480-nm light. Size distribution was determined based on an instrument algorithm that calculates the distribution of spherical particles that would give the same scattering pattern as the sample particles. The distribution of the algorithm's spherical particles is given as a percent frequency F%. The size range detectable by the Horiba LA-900 is 0.04 to 1000 μm. Plots are typically Gaussian in shape on a semilogarithmic scale for a natural distribution of particles.[52] For particles that are not uniform in shape, such as the CLC flakes, the particle analyzer detects the largest dimension,[53] so the median value of such a distribution lies on the high side of the sieve designation. The measured results are shown in Table 74.V.

Each size-group of CLC670 is plotted in Fig. 74.77 to show if the different size-group distributions are well or poorly separated. The vertical lines indicate the nominal ranges based on the sieve designations listed in Table 74.V. The medians and modes are well separated. In general, however, the ">180-μm" group contains flakes that exceed the Horiba LA-900 size-detection limits. The "<20-μm" group shows some agglomeration. Otherwise, each mode falls within the sieve-size designation. There is overlap among the groups within the standard deviations for each distribution, so we may expect to see trends in optical behavior related to size but probably no optical behavior unique to a particular size-group since each group contains some flakes whose sizes are common to adjacent groups.

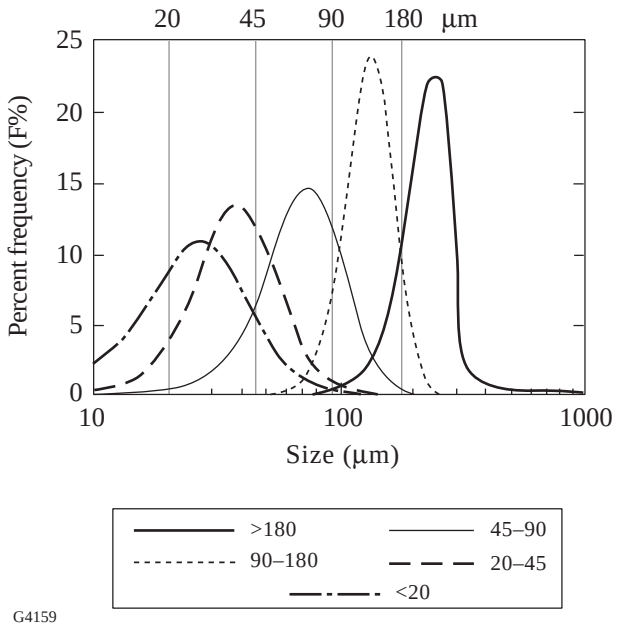

Figure 74.77
Effectiveness of sieving for separating size-groups. The vertical lines indicate the nominal size limits of the sieve designations.

Orientation of CLC Flakes

Glass disk substrates made from a conveniently available float glass ($n_{D,20} = 1.533$, 25-mm diameter, 1 mm thick) were weighed; then 1 mL of deionized water was dropped by graduated pipet onto each substrate to cover it to the edge. Flakes in methanol slurry were dripped onto the water bead by a medicine dropper. The flakes oriented themselves with their largest surface parallel to the meniscus. When the surface was visually covered with flakes, the underlying fluid was removed by medicine dropper. Each sample was allowed to dry. At regular intervals, each sample was weighed until three identical readings were obtained, indicating that the samples had completely dried (about 48 h total). After all the optical tests were completed for a given sample, its thickness was measured by contact gauge[54] in five spots and averaged. The gauge tip tended to disturb the flakes, so thickness measurements could not be made until optical testing was completed.

Since the >180-μm and <20-μm sieve groups for CLC670 were of anomalous size, they were excluded from optical testing so that comparisons of size effects on optical behavior could be drawn with more certainty by being based on the other three sieve groups. In addition, the >180-μm flakes, when oriented by water bead, did not completely cover the substrate. The <20-μm flakes, when oriented by water bead, tended to aggregate into visually observable inhomogeneities. Therefore, even qualitative comparisons involving these extreme sizes were not feasible.

Selective Reflection

Transmittance profiles of each size-group were determined by spectrophotometer[55] at 0° incidence. The results of three size-groups are shown in Fig. 74.78. There is a dramatic drop in overall transmittance with decreasing flake size; however, each size-group continues to show the selective wavelength reflection (manifested by a transmittance valley) characteristic of CLC's.

In addition, a CLC670 "45- to 90-μm" sample prepared by water-bead orientation was examined in transmission using right-hand circular and then left-hand circular incident polarization. Figure 74.79 shows that the CLC flakes continue to exhibit the selective polarization-handedness reflectivity also characteristic of CLC's.

Clearly, we have discrete CLC domains of prealigned Grandjean texture that continue to exhibit the selective wavelength and polarization of unfractured CLC films or of CLC polymer-dispersed or gel systems. These domains, however, are uncontaminated by any processing steps. The CLC flakes are also not subject to the alignment deformities that might be caused by confining walls.

The additional optical tests performed on these CLC flake samples will allow us to make comparisons by flake-size of orientation quality. In particular, we will look at the angle dependence of both the selective reflection wavelength and the scattering, considering CLC flakes as distributions of discrete cholesteric domains.

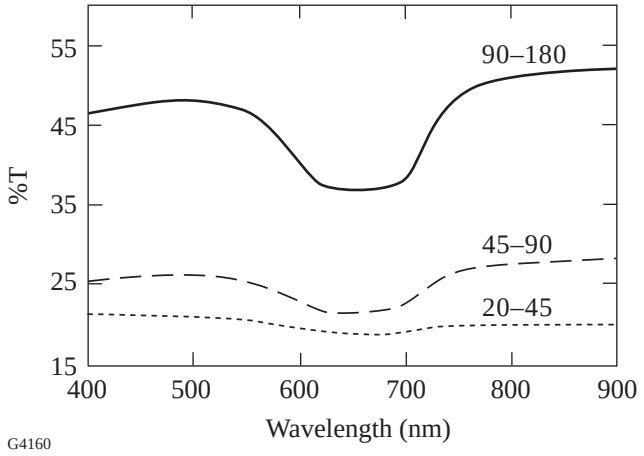

Figure 74.78
Transmittance profiles of three sieve groups.

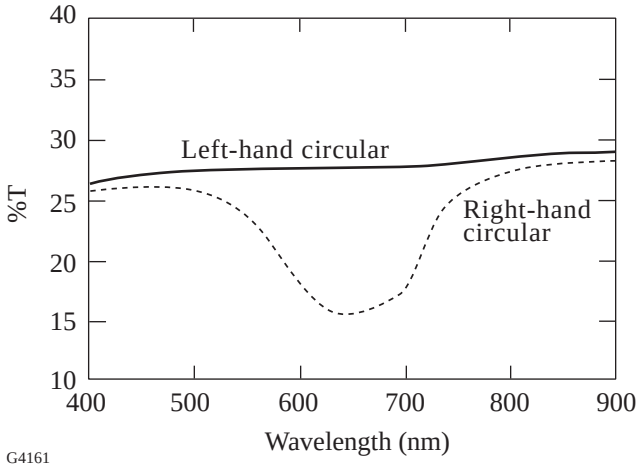

Figure 74.79
Selective polarization handedness of CLC flakes.

Angle Dependence of Selective Wavelength

Three to four samples from each size-group were prepared and examined in transmission at seven incidence angles (0°–60°). The center of the selective wavelength band was estimated by visual integration and recorded as λ_r-meas. The wavelength at 0° was recorded as λ_0. Equation (1) was used to calculate λ_r-theo. When measuring in transmission, the implicit assumption is $\theta_i = \theta_r$. The value of $\bar{n}_{ch}$ is 1.6, based on Abbe refractometer[56] measurements of the unfractured CLC films by a technique determined earlier for nematic liquid crystal polymers.[57] Figure 74.80 shows how well the average selective-reflection-wavelength measurements from each size-group agree with the calculated theoretical values.

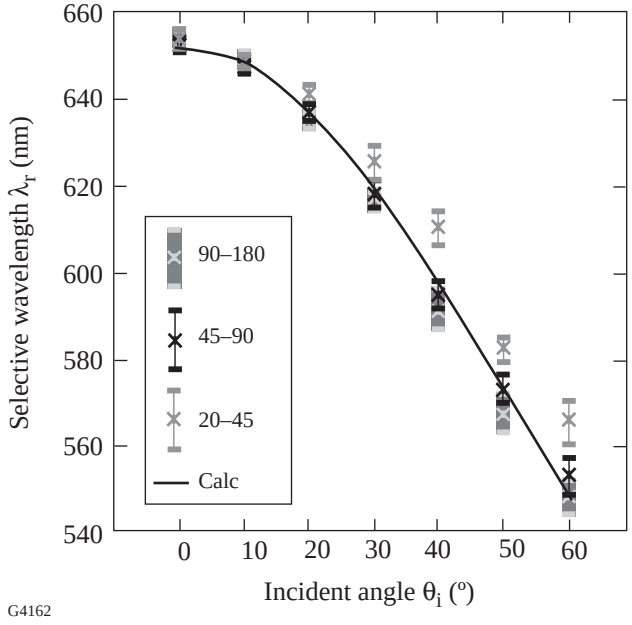

Figure 74.80
Angle dependence of selective wavelength reflection as a function of flake size.

The 45- to 90-μm flakes show better agreement with Bragg's Law in the form of Fergason's Equation than do the other two size-groups. We attribute this to a better orientation of the medium-sized flakes on the substrate. Their aspect ratio is large enough that the largest dimension is perpendicular to the thickness, so, during the water-bead orientation, the helix axis can align perpendicular to the substrate.

Scattering

We will interpret "scattering" here to refer to any redirection of light from its original path of propagation. As such, use of turbidity as a measure of scattering simply compares transmittance of samples, where lower transmittance corresponds to greater scattering. This section will show that the primary source of scattering by CLC flakes is the misalignment of the helix axes of individual flakes with respect to the substrate.

The same CLC670 samples prepared for angle-dependent wavelength studies were used for turbidity calculations. Turbidity was measured with a horizontal-pass HN32 Polaroid polarizing film[58] in the spectrophotometer as part of the background correction protocol. As incident angle was increased, the incident polarization remained *P*-polarized. The wavelength chosen for turbidity measurements needed to be well outside the selective reflection region, outside the region of substrate or CLC absorptivity, and part of a normal transmission scan that would not involve lamp, detector, or other voltage-dependent instrument changes; therefore, the chosen measurement wavelength was 900 nm.

The %T of a "blank" sample, i.e., a sample with everything but the liquid crystal, as well as the %T of the sample *with* liquid crystal were recorded at the same incident angle. Turbidity was calculated for all samples using Eq. (3) and averaged within each size-group at each incidence angle. Figure 74.81 shows the turbidity ranges of multiple samples of each group as well as for an unfractured continuous film. For each sieved size-group, the turbidity increases as the incident angle increases. The smaller the flakes, the higher the turbidity per unit thickness.

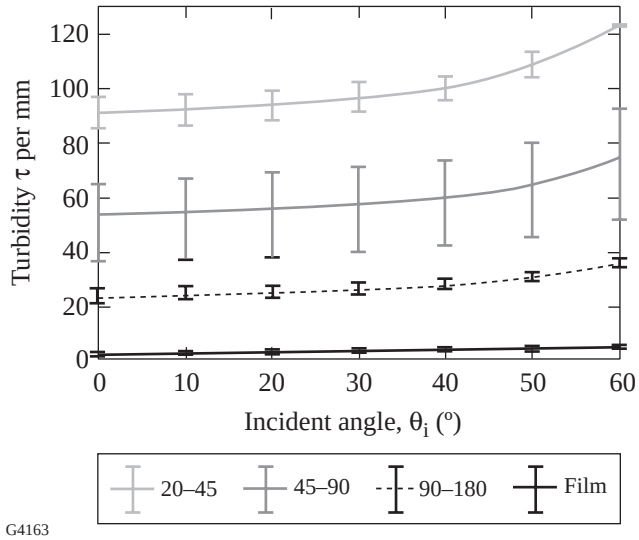

Figure 74.81
Turbidity ranges of multiple samples of each sieve group of CLC670 flakes.

As we saw in Fig. 74.78, transmission scans of flake samples of decreasing median size grow gradually wider and flatter with overall lower-percent transmittance. Due to their small aspect ratio, smaller flakes are not necessarily aligned with their helix axes perpendicular to the substrate. There will, then, be many angles of incidence and reflection for which some wavelength of a spectral scan will meet the Bragg/Fergason criterion of Eq. (2). Selective reflection may be expected to occur fairly uniformly across the spectrum as the variety of CLC flake orientations increases. As flake sizes get smaller, more flakes are required to cover the same sample area, resulting in this increase in orientation possibilities. Consequently, the turbidity increases as the disorder of the smaller flakes redirects more light out of the original propagation direction.

The flakes are still not small enough to be of the size of the measurement wavelength so we are examining the scattering geometrically. In anticipation of eventually being able to make CLC flakes as small as the domains of the other more common mixed-media systems,[59] the use of turbidity as a measure of scattering is used in this study even though it was developed originally for the so-called anomalous diffraction regime[60,61] in which the wavelength is only slightly smaller than the scatterers.

In analogy with mixed-media systems that employ index match or index mismatch to control scattering, the CLC flake samples were overcoated with one of two transparent hosts: (a) a silicone elastomer designated SE2061,[62] which has an ~0.2 index difference, *Dn*, from the average cholesteric index of CLC670 or (b) a transparent enamel filtered[63] from a commercially available paint[64] with a <0.04 index difference, *Dn*, from CLC670. In the overcoating process, 1 mL of host in a graduated medicine dropper was added dropwise to the center of the flake sample. Each host flowed uniformly and in its own time to the edge of the sample substrate. The overcoated flake samples were measured in the same way as the others, and turbidity was calculated for seven incident angles.

The turbidities of an uncoated sample, a sample overcoated with the moderate index match (SE2061), and a sample overcoated with the close index match (Testor's Enamel) are plotted for each size-group in Figs. 74.82(a), 74.82(b), and 74.82(c). In every case, overcoating with a host reduces the turbidity of the flake samples. There appears to be less of a difference between a moderate and a good index match than between a coated and an uncoated sample regarding turbidity of the larger flakes. In addition, the overcoated flakes show a narrower selective reflection band than uncoated flakes,[65] suggesting that the overcoating process improves the orientation of the flakes. This may explain why there was only a slight difference in turbidity between moderately and nearly index-matched CLC flakes: It is not the index match but rather

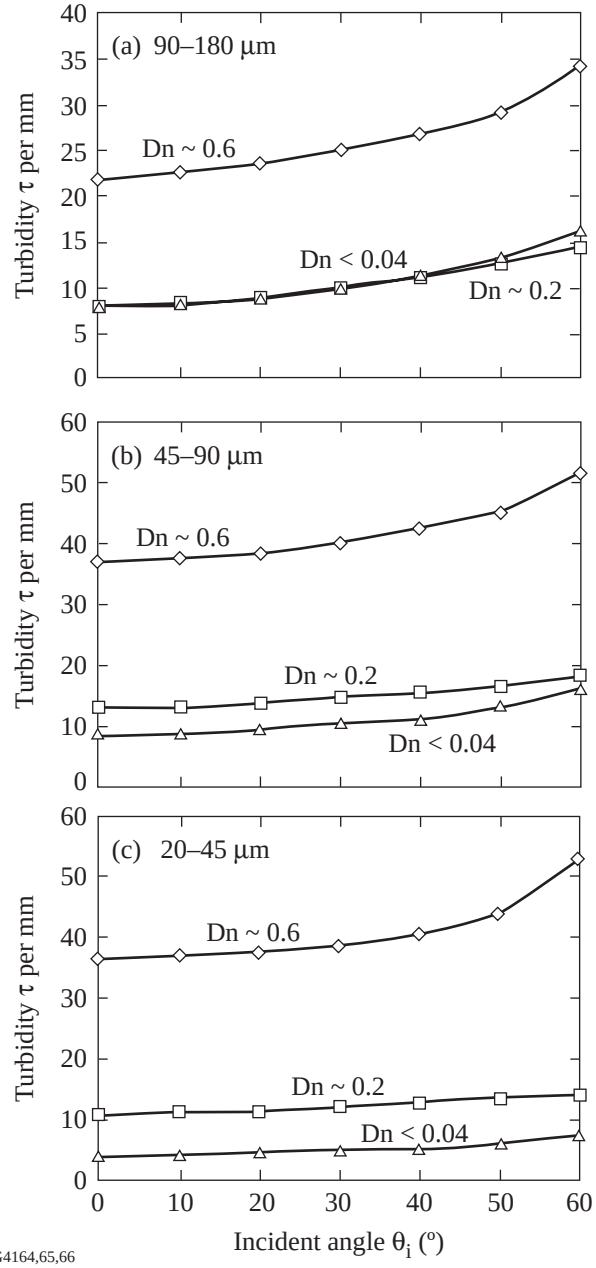

Figure 74.82
Comparison of turbidities of each flake size-group as a function of index match and incident angle. Each legend indicates the index mismatch of the flakes and host: 0.6 is air, 0.2 is SE2061, and <0.04 is enamel. The flake size-groups shown are (a) 90 to 180 μm, (b) 45 to 90 μm, and (c) 20 to 45 μm.

the flowing action of the hosts that reorients the flakes and reduces scattering.

Applications of Results

CLC flakes as part of a mixed medium can provide three main venues of use: decorative arts, document security, and models of other mixed-media systems. In the realm of decorative arts, we have shown elsewhere[66] that CLC flakes, with or without a host, can be successfully modeled and measured by standard colorimetric methods. As such, CLC flakes in a suitable host, such as the enamel used in this study, provide versatile paints and inks, which we have applied by brush, airbrush, and fountain pen to surfaces including paper, cloth, metal, and glass.

CLC flakes may also be considered for use in document security. Polymerized CLC films have been suggested for this purpose as overlays.[67] CLC flakes can be embedded into paper currency, for example, avoiding the problem caused by thin, brittle films. The use of CLC's allows angle-dependent color suitable for first-line identification. The unique polarized-reflection capability of CLC flakes provides a further deterrent to counterfeit reproduction.

Finally, CLC flakes are discrete cholesteric domains, which exhibit none of the limitations of polymer-dispersed and gel systems such as boundary deformations, high-voltage requirements, or domain contamination. With narrower sieve cuts to provide better flake-size uniformity, CLC flakes can provide an excellent physical model of the other mixed-media systems in which the domain is not so clearly characterized. Some work must be done to reduce CLC flake sizes for even closer modeling capability. Toward this end, small quantities of CLC flakes that are only 7 μm thick have been prepared.[68]

Conclusions

We have shown that CLC polysiloxane oligomer films can be fractured into smaller domains called flakes. These CLC flakes can be separated by size and oriented using flotation on an aqueous meniscus. CLC flakes maintain the wavelength and polarization selectivity of the original film. The CLC flakes can also be embedded into an isotropic polymer as a new kind of mixed medium in which the cholesteric domain structure is not contaminated, diluted, voltage dependent, or deformed. As work with this new mixed medium continues, we anticipate that narrower sieve cuts and smaller flakes will allow better use of CLC flakes as models for polymer-dispersed and gel CLC systems.

ACKNOWLEDGMENT

The authors thank Dr. F.-H. Kreuzer and Dr. Robert Maurer of the Consortium für elektrochemische Industrie GmbH and Munich for the CLC polysiloxanes. This work was supported by the U. S. Department of Energy, Office of Inertial Confinement Fusion under Cooperative Agreement DE-FC03-92SF19460, the University of Rochester, and the New York State Energy Research and Development Authority. The support of DOE does not constitute an endorsement by DOE of the views expressed in this article. Funding was also provided by Reveo, Inc.

REFERENCES

1. P. P. Crooker and D. K. Yang, Appl. Phys. Lett. **57**, 2529 (1990).
2. R. A. M. Hikmet, Liq. Cryst. **9**, 405 (1991).
3. G. S. Chilaya and L. N. Lisetski, Mol. Cryst. Liq. Cryst. **140**, 243 (1986).
4. HL. De Vries, Acta Cryst. **4**, 219 (1951).
5. W. U. Müller and H. Stegemeyer, Berichte der Bunsen-Gesellschaft. **77**, 20 (1973).
6. F. C. Frank, Faraday Discuss. Chem. Soc. **25**, 19 (1958).
7. M. Kléman, Rep. Prog. Phys. **52**, 555 (1989).
8. C. M. Dannels and C. Viney, Polymer News. **16**, 293 (1991).
9. C. Viney and C. M. Dannels, Mol. Cryst. Liq. Cryst. **196**, 133 (1991).
10. L. L. Chapoy, B. Marcher, and K. H. Rasmussen, Liq. Cryst. **3**, 1611 (1988).
11. A. Keller *et al.*, Faraday Discuss. Chem. Soc. **79**, 186 (1985).
12. M. F. Grandjean, Comptes Rendus Acad. Sci. **172**, 71 (1921).
13. R. Cano, Bull. Soc. fr. Minéral. Cristallogr. **92**, 20 (1968).
14. P. Kassubek and G. Meier, in *Liquid Crystals 2: Proceedings of the 2nd International Liquid Crystal Conference*, edited by G. Brown (Gordon and Breach, New York, 1969), pp. 753–762.
15. P. E. Cladis and M. Kléman, Mol. Cryst. Liq. Cryst. **16**, 1 (1972).
16. M. J. Costello, S. Meiboom, and M. Sammon, Phys. Rev. A. **29**, 2957 (1984).
17. D. W. Berreman *et al.*, Phys. Rev. Lett. **57**, 1737 (1986).
18. F. Livolant and Y. Bouligand, Mol. Cryst. Liq. Cryst. **166**, 91 (1989).
19. J. Voss and B. Voss, Z. Naturforsch. **31a**, 1661 (1976).
20. P. G. deGennes, *The Physics of Liquid Crystals*, 1st ed. (Clarendon Press, Oxford, 1974), p. 272.
21. I. Heynderickx, D. J. Broer, and Y. Tervoort-Engelen, Liq. Cryst. **15**, 745 (1993).

22. G. Binnig, C. F. Quate, and Ch. Gerber, Phys. Rev. Lett. **56**, 930 (1986).

23. R. M. Overney *et al.*, Langmuir **9**, 341 (1993).

24. H. Yamada, S. Akamine, and C. F. Quate, Ultramicroscopy **42–44**, 1044 (1992).

25. H. Finkelmann and G. Rehage, Makromol. Chem., Rapid Commun. **1**, 31 (1980).

26. F.-H. Kreuzer *et al.*, Mol. Cryst. Liq. Cryst. **199**, 345 (1991).

27. T. J. Bunning *et al.*, Liq. Cryst. **16**, 769 (1994).

28. T. J. Bunning *et al.*, Materials Directorate, Wright Laboratory, Wright-Patterson Air Force Base, OH, Interim Report #WL-TR-91-4089 (July 1989–June 1991).

29. C. Viney, G. R. Mitchell, and A. H. Windle, Mol. Cryst. Liq. Cryst. **129**, 75 (1985).

30. T. J. Bunning *et al.*, Mol. Cryst. Liq. Cryst. **231**, 163 (1993).

31. T. J. Bunning *et al.*, Liq. Cryst. **10**, 445 (1991).

32. J. L. Fergason, in *1985 SID International Symposium, Digest of Technical Papers*, edited by J. Morreale (Pallisades Inst. Res. Services, New York, 1985), pp. 68–70.

33. J. W. Doane *et al.*, Appl. Phys. Lett. **48**, 269 (1986).

34. M. Radian-Guenebaud and P. Sixou, Mol. Cryst. Liq. Cryst. **220**, 53 (1992).

35. D. K. Yang and P. P. Crooker, Liq. Cryst. **9**, 245 (1991).

36. S. M. Faris, U.S. Patent No. 5,364,557 (15 November 1994).

37. J. L. Fergason, Mol. Cryst. **1**, 293 (1966).

38. P. S. Drzaic and A. M. Gonzales, Appl. Phys. Lett. **62**, 1332 (1993).

39. F. Kreuzer, Wacker-Chemie, Consortium für Elektrochemische Industrie GmbH, Zielstattstrasse 20, D-81379 München, Germany.

40. The photoinitiator used is Irgacure-907, the trade name for 2-methyl-1,[4 methyl thiophenyl]2 morpholino propanone-1. Ciba Additives, Ciba-Geigy Corporation, Hawthorne, NY 10532-2188.

41. Silicon Epiprime, 100-mm-diam wafers, WaferNet, Inc., San Jose, CA 95131.

42. Dataplate digital hotplate/stirrer, PMC Industries, Inc., San Diego, CA 92121.

43. Ultra-Precision Glass Fibers, EM Industries, Inc., Advanced Chemical Division, Hawthorne, NY 10532.

44. UV Lamp Model B-100AP and Blak-Ray Ultraviolet Meter Model J-221, UVP, Inc., San Gabriel, CA 91778.

45. Photo used as October image in the American Institute of Physics 1996 "Beauty of Physics" calendar, Photographer: E. M. Korenic, Laboratory for Laser Energetics, University of Rochester, Rochester, NY 14623-1299.

46. In cooperation with Brian McIntyre, Scanning Electron Microscopist, The Institute of Optics, University of Rochester, Rochester, NY 14627.

47. Devcon® 5 Minute® Epoxy, ITW Devcon, Illinois Tool Works Company, Danvers, MA 01923.

48. Digital Instruments Nanoscope® III Scanning Probe Microscope, Digital Instruments, Inc., Santa Barbara, CA 93117.

49. R. Meister *et al.*, Phys. Rev. E **54**, 3771 (1996).

50. Newark Wire Cloth Company, Newark, NJ 07104.

51. LA-900 Laser Scattering Particle Size Distribution Analyzer, Horiba Instruments, Inc., Irvine, CA 92714.

52. T. Allen, in *Pigments—An Introduction to Their Physical Chemistry*, edited by D. W. Patterson (Elsevier, Amsterdam, 1967), Chap. 6, pp. 102–133.

53. M. Pohl, Horiba Instruments, Inc., Irvine, CA (private communication) (1994).

54. Digimatic indicator IDC Series 543, Mitutoyo Corporation, Paramus, NJ 07652.

55. Perkin-Elmer Model Lambda-9 spectrophotometer, Perkin-Elmer Corporation, Norwalk, CT 06859-0012.

56. Bellingham and Stanley Model 60/HR Abbe Refractometer, Bellingham and Stanley Ltd., North Farm Industrial Estate, Tunbridge Wells, Kent TN2 3EY, England.

57. E. M. Korenic, S. D. Jacobs, J. K. Houghton, A. Schmid, and F. Kreuzer, Appl. Opt. **33**, 1889 (1994).

58. HN32 Polaroid® linear polarizing film, Polaroid®, Polarizing Division, Norwood, MA 02062.

59. G. P. Montgomery, Jr., J. L. West, and W. Tamura-Lis, J. Appl. Phys. **69**, 1605 (1991).

60. S. Zumer, Phys. Rev. A **37**, 4006 (1988).

61. P. S. Drzaic, Mol. Cryst. Liq. Cryst. **261**, 383 (1995).

62. Petrarch Systems, Inc., Bristol, PA 19007.

63. Millex®-FG_{13} Filter Unit, 0.2 μm, Millipore Corporation, Bedford, MA 01730.

64. Testor's Gloss Enamel Gold (#1144), The Testor's Corporation, Rockford, IL 61104.

65. E. M. Korenic, "Colorimetry of Cholesteric Liquid Crystals," Ph.D. thesis, The Institute of Optics, University of Rochester, 1997, pp. 216–219.

66. E. M. Korenic, "Colorimetry of Cholesteric Liquid Crystals," Ph.D. thesis, The Institute of Optics, University of Rochester, 1997.

67. R. L. van Renesse, in *Optical Document Security*, edited by R. L. van Renesse (Artech House, Boston, 1994), Chap. 13, pp. 263–280.

68. S. D. Jacobs and T. Pfuntner, Laboratory for Laser Energetics, University of Rochester, Rochester, NY 14623-1299 (private communication) (1995).

Publications and Conference Presentations

Publications

R. Betti, V. N. Goncharov, R. L. McCrory, and C. P. Verdon, "Feedthrough and Dynamic Stabilization in Convergent Geometry," in *Laser Interaction and Related Plasma Phenomena*, edited by G. H. Miley, E. M. Campbell, W. J. Hogan, C. Maille-Petersen, H. Coppedge, and E. Montoya (American Institute of Physics, New York, 1997), Vol. 406, pp. 294–302.

R. Betti, V. Goncharov, R. L. McCrory, and C. P. Verdon, "Linear Theory of the Ablative Rayleigh–Taylor Instability," in *Advances in Laser Interaction with Matter and Inertial Fusion*, edited by G. Velarde, J. M. Martinez-Val, E. Minguez, and J. M. Perlado (World Scientific, Singapore, 1997), pp. 125–128.

T. R. Boehly, R. L. McCrory, C. P. Verdon, J. M. Soures, A. Babushkin, R. E. Bahr, R. Boni, D. K. Bradley, R. S. Craxton, J. A. Delettrez, W. R. Donaldson, R. Epstein, D. R. Harding, P. A. Jaanimagi, S. D. Jacobs, K. Kearney, R. L. Keck, J. H. Kelly, T. J. Kessler, R. L. Kremens, J. P. Knauer, S. A. Letzring, D. J. Lonobile, S. J. Loucks, L. D. Lund, F. J. Marshall, P. W. McKenty, D. D. Meyerhofer, S. F. B. Morse, A. Okishev, S. Papernov, G. Pien, T. Safford, W. Seka, R. W. Short, M. J. Shoup III, M. D. Skeldon, S. Skupsky, A. W. Schmid, D. J. Smith, S. Swales, M. D. Wittman, and B. Yaakobi, "The First Year of ICF Experiments at the OMEGA Laser Facility," in *Fusion Energy 1996* (IAEA, Vienna, 1997), Vol. 3, pp. 31–42.

T. R. Boehly, V. A. Smalyuk, D. D. Meyerhofer, J. P. Knauer, D. K. Bradley, C. P. Verdon, and D. Kalantar, "The Effect of Increased Irradiation Uniformity on Imprinting by 351-nm Laser Light," in *Laser Interaction and Related Plasma Phenomena*, edited by G. H. Miley, E. M. Campbell, W. J. Hogan, C. Maille-Petersen, H. Coppedge, and E. Montoya (American Institute of Physics, New York, 1997), Vol. 406, pp. 122–129.

B. Buerke, J. P. Knauer, S. J. McNaught, and D. D. Meyerhofer, "Precision Tests of Laser-Tunneling Ionization Models," in *Applications of High Field and Short Wavelength Sources VII*, 1997 OSA Technical Digest Series, Vol. 7 (OSA, Washington, DC, 1997), pp. 75–76.

J. L. Chaloupka, T. J. Kessler, and D. D. Meyerhofer, "A Three-Dimensional Ponderomotive Trap for High-Energy Electrons," in *Applications of High Field and Short Wavelength Sources VII*, 1997 OSA Technical Digest Series, Vol. 7 (OSA, Washington, DC, 1997), p. 109.

S. D. Jacobs, "Deterministic Manufacturing of Precision Glass Optics Using Magnetorheological Finishing (MRF)," in *Advances in Fusion and Processing of Glass II*, edited by A. G. Clare and L. E. Jones (The American Ceramic Society, Westerville, OH, 1998), Vol. 82, pp. 457–468.

R. L. Keck, A. V. Okishev, M. D. Skeldon, A. Babushkin, and W. Seka, "Pulse Shaping on the OMEGA Laser System," in *Laser Interaction and Related Plasma Phenomena*, edited by G. H. Miley, E. M. Campbell, W. J. Hogan, C. Maille-Petersen, H. Coppedge, and E. Montoya (American Institute of Physics, New York, 1997), Vol. 406, pp. 333–340.

T. J. Kessler, Y. Lin, L. S. Iwan, W. P. Castle, C. Kellogg, J. Barone, E. Kowaluk, A. W. Schmid, K. L. Marshall, D. J. Smith, A. L. Rigatti, J. Warner, and A. R. Staley, "Laser Phase Conversion Using Continuous Distributed Phase Plates," in *Solid-State Lasers for Application to Inertial Confinement Fusion*, edited by M. L. André (SPIE, Bellingham, WA, 1997), Vol. 3047, pp. 272–281.

J. P. Knauer, D. D. Meyerhofer, T. R. Boehly, D. Ofer, C. P. Verdon, D. K. Bradley, P. W. McKenty, V. A. Smalyuk, S. G. Glendinning, and R. G. Watt, "Single-Mode Rayleigh–Taylor Growth-Rate Measurements with the OMEGA Laser System," in *Laser Interaction and Related Plasma Phenomena*, edited by G. H. Miley, E. M. Campbell, W. J. Hogan, C. Maille-Petersen, H. Coppedge, and E. Montoya (American Institute of Physics, New York, 1997), Vol. 406, pp. 284–293.

J. C. Lambropoulos, S. D Jacobs, B. Gillman, F. Yang, and J. Ruckman, "Subsurface Damage in Microgrinding Optical Glasses," in *Advances in Fusion and Processing of Glass II*, edited by A. G. Clare and L. E. Jones (The American Ceramic Society, Westerville, OH, 1998), Vol. 82, pp. 469–474.

R. L. McCrory, "The LLE Direct-Drive Target Physics Experimental Program: First Year of Experiments on OMEGA," in *Advances in Laser Interaction with Matter and Inertial Fusion*, edited by G. Velarde, J. M. Martinez-Val, E. Minguez, and J. M. Perlado (World Scientific, Singapore, 1997), pp. 16–19 (invited).

J. J. Ou and S.-H. Chen, "Molecular Dynamics Simulation of Organic Glass-Formers: I. *ortho*-Terphenyl and 1,3,5-Tri-α-Naphthyl Benzene," J. Comput. Chem. **19**, 86 (1998).

S. Papernov, A. W. Schmid, and F. Dahmani, "Laser Damage in Polymer Waveguides Driven Purely by a Nonlinear, Transverse-Scattering Process," Opt. Commun. **147**, 112 (1998).

J. F. Seely, G. E. Holland, T. Boehly, G. Pien, and D. Bradley "Uniformity of the Soft-X-Ray Emissions from Gold Foils Irradiated by OMEGA Laser Beams Determined by a Two-Mirror Normal-Incidence Microscope with Multilayer Coatings," Appl. Opt. **37**, 1140 (1998).

W. Seka, A. Babushkin, T. R. Boehly, D. K. Bradley, M. D. Cable, R. S. Craxton, J. A. Delettrez, W. R. Donaldson, D. R. Harding, P. A. Jaanimagi, R. L. Keck, J. H. Kelly, T. J. Kessler, J. P. Knauer, R. L. Kremens, F. J. Marshall, R. L. McCrory, P. W. McKenty, D. D. Meyerhofer, S. F. B. Morse, A. V. Okishev, G. Pien, M. D. Skeldon, J. M. Soures, C. P. Verdon, B. Yaakobi, and J. D. Zuegel, "OMEGA Experimental Program and Recent Results," in *Laser Interaction and Related Plasma Phenomena*, edited by G. H. Miley, E. M. Campbell, W. J. Hogan, C. Maille-Petersen, H. Coppedge, and E. Montoya (American Institute of Physics, New York, 1997), Vol. 406, pp. 56–66.

H. Shi, B. M. Conger, D. Katsis, and S.-H. Chen, "Circularly Polarized Fluorescence from Chiral Nematic Liquid Crystalline Films: Theory and Experiment," Liq. Cryst. **24**, 163 (1998).

M. D. Skeldon, A. Babushkin, W. Bittle, A. V. Okishev, and W. Seka, "Modeling the Temporal-Pulse-Shape Dynamics of an Actively Stabilized Regenerative Amplifier," IEEE J. Quantum Electron. **34**, 286 (1998).

M. D. Skeldon, A. Babushkin, J. D. Zuegel, R. L. Keck, A. Okishev, and W. Seka, "Modeling of an Actively Stabilized Regenerative Amplifier for OMEGA Pulse-Shaping Applications," in *Solid-State Lasers for Application to Inertial Confinement Fusion*, edited by M. L. André (SPIE, Bellingham, WA, 1997), Vol. 3047, pp. 129–135.

F. Yang, D. Golini, D. H. Raguin, and S. D. Jacobs, "Planarization of Gratings Using Magnetorheological Finishing," in *Science and Technology of Semiconductor Surface Preparation*, edited by G. S. Higashi, M. Hirose, S. Raghavan, and S. Verhaverbeke (Materials Research Society, Pittsburgh, PA, 1997), Vol. 477, pp. 131–136.

M. Yu, C. J. McKinstrie, and G. P. Agrawal, "Temporal Modulational Instabilities of Counterpropagating Light Waves in a Finite Dispersive Kerr Medium, Part I: Theoretical Model and Analysis," J. Opt. Soc. Am. B **15**, 607 (1998).

M. Yu, C. J. McKinstrie, and G. P. Agrawal, "Temporal Modulational Instabilities of Counterpropagating Light Waves in a Finite Dispersive Kerr Medium, Part II: Application to Fabry–Perot Cavities," J. Opt. Soc. Am. B **15**, 617 (1998).

Forthcoming Publications

S. Alexandrou, C.-C. Wang, M. Currie, R. Sobolewski, and T. Y. Hsiang, "Characterization of Coplanar Transmission Lines at Subterahertz Frequencies," to be published in IEEE Transactions on Microwave Theory and Techniques.

E. L. Alfonso, S.-H. Chen, R. Q. Gram, and D. R. Harding, "Fabrication of Polyimide Shells by Vapor Phase Deposition for Use as ICF Targets," to be published in Fusion Technology.

E. L. Alfonso, S.-H. Chen, R. Q. Gram, and D. R. Harding, "Properties of Polyimide Shells Made Using Vapor Phase Deposition," to be published in the Journal of Materials Research.

A. Babushkin, R. S. Craxton, S. Oskoui, M. J. Guardalben, R. L. Keck, and W. Seka, "Demonstration of the Dual-Tripler Scheme for Increased-Bandwidth Third-Harmonic Generation," to be published in Optics Letters.

A. Babushkin, W. Seka, S. A. Letzring, W. Bittle, M. Labuzeta, M. Miller, and R. G. Roides, "Multicolor Fiducial Laser for Streak Cameras and Optical Diagnostics for the OMEGA Laser System," to be published in the Proceedings of the 22nd International Congress on High-Speed Photography and Photonics, Santa Fe, NM, 27 October–1 November 1996.

R. Betti, "Beta Limits for the N = 1 Mode in Rotating-Toroidal-Resistive Plasmas Surrounded by a Resistive Wall," to be published in Physics of Plasmas.

R. Betti, V. N. Goncharov, and R. L. McCrory, "Hydrodynamic Stability Theory of Unsteady Ablation Fronts," to be published in Laser and Particle Beams.

R. Betti, V. N. Goncharov, R. L. McCrory, and C. P. Verdon, "Growth Rates of the Ablative Rayleigh–Taylor Instability in Inertial Confinement Fusion," to be published in Physics of Plasmas.

T. R. Boehly, R. L. McCrory, C. P. Verdon, W. Seka, S. J. Loucks, A. Babushkin, R. E. Bahr, R. Boni, D. K. Bradley, R. S. Craxton, J. A. Delettrez, W. R. Donaldson, R. Epstein, D. Harding, P. A. Jaanimagi, S. D. Jacobs, K. Kearney, R. L. Keck, J. H. Kelly, T. J. Kessler, R. L. Kremens, J. P. Knauer, D. J. Lonobile, L. D. Lund, F. J. Marshall, P. W. McKenty, D. D. Meyerhofer, S. F. B. Morse, A. Okishev, S. Papernov, G. Pien, T. Safford, J. D. Schnittman, R. Short, M. J. Shoup III, M. Skeldon, S. Skupsky, A. W. Schmid, V. A. Smalyuk, D. J. Smith, J. M. Soures, M. Wittman, and B. Yaakobi, "Inertial Confinement Fusion Experiments with OMEGA—a 30-kJ, 60-Beam UV Laser," to be published in the Proceedings of the 1997 IAEA Conference, Osaka, Japan, 10–14 March 1997.

T. R. Boehly, D. D. Meyerhofer, J. P. Knauer, D. K. Bradley, T. Collins, J. A. Delettrez, V. N. Goncharov, R. L. Keck, S. Regan, V. A. Smalyuk, W. Seka, and R. P. J. Town, "Laser-Uniformity and Hydrodynamic-Stability Experiments at the OMEGA Laser Facility," to be published in Laser and Particle Beams.

D. K. Bradley, J. A. Delettrez, R. Epstein, F. J. Marshall, S. Regan, R. P. J. Town, B. Yaakobi, D. A. Haynes, Jr., C. F. Hooper, Jr., and C. P. Verdon, "Spherical Rayleigh–Taylor Experiments on the 60-Beam OMEGA Laser System," to be published in Laser and Particle Beams.

S.-H. Chen, J. C. Mastrangelo, B. M. Conger, and D. Katsis, "Design, Synthesis, and Potential Application of Glass-Forming Functional Organic Materials," to be published in Makromolekular Chemie, Macromolecular Symposium (invited).

S.-H. Chen, J. C. Mastrangelo, B. M. Conger, A. S. Kende, and K. L. Marshall, "Synthesis and Characterization of Thermotropic Chiral-Nematic Polythiophenes," to be published in Macromolecules.

A. Chirokikh, W. Seka, A. Simon, R. S. Craxton, and V. T. Tikhonchuk, "Stimulated Brillouin Scattering in Long-Scale-Length Laser Plasmas," to be published in Physics of Plasmas.

T. J. B. Collins, H. L. Helfer, and H. M. VanHorn, "A Model for QPOs in CVs Based on Boundary-Layer Oscillations," to be published in Astrophysical Journal, Letters.

T. J. B. Collins, H. L. Helfer, and H. M. Van Horn, "Accretion Disk and Boundary Layer Models Incorporating OPAL Opacities," to be published in Astrophysical Journal.

R. S. Craxton, S. Skupsky, A. Babushkin, J. H. Kelly, T. J. Kessler, J. M. Soures, and J. D. Zuegel, "Beam Smoothing on the OMEGA Laser System," to be published in Laser and Particle Beams.

S. Cremer, C. P. Verdon, and R. D. Petrasso, "Tertiary Proton Diagnostics in Future ICF Experiments," to be published in Physics of Plasmas.

M. Currie, C.-C. Wang, R. Sobolewski, and T. Y. Hsiang, "Picosecond Nodal Testing of Centimeter-Size Superconducting Microstrip Interconnects," to be published in Applied Superconductivity.

F. Dahmani, J. C. Lambropoulos, A. W. Schmid, S. Papernov, and S. J. Burns, "Fracture of Fused Silica with 351-nm-Laser-Generated Surface Cracks," to be published in the Journal of Applied Physics.

F. Dahmani, A. W. Schmid, J. C. Lambropoulos, and S. J. Burns, "Laser-Fluence and Laser-Pulse Number Dependence of Birefringence and Residual Stress near Laser-Induced Cracks in Fused Silica," to be published in the Journal of Applied Optics.

B. DeMarco, C. W. Barnes, K. Kearney, and R. L. Kremens, "Neutron Yield Measurement on the OMEGA Laser System," to be published in the Review of Scientific Instruments.

P. M. Fauchet, "Porous Silicon: Photoluminescence and Electroluminescent Devices," to be published in the Light Emission in Silicon, Semiconductors, and Semimetals Series.

D. Fried, R. E. Glena, J. D. B. Featherstone, and W. Seka, "Permanent and Transient Changes in the Reflectance of CO_2 Laser-Irradiated Dental Hard Tissues at $\lambda = 9.3, 9.6, 10.3,$ and 10.6 μm and at Fluences between 1–20 J/cm^2," to be published in Lasers in Surgery and Medicine.

R. E. Giacone, C. J. McKinstrie, and R. Betti, "Response to 'Comment on "Angular Dependence of Stimulated Brillouin Scattering in Homogeneous Plasma" [Phys. Plasmas **2**, 4596 (1995],' " to be published in Physics of Plasmas.

B. E. Gillman and S. D. Jacobs, "Bound Abrasive Polishers for Optical Glass," to be published in the Journal of Applied Optics.

W. Göb, W. Lang, and R. Sobolewski, "Magnetoresistance of a $YBa_2Cu_3O_7$ Corbino Disk: Probing Geometrical Contributions to the Unconventional Normal-State Magnetoresistance of High-Temperature Superconductors," to be published in Physical Review B: Rapid Communications.

K. Green, M. Lindgren, C.-C. Wang, L. Fuller, T. Y. Hsiang, W. Seka, and R. Sobolewski, "Picosecond Photoresponse in Polycrystalline Silicon," to be published in the Proceedings of Ultrafast Electronics and Optoelectronics, Incline Village, NV, 17–21 March 1997.

M. J. Guardalben, "Conoscopic Alignment Methods for Birefringent Optical Elements in Fusion Lasers," to be published in Optics & Photonics News.

O. E. Hanuch, V. B. Agrawal, S. Papernov, M. delCerro, and J. V. Aquavella, "Posterior Capsular Polishing with the Nd:YLF Picosecond Laser: Model Eye Study," to be published in Investigative Ophthalmology.

D. R. Harding, "Using Ion Beam Techniques to Determine the Elemental Composition of ICF Targets," to be published in Fusion Technology.

S. D. Jacobs, W. I. Kordonski, and H. M. Pollicove, "Precision Control of Aqueous Magnetorheological Fluids for Finishing of Optics," to be published in the Proceedings of ERMR 1997, 6th International Conference on Electrorheological Fluids, Magnetorheological Suspensions, and Their Applications, Yonezawa, Japan, 22–25 July 1997.

S. D. Jacobs, H. M. Pollicove, W. I. Kordonski, and D. Golini, "Magnetorheological Finishing (MRF) in Deterministic Optics Manufacturing," to be published in the Proceedings of the International Conference on Precision Engineering '97, Taipei, Taiwan, 20–22 November 1997.

D. Jacobs-Perkins, M. Currie, K. T. Tang, C.-C. Wang, C. Williams, W. R. Donaldson, R. Sobolewski, and T. Y. Hsiang, "Subpicosecond Electro-Optic Imaging Using Interferometric and Polarization-Based Apparatus," to be published in the Proceedings of Ultrafast Electronics and Optoelectronics, Incline Village, NV, 17–21 March 1997.

J. P. Knauer, C. P. Verdon, R. Betti, D. D. Meyerhofer, T. R. Boehly, D. K. Bradley, V. A. Smalyuk, P. W. McKenty, S. G. Glendinning, D. H. Kalantar, R. G. Watt, P. L. Gobby, O. Willi, and R. J. Taylor, "Single-Mode Rayleigh–Taylor Growth-Rate Measurements with the OMEGA Laser System," to be published in Physical Review E.

J. P. Knauer, C. P. Verdon, T. J. B. Collins, V. N. Goncharov, R. Betti, T. R. Boehly, D. D. Meyerhofer, and V. A. Smalyuk, "Interpretation of X-Ray Radiographic Images of Rayleigh–Taylor Unstable Interfaces," to be published in Laser and Particle Beams.

E. M. Korenic, S. D. Jacobs, S. M. Faris, and L. Li, "Cholesteric Liquid Crystal Flakes–A New Form of Domain," to be published in Molecular Crystals and Liquid Crystals.

E. M. Korenic, S. D. Jacobs, S. M. Faris, and L. Li, "Cholesteric Liquid Crystal Transmission Profile Asymmetry," to be published in Molecular Crystals and Liquid Crystals.

E. M. Korenic, S. D. Jacobs, S. M. Faris, and L. Li, "Color Gamut of Cholesteric Liquid Crystal Films and Flakes by Standard Colorimetry," to be published in COLOR Research and Application.

K. S. Lebedev, E. A. Magulariya, S. G. Lukishova, S. V. Belyaev, N. V. Malimonenko, and A. W. Schmid, "Reflective Nonlinearities of Nonabsorbing Chiral Liquid Crystals: Frustration of Selective Reflection by Powerful Laser Radiation," to be published in the Bulletin of the American Physical Society.

M. Lindgren, M. Currie, C. Williams, T. Y. Hsiang, P. M. Fauchet, S. H. Moffat, R. A. Hughes, J. S. Preston, and F. A. Hegmann, "Ultrafast Photoresponse and Pulse Propagation in High-T_c Superconducting Y-Ba-Cu-O Thin Film Devices," to be published in the IEEE Journal on Selected Topics in Quantum Electronics.

M. Lindgren, M. Currie, C. Williams, T. Y. Hsiang, P. M. Fauchet, R. Sobolewski, S. H. Moffat, R. A. Hughes, J. S. Preston, and F. A. Hegmann, "Intrinsic Photoresponse of a Y-Ba-Cu-O Superconductor," to be published in Physical Review B.

M. Lindgren, W.-S. Zeng, M. Currie, R. Sobolewski, S. Cherednichenko, B. Voronov, and G. N. Gol'tsman, "Picosecond Response of a Superconducting Hot-Electron NbN Photodetector," to be published in Applied Superconductivity.

M. Lindgren, W.-S. Zeng, M. Currie, C. Williams, T. Y. Hsiang, P. M. Fauchet, R. Sobolewski, S. H. Moffat, R. A. Hughes, J. S. Preston, and F. A. Hegmann, "An Ultrafast High-T_c Superconducting Y-Ba-Cu-O Photodetector," to be published in the Proceedings of Ultrafast Electronics and Optoelectronics, Incline Village, NV, 17–21 March 1997.

S. G. Lukishova, S. V. Belyaev, K. S. Lebedev, E. A. Magulariya, A. W. Schmid, and N. V. Malimonenko, "cw and High-Repetition-Rate Lasing in Nd:YAG Resonators with Chiral-Nematic Liquid-Crystal Mirrors: A Study of Nonlinear Responses," to be published in Quantum Electronics.

S. G. Lukishova, S. V. Belyaev, K. S. Lebedev, E. A. Magulariya, A. W. Schmid, and N. V. Malimonenko, "Nonlinear Bleaching in the Selective Reflection of Nonabsorbing Chiral-Nematic Liquid-Crystal Thin Films," to be published in JETP Letters and in Molecular Crystals and Liquid Crystals.

F. J. Marshall, M. M. Allen, J. P. Knauer, J. A. Oertel, and T. Archuleta, "A High-Resolution X-Ray Microscope for Laser-Driven Planar-Foil Experiments," to be published in Physics of Plasmas.

K. L. Marshall, J. Haddock, N. Bickel, D. Singel, and S. D. Jacobs, "Angular-Scattering Characteristics of Ferroelectric Liquid Crystal Electro-Optical Devices Operating in the TSM and ESM Modes," to be published in the Journal of Applied Optics.

S. M. McCormack, D. Fried, J. D. B. Featherstone, R. E. Glena, and W. Seka, "Scanning Electron Microscope Observations of CO_2 Laser Effects on Dental Enamel," to be published in the Journal of Dental Research.

C. J. McKinstrie, A. V. Kanaev, V. T. Tikhonchuk, R. E. Giacone, and H. X Vu, "Three-Dimensional Analysis of the Power Transfer Between Crossed Laser Beams," to be published in Physics of Plasmas.

C. J. McKinstrie and E. J. Turano, "Non-relativistic Motion of a Charged Particle in an Electromagnetic Field," to be published in the Journal of Plasma Physics.

D. D. Meyerhofer, D. K. Bradley, A. V. Chirokikh, R. S. Craxton, S. Regan, W. Seka, R. W. Short, A. Simon, B. Yaakobi, J. Carroll, and R. P. Drake, "Laser–Plasma Interaction Experiments in NIF Direct-Drive Scale Plasmas," to be published in Laser and Particle Beams.

S. Papernov, A. W. Schmid, J. F. Anzellotti, D. J. Smith, D. R. Collier, and F. A. Carbone, "One Step Closer to the Intrinsic Laser Damage Threshold of HfO_2 and SiO_2 Monolayer Thin Films," to be published in the Proceedings of the 30th Annual Symposium on Optical Materials for High Power Lasers, Boulder, CO, 6–8 October 1997.

S. Papernov, A. W. Schmid, and D. Zaksas, "Characterization of Freestanding Polymer Films for Application in 351-nm, High-Peak-Power Laser Systems," to be published in Optical Engineering.

S. Papernov, D. Zaksas, and A. W. Schmid, "A Nonlinear UV-Damage Mechanism in Polymer Thin Films Observed from Below to Above Damage Threshold," to be published in the Proceedings of the 30th Annual Symposium on Optical Materials for High Power Lasers, Boulder, CO, 6–8 October 1997.

S. Papernov, D. Zaksas, and A. W. Schmid, "Perfluorinated Polymer Films with Extraordinary UV-Laser-Damage Resistance," to be published in the Proceedings of the 30th Annual Symposium on Optical Materials for High Power Lasers, Boulder, CO, 6–8 October 1997.

R. D. Petrasso, C. K. Li, M. D. Cable, S. M. Pollaine, S. W. Haan, T. P. Bernat J. D. Kilkenny, S. Cremer, J. P. Knauer, C. P. Verdon, and R. L. Kremens, "Implosion Symmetry and ρR Measurements of the National Ignition Facility from Nascent 31-MeV Tertiary Protons," to be published in Physical Review Letters.

A. L. Rigatti and D. J. Smith, "Status of Optics on the OMEGA Laser System after 18 Months of Operation," to be published in the Proceedings of the XXVIII Annual Symposium on Optical Materials for High Power Lasers, Boulder, CO, 7–9 October 1996.

J. Z. Roach, A. Ninkov, S. W. Swales, and T. Morris, "Design and Evaluation of a Screen CCD Imaging System," to be published in Optical Engineering.

W. Seka, T. R. Boehly, D. K. Bradley, V. Glebov, P. A. Jaanimagi, J. P. Knauer, F. J. Marshall, D. D. Meyerhofer, R. Petrasso, S. Regan, J. M. Soures, B. Yaakobi, J. D. Zuegel, R. Bakukutumbi, T. J. B. Collins, R. S. Craxton, J. A. Delettrez, R. L. McCrory, P. W. McKenty, R. W. Short, A. Simon, S. Skupsky, and R. P. J. Town, "Experimental Program at LLE in Support of the Direct-Drive Approach to Ignition for the NIF," to be published in Laser and Particle Beams.

A. Simon, "Comparison Between SBS Theories and Experiment," to be published in the Proceedings of the LaJolla Summer School '95, Plasma Physics and Technology (AIP).

M. D. Skeldon, R. Saager, and W. Seka, "Quantitative Pump-Induced Wavefront Distortions in Laser-Diode- and Flash-Lamp-Pumped Nd:YLF Laser Rods," to be published in IEEE Journal of Quantum Electronics.

V. A. Smalyuk, D. D. Meyerhofer, T. R. Boehly, J. P. Knauer, and D. K. Bradley, "Characterization of an X-Ray Radiographic System Used to Measure the Evolution of Broadband Imprint in Laser-Driven Planar Targets," to be published in Review of Scientific Instruments.

D. J. Smith, J. F. Anzellotti, S. Papernov, and Z. R. Chrzan, "High Laser-Induced-Damage Threshold Polarizer Coatings for 1054 nm," to be published in the Proceedings of the XXVIII Annual Symposium on Optical Materials for High Power Lasers, Boulder, CO, 7–9 October 1996.

C. Stockinger, W. Markowitsch, W. Lang, W. Kula, and R. Sobolewski, "Mechanisms of Photodoping in Oxygen-Deficient $YBa_2Cu_3O_x$ Films Studied by *In-Situ* Transport," to be published in Physical Review B.

B. Yaakobi and F. J. Marshall, "Imaging the Cold, Compressed Shell in Laser Implosions Using the Kα Fluorescence of a Titanium Dopant," to be published in Physical Review E.

B. Yaakobi, F. J. Marshall, and D. K. Bradley, "Pinhole-Array X-Ray Spectrometer for Laser-Fusion Experiments," to be published in Applied Optics.

J. D. Zuegel and W. Seka, "Upconversion and Reduced $^4F_{3/2}$ Upper-State Lifetime in Intensely Pumped Nd:YLF," to be published in Optics Letters.

Conference Presentations

A. Babushkin and W. Seka, "Efficient End-Pumped 1053-nm YLF:Nd Laser," Advanced Solid-State Lasers—Thirteenth Topical Meeting, Coeur D'Alene, Idaho, 2–4 February 1998.

S. J. Loucks, R. L. McCrory, S. F. B. Morse, W. Seka, T. R. Boehly, R. Boni, T. H. Hinterman, R. L. Keck, J. H. Kelly, T. J. Kessler, L. D. Lund, D. D. Meyerhofer, A. V. Okishev, G. Pien, M. J. Shoup III, D. J. Smith, and K. A. Thorp, "OMEGA Architecture, Capabilities, and Operations," JOWOG 37, Los Alamos, NM, 2–5 February 1998.

W. Kordonski, D. Golini, P. Dumas, S. Hogan, and S. Jacobs, "Magnetorheological Suspension-Based Finishing Technology (MRF)," SPIE's 5th Annual International Symposium on Smart Structures and Materials, San Diego, CA, 1–5 March 1998.

A. Chirokikh, D. D. Meyerhofer, W. Seka, R. S. Craxton, and A. Simon, "Stimulated Brillouin Scattering in Long-Scale-Length Plasmas on the OMEGA Laser System," XXV Zvenigorod Conference on Plasma Physics and Fusion, Zvenigorod, Russia, 2–6 March 1998.

A. Simon, "Transit-Time Damping and a New Physical Picture for Landau Damping," Physics Department of the National Cheng Kung University, Taiwan, China, 9 March 1998.

The following presentations were made at the Second International Workshop on Laboratory Astrophysics with Intense Lasers, Tucson, AZ, 19–21 March 1998:

T. R. Boehly, D. D. Meyerhofer, J. P. Knauer, D. K. Bradley, T. Collins, J. A. Delettrez, R. L. Keck, S. Regan, V. A. Smalyuk, W. Seka, and R. P. J. Town, "Laser-Driven Hydrodynamic Instability Experiments of Interest to Inertial Confinement Fusion."

D. D. Meyerhofer, "Observation of Positron Production by Multiphoton Light by Light Scattering."